Discrete Element Methods for the Thermo-Mechanics of Ceramic Breeder Pebble Beds

Zur Erlangung des akademischen Grades

Doktor der Ingenieurwissenschaften

der KIT-Fakultät für Maschinenbau

Karlsruher Institut für Technologie (KIT)

genehmigte

Dissertation

von

Marigrazia Moscardini

Tag der mündlichen Prüfung: 22 Oktober 2018

Hauptreferent:	Prof. Dr.-Ing. Marc Kamlah
	Karlsruher Institut für Technologie (KIT)
Korreferent:	Prof. Dr.-Ing. Thomas Schulenberg
	Karlsruher Institut für Technologie (KIT)

Abstract

Tritium breeder and neutron multiplier materials are required to guarantee the self-sustainment of the tritium fuel in a fusion reactor. Both materials are located in the breeder blanket, a compulsory component for the future DEMOnstration power reactor. Different breeder blanket concepts will be tested in ITER (International Thermonuclear Experimental Reactor) preceding DEMO to demonstrate the achievement of the operating targets and the fulfillment of allowable limits. In the solid breeder blanket concept both the breeder and neutron multiplier materials are in the form of packed pebble beds. Pebble beds are assemblies of pebbles highly packed into a stiff metallic structure with helium used as tritium purge gas flowing through the voids among particles. Due to the discrete nature of these materials, the macroscopic behavior of the whole bed is the result of the particle-particle, particle-wall and particle-gas interactions. This originates a complex fully coupled thermo-mechanical behavior in which several parameters such as packing factor, particle size, gas pressure and temperature play a major role. In this frame, the Discrete Element Method (DEM) is an appropriate tool able to characterize the thermo-mechanical behavior of fusion pebble beds as result of the particle interactions by modelling pebbles individually. Furthermore, allowing investigating pebble beds at the microscale level, DEM is a suitable approach to study phenomena and evaluate parameters otherwise inaccessible to experiments or other tools, representing a strong support for the design of the breeder blanket.

In Europe, an advanced DEM code is under development for a long time at the Karlsruhe Institute of Technology (KIT) to investigate the behavior of ceramic breeder pebble beds. In the first part of this thesis, the existing in-house mechanical DEM code, developed to study the mechanical behavior of perfect spherical packed particles, was further extended to investigate the influence of the sphericity of the currently produced pebbles on the mechanical behavior of the bed. In the second part of the work, an innovative in-house thermal DEM code was developed to simulate the heat transfer in the breeder pebble beds. As innovative step, the Smoluchowski effect was implemented for the first time into a DEM code allowing simulating the influence of the gas pressure on the effective thermal conductivity. The code was first validated and then used to evaluate the effective thermal conductivity of the breeder bed demonstrating a strong predictability under several different conditions. Afterwards, the code was applied to estimate the temperature field generated inside the thickness of the breeder bed under fusion relevant conditions.

Kurzfassung

Zur Produktion des Tritium-Brennstoffs werden Tritium-Brutmaterialen und Neutronenmultiplikatoren in Fusionsreaktoren benötigt. Beide Materilien befinden sich im Brutblanket, einer unverzichtbaren Komponente des zukünftigen DEMO (DEMonstration Power Plant) Fusionsdemonstrationsreaktor. Im Versuchsreaktor ITER (International Thermonuclear Experimental Reactor) werden im Vorfeld des DEMO-Reaktorprojekts, zum Nachweise der Erreichbarkeit bestimmter Ziele sowie der Einhaltung zulässiger Grenzwerte während des Betriebs, verschiedene Brutblanketkonzepte getestet. Dem Feststoff-Brutblanketkonzept liegen sowohl ein Neutronenmultiplikator als auch ein Brutmaterial in Form eines Schüttbetts zu Grunde. Letztere bestehen aus in eine steife Metallstruktur gepackten, dichten Kugelschüttungen, in deren Hohlräume Helium als Tritiumspülgas strömt. Aufgrund der granularen Beschaffenheit solcher Materialien ist das makroskopische Verhalten der gesamten Schüttung das Ergbnis der Teilchen-Teilchen-, Teilchen-Wand- und Teilchen-Gas-Wechselwirkungen. Es entsteht ein komplexes, vollständig gekoppeltes thermomechanisches Verhalten, bei dem verschiedene Parameter wie beispielsweise die Packungsdichte, die Partikelgröße, der Gasdruck und die Temperatur einen entscheidenden Einfluss auf das Verhalten des Blankets haben. Die Diskrete-Elemente-Methode (DEM) ist ein angemessenes Werkzeug, das durch Modellierung einzelner Partikel die Charakterisierung des thermomechanischen Verhaltens von Fusionsschüttbetten als Ergbnis von Teilchenwechselwirkungen erlaubt. Darüber hinaus ist die DEM ein geeignetes Instrument Schüttungen auf mikrostruktureller Ebene zu erforschen und entscheidende, die Eigenschaften und das Verhalten beeinflussende Parameter zu identifizieren, die mit Experimenten oder anderen Methoden nicht untersucht und bewertet werden können. Dadurch stellt die DEM eine wesentliche Unterstützung für das Design eines Brutblanket dar.

In Europa wird am Karlsruher Institut für Technologie (KIT) seit einiger Zeit an der Entwicklung eines geeigneten, eigenen DEM-Codes gearbeitet, der zur Untersuchung des Verhaltens keramischer Schüttbetten für die Tritiumerzeugung dient. Im ersten Teil der vorliegenden Dissertation wird der mechanische DEM-Code, der zur Analyse des mechanischen Verhaltens perfekt sphärischer Partikelschüttungen entwickelt wurde erweitert, sodass der Einfluss der Sphärizität der gegenwärtig hergestellten Kugeln auf das mechanische Verhalten des Schüttbetts untersucht werden kann. Der zweite Teil der Arbeit behandelt die Entwicklung eines innovativen thermischen DEM-Codes zur Simulation des Wärmeaustauschs im Schüttbett. Der erstmals in einen DEM-Code implementierte

Smoluchowski-Effekt erlaubt es, den Einfluss des Gasdrucks auf die effektive Wärmeleitfähigkeit zu simulieren. Nach erfolgreicher Validierung des erweiterten Codes konnte dieser zur Bewertung der effektiven Wärmeleitfähigkeit des Schüttbetts verwendet werden. Er ermöglicht somit gute Vorhersagen unter verschiedenen Bedingungen. Des Weiteren findet der Code Anwendung zur Berechnung des innerhalb des Schüttbetts in Dickenrichtung erzeugten Temperaturfelds unter Fusionsbedingungen.

Contents

Abbreviations

BU	*Breeder Unit*
CEA	*Commissariat à l'énergie atomique et aux énergies alternatives*
CN	*Coordination Number*
CPs	*Cooling Plates*
DEM	*Discrete Element Method*
DEMO	*Demonstration Power Reactor*
D-T	*Deuterium-Tritium*
EU Ref.	*EU Reference*
FEA	*Finite Element Analysis*
FEM	*Finite Element Method*
HCPB	*Helium Cooled Pebble Bed*
HM	*Hall and Martin correlation*
ITER	*International Thermonuclear Experimental Reactor*
JAERI	*Japan Atomic Energy Research Institute*
KIT	*Karlsruhe Institute of Technology*
LMT	*Li_2TiO_3 (lithium metatitanate)*
LOCA	*Loss of Cooling Accident*
MCs	*Multi Contacts*
MS	*Multi-Sphere*
OB	*Outboard*
PF	*Packing Factor*
RCP	*Random Close Packing*
R&D	*Research and Development*
RI	*Inner Radius*
RO	*Outer Radius*
RT	*Room Temperature*
SBZ	*Schunder, Bauer, Zehner correlation*
TBM	*Test Blanket Modules*
TD	*Theoretical Density*
TRT	*Tritium Residence Time*
UCLA	*University of California Los Angeles*
UCT	*Uniaxial Compression Test*

x

Symbols

Roman letters

A	[m^2]	*Cross sectional area of non-cubic box*
a, b and c	[m]	*Half-lengths of the ellipsoid principal axes*
a_r	[/]	*Aspect ratio of the ellipsoidal particle*
C	[/]	*Goodman's constant*
C_{ij}^{eff}	[W/K]	*Effective conductance of the thermal contact between particle i and j*
C_i^s	[W/K]	*Thermal conductance of the particle i*
C_{ij}^{ct}	[W/K]	*Thermal conductance of the contact*
C_r	[/]	*Contraction rate*
CN	[/]	*Coordination number*
c_p	[J/kg K]	*Specific heat at constant pressure*
D_{ij}	[m]	*Distance between centers of particle i and j*
d	[m]	*Distance between the centers of the two external primary spheres*
d_{ave}	[m]	*Mean gap size (average value over the curvature of the spheres in thermal contact)*
d_m	[m]	*Kinetic molecule diameter*
$\overline{d}_\gamma$	[m]	*Mean value of the gap size (average value over the curvature of the smaller sphere in thermal contact)*
$\overline{d}_\theta$	[m]	*Mean value of the gap size (average value over the curvature of the bigger sphere in thermal contact)*
E	[Pa]	*Young's modulus*
f	[/]	*Super-quadratic equation*
f_{ave}	[N]	*Average normal force*
f_{max}	[N]	*Maximum normal force*
f_N	[N]	*Normal force*
f_T	[N]	*Tangential force*
G_{eff}	[Pa]	*Shear modulus*
H	[m]	*Bed height*
h_i	[m]	*Height of the i-th spherical cap*
h_{ij}	[m]	*Minimum gap between particle i and j*
I	[kg m^2]	*Moment of Inertia*

K_n	[/]	Knudsen number
K_s	[Pa]	Shear stiffness
$\mathcal{K}$	[J/K]	Boltzmann constant
k_{eff}	[W/m K]	Effective thermal conductivity
k_g	[W/m K]	Thermal conductivity of unconfined gas
k_g^c	[W/m K]	Thermal conductivity of confined gas
$k_{g,ij}$	[W/m K]	Thermal conductivity of unconfined gas at the average temperature of the two particle in contact
$k_{g,ij}^c$	[W/m K]	Thermal conductivity of confined gas at the average temperature of the two particle in contact
k_s	[W/m K]	Solid thermal conductivity
$k_{s,ij}$	[W/m K]	Thermal conductivity for the contact zone at the average temperature of the two particle in contact
k_{eff_0}	[W/m K]	Thermal conductivity of the bed when gas is considered unconfined
L	[m]	Length of the gas confining space
L_b	[m]	Length of virtual box
l	[m]	Length of the square section of the assembly
$\boldsymbol{M}$	[Nm]	Torque
m	[kg]	Mass of the particle
m_g	[gr/mol]	Atomic mass of the gas
m_r	[/]	Ratio of the gas (m_g) to solid (m_s) atomic masses
m_s	[gr/mol]	Atomic mass of the solid material
N_s	[/]	Number of primary spheres composing the individual ellipsoidal particle
N_p	[/]	Number of particles in the assembly
N^{MC}	[/]	Number of multi-contacts
$\boldsymbol{n}$	[/]	Normal unit vector
p	[Pa]	Gas pressure
p_h	[Pa]	Hydrostatic pressure
p_r	[%]	Porosity of the solid material
$\dot{q}_v$	[W/ m^3]	Volumetric heat source
q	[/]	Quaternion
$q_{i,bw}$	[W/m^2]	Heat flux between particle i and bottom wall
q_{ij}	[W/m^2]	Heat flux between particle i and j

R	[m]	Radius of primary sphere in monosized bed
R_i	[m]	Radius of the i-th primary sphere
R_{ij}	[m]	Equivalent radius
R_{ij}^e	[m]	Effective radius
R_{in}	[m]	Radius equal for all primary spheres for which no overlaps occur in the assembly
R_{max}	[m]	Radius of the biggest primary sphere
R_{min}	[m]	Radius of the smallest primary sphere
R_{out}	[m]	Radius equal for all primary spheres to get a PF=1
R_{sm}	[m]	Smaller radius of any two consecutive primary spheres in an ellipsoidal particle
R^{rd}	[m]	Reduced radius
$\underline{\underline{R}}$	[/]	Rotation matrix
$\underline{\underline{R}}^T$	[/]	Transposed rotation matrix
r_c	[m]	Contact radius
r_i	[/]	R_i/R_{max}
T	[K] or [°C]	Temperature
T_{ave}	[K] or [°C]	Average temperature of the thermal contact
t_f	[/]	Slope of the line for the alignment of the primary spheres
X	[/]	Fraction of the distance in overlap defining the height of the spherical cap of the smallest primary sphere
x,y and z	[m]	Position in Cartesian coordinates
$\ddot{x}$	[m/s^2]	Acceleration of the particle
V	[m^3]	Volume of the virtual box
$V_{tot,s}$	[m^3]	Total volume of the spheres
V_p	[m^3]	Volume of the individual ellipsoidal particle
$V_{s,i}$	[m^3]	Volume of the i-th primary sphere
$(V_{sc,i} + V_{sc,i+1})$	[m^3]	Total volume of the i-th spherical cap

Greek letters

α	[/]	Ratio between solid and gas thermal contact
α_d	[m^2/s]	Thermal diffusivity
α_c	[/]	Thermal accommodation coefficient
α_r	[rad]	Angle of rotation

xiii

β	[/]	*Gas constant in Kaganer's model*
γ	[rad]	*Integration angle for the mean value of the gap size $\overline{d}_\gamma$ of the smaller particle in contact*
$\Delta\varepsilon$	[%]	*Variation of the residual strain*
$\Delta\eta$	[/]	*Difference between the packing factors calculated by the scaling radius R_{out} and R_{in}*
$\Delta\dot{\boldsymbol{x}}_T$	[m/s]	*Sliding velocity*
Δt	[s]	*Simulation time step*
δ	[/]	*Fraction of R_{min} in overlap*
δ_s	[m]	*Overlap between two consecutive primary spheres*
δ_p	[m]	*Overlap between two primary spheres of two different ellipsoidal particles in contact*
δ^*	[m]	*Weighted distance among contacting particles on the average normal force*
$\delta_d^{(I,J)}$	[m]	*Distance between the contacting particles I and J*
ε_1 and ε_2	[/]	*Blockiness controllers in the Super-quadratic function*
ε_{33}	[%]	*Strain in the axial direction*
η_{ij}	[/]	*Cut-off parameter in contacting particles*
θ	[rad]	*Integration angle for the mean value of the gap size $\overline{d}_\theta$ of the bigger particle in contact*
Λ	[m]	*Mean free path*
ξ_{ij}	[/]	*Cut-off parameter in particles with separation gap*
μ_f	[/]	*Friction coefficient*
ν	[/]	*Poisson's ratio*
ρ	[kg/m^3]	*Density of the particle*
τ	[/]	*Parameter for the stability of the calculation*
σ_{33}	[MPa]	*Stress in the axial direction*
Σ	[N/mm^3]	*Parameter to correlate CN to p_h*
$\mathcal{X}$	[/]	*Fraction of the sphere curvature involved in the heat transfer*
$\mathcal{X}_c$	[/]	*Ratio between R_{out} at the current time step over R_{out} at the previous time step*
Ψ	[W/m^3]	*Neutronic power density*
ω	[1/s^2]	*Angular velocity*

Chapter 1

Introduction

Tritium breeding and neutron multiplier materials are both needed for the self-sustainment of the tritium fuel in a fusion reactor. According to the solid breeder blanket concept both these materials are used in the form of pebble beds in the breeder blanket component. Due to their discrete nature, pebble beds show a complex fully coupled thermo-mechanical behavior. Simulations carried out with a Discrete Numerical Method (DEM) allow evaluating the thermo-mechanical behavior of pebble beds as a result of the interactions among particles supporting the design of the breeder blanket. In this chapter, a general overview about fusion technology, breeding blanket concept and pebble beds is given first. Thereafter, the motivation of this work is introduced. Finally, a brief description of the chapters is included.

1.1 Nuclear Fusion Background

The nuclear fusion reaction occurs when two or more atomic nuclei fuse together to form a heavier nucleus. The difference in mass between products and reactants is equivalent to the energy release. In order to overcome the Coulomb barrier due to the electrostatic repulsion, the nuclear short-range forces have to be activated bringing the two nuclei close to each other. To this end, a high amount of kinetic energy has to be provided to the two nuclei [1] (Azteni and Meyer-ter-Vehn,2017).

In thermo nuclear fusion applications, the needed amount of kinetic energy is provided heating the two nuclei up to the corresponding ignition temperature[1]. The probability for the reaction to occur between the two nuclei, which is given by the microscopic cross section of the related fusion reaction, changes with the temperature. Figure 1−1 shows the microscopic cross sections as a function of the kinetic temperature [1] (Azteni and Meyer-ter-Vehn,2017).

Among the fusion reactions, the deuterium tritium reaction (D-T) shows the highest microscopic cross section at the lowest ignition temperature. For this reason, it is considered as a promising candidate for a fusion reactor.

The D-T reaction reads as

$$^{2}_{1}D + ^{3}_{1}T \rightarrow ^{4}_{2}He + ^{1}_{0}n + 17.6\ MeV \qquad\qquad 1.1$$

---
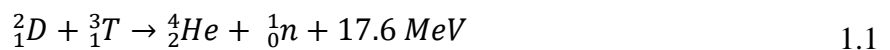
[1] The ignition temperature is reached when a nuclear fusion reaction becomes self-sustained, thus the external energy to heat the fuel is no longer needed.

in which the 80% of the out coming energy is carried by the neutron (14 MeV), while the remaining 20% (3.5MeV) by ^{4}He.
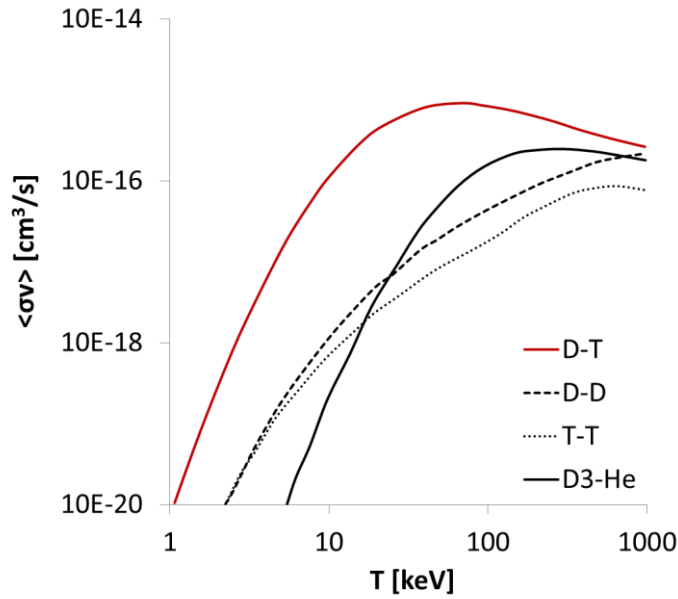

Figure 1–1: Microscopic cross sections of fusion reactions vs. kinetic temperature. Reproduced according to [1] (Azteni and Meyer-ter-Vehn, 2017).

Due to the high temperatures needed to realize the fusion, the fuel D-T is in the state of plasma that is an electrically neutral hot ionized gas where the electrons are separated from the positive nuclei. To sustain the reaction, deuterium and tritium have to be constantly supplied to the plasma. While deuterium is available in nature, tritium is a radioactive isotope of hydrogen with a half-life of 12.4 years. Therefore it is not present naturally to a sufficient amount and has to be produced artificially. In a fusion reactor, tritium is produced by the reaction between the breeder material and the neutrons coming from the plasma. The breeder material is a lithium-based compound. Natural lithium is composed of two isotopes, ^{6}Li and ^{7}Li with the relative abundances of 7.4% and 92.6%, respectively.

^{6}Li and ^{7}Li produce tritium according to the reactions

$$^7Li + n \rightarrow ^3T + ^4He + n - 2.8MeV \qquad 1.2$$

$$^6Li + n \rightarrow ^3T + ^4He + 4.8MeV \ . \qquad 1.3$$

The isotope ^{6}Li represents the main source of tritium, since it has a significantly higher cross section for the breeding reaction. For this reason, ^{6}Li has to be enriched up to 30-90%. In Figure 1–2 the cross sections of the reactions ^{6}Li(n, α) T and ^{7}Li(n, nα) T are reported [2] (Cismondi, 2011).
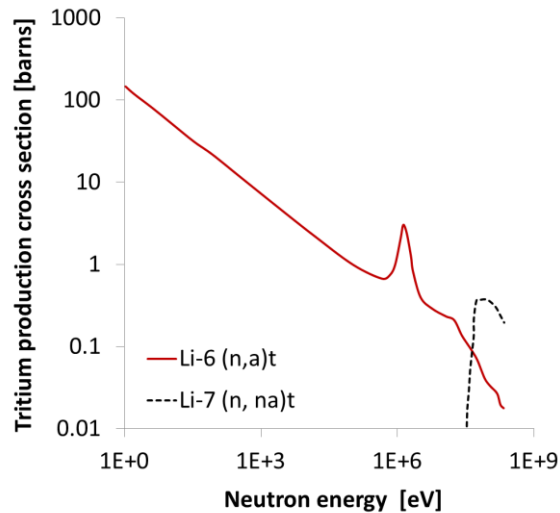
Figure 1–2: Cross sections of ^{6}Li and ^{7}Li for the production of tritium. Reproduced according to [2] (Cismondi, 2011).

A certain percentage of the neutrons produced inside the plasma is lost due to leakage and undesired absorption in the structural components of the reactor. For this reason, a neutron multiplier, placed in the breeder blanket, is required in order to assure a ratio of the tritium produced in the reactor over the tritium burned in the plasma greater than one. Such ratio is named Tritium Breeding Ratio (TBR). A neutron multiplier material releases two neutrons after the absorption of one neutron (n, 2n). Beryllium and lead are both neutron multiplier materials considered as candidates for fusion reactors [2] (Cismondi, 2011).

In Figure 1–3 a simplified scheme of a fusion reactor is shown. In the central zone, the reaction between deuterium and tritium generates plasma. The yellow region surrounding the plasma is the breeder zone, where breeder and neutron multiplier are located. Between the plasma and the breeder zone, the vacuum vessel is located. Neutrons generated from the D-T reaction overcome the vacuum vessel reaching the breeder zone where tritium is generated inside the breeder blankets. After that, tritium is extracted from the breeder zone to be carried into the plasma. The heat generated from the neutron interactions inside the blanket and the heat flux coming from the plasma into the blanket are then used for electricity production.

The plasma can be heated up via ohmic heating, neutral beam injection or radiofrequency heating. However, if the contribution of the energy released from the helium molecule slowing down inside the plasma is equal to the energy lost from the plasma, the external heating is no longer necessary. In this condition, the plasma is self-sustaining and it is in the state of ignition.
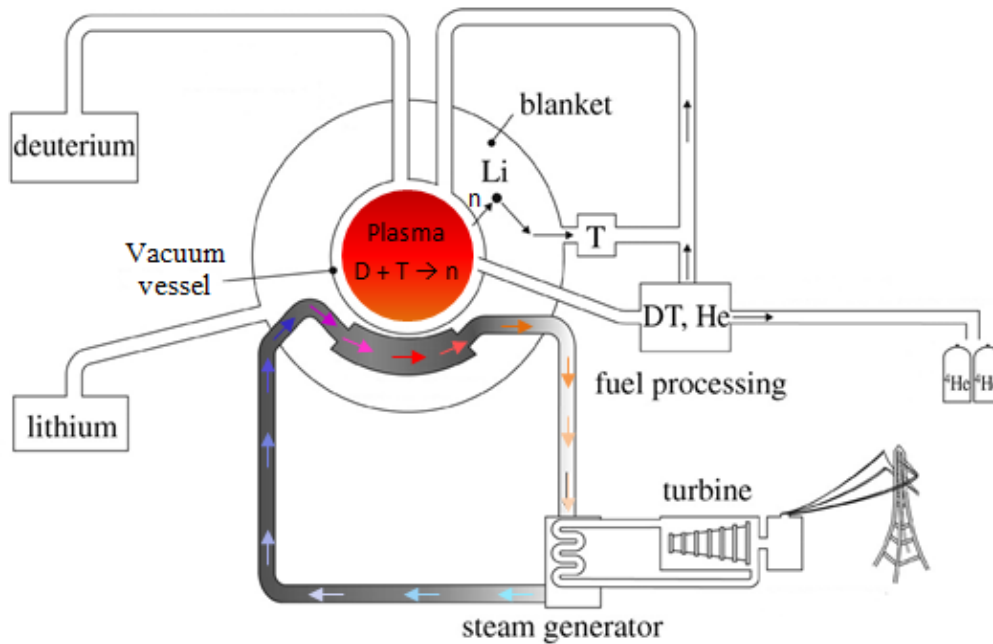
Figure 1–3: Simplified scheme of a fusion reactor.

In order to keep the plasma stable avoiding contacts with the walls of the vacuum vessel, the plasma has to be confined. A very effective technique to confine the plasma makes use of a torus shaped magnetic field to confine the plasma in a toroidal vacuum chamber. Moreover, to minimize the particle escape from the plasma, helical magnetic field lines around the torus are produced. Stellarator and tokamak are two different toroidal fusion machines based on the magnetic confinement of the plasma [3] (Xu, 2016).

The first commercial fusion station will be planned after the realization of two intermediate projects:

➢ ITER (International Thermonuclear Experimental Reactor), an international experiment involving Europe and 7 other countries, will be the first fusion device to produce net energy[2]. Currently, it is under construction in Cadarache. It will be used to test materials, components and technologies for a fusion reactor based on the tokamak confinement. The realization of the first plasma is planned on 2025.

➢ DEMO (Demonstration Power Reactor), the first DEMOstration Power Station, will guarantee to supply the power grid with a few hundred megawatts of electric energy demonstrating the possibility to work with a closed fuel cycle.

---

[2] This means that the energy generated by a fusion plasma pulse is higher than the energy amount required to power the machine system.

1.2 The breeder blanket concept

The breeding blanket is a key component of fusion reactors. It is designed to guarantee tritium fuel sustainability, power extraction and radiation shielding. Several breeder blanket concepts based on different breeding and structural materials, coolants and geometrical arrangements were developed to meet specific requirements. Six of these concepts will be tested in ITER in the form of Test Blanket Modules (TBMs) under fusion severe conditions [4] (Van der Laan et al., 2015).

In Figure 1–4, TBMs with their designated position in ITER are shown. The six TBMs are located, in pairs, in three ports close to the plasma, while the ancillary systems (pipes, extraction pumps, heat exchangers, molecular sieves etc.) are arranged away from the vacuum vessel.
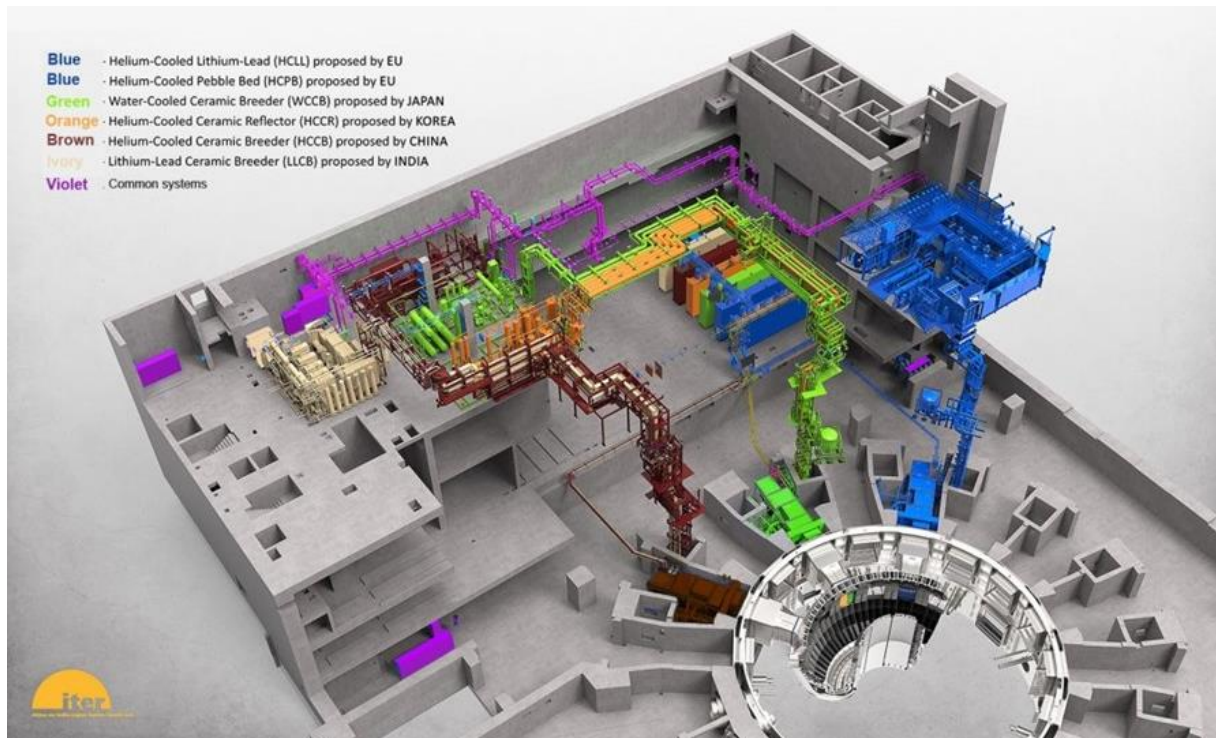
Figure 1–4: The six Test Blanket Modulus with their dedicated locations in ITER, [5] (https://www.iter.org/mach/TritiumBreeding), (credit: ITER Organization).

All breeder blanket concepts are based on a similar design [2] (Cismondi, 2011):

➢ An actively cooled first wall necessary to remove the heat flux deposited by the plasma.

➢ A breeder zone, where the neutronic energy is deposited and tritium is produced. The breeder zone can be either actively cooled when the breeder is a solid material (solid breeder blanket), or cooled by the breeder material itself when the breeder is in the liquid state (liquid breeder blanket).

➢ A shield in order to isolate the large magnets from the neutron flux.

Among the six TBMs, the Helium Cooled Pebble Bed Test Blanket Module (HCPB-TBM) is the solid breeder blanket concept under development at Karlsruhe Institute of Technology (KIT). In the HCPB-TBM, pebble beds of both lithium ceramic compound and beryllium are used for the tritium production and neutron multiplication, respectively. Pebble beds are accommodated inside the TBM box in so called Breeder Units (BU). The structural material is EUROFER, a reduced activation ferritic martensitic steel. Helium at a pressure of 8 MPa is used as coolant to extract the heat produced in the breeder zone, while Helium at 0.4 MPa is used as purge gas to extract tritium from the pebble beds. In Figure 1–5, the HCPB-TBM is shown together with a magnified view of the BU [6] (Hernandez et al., 2012).
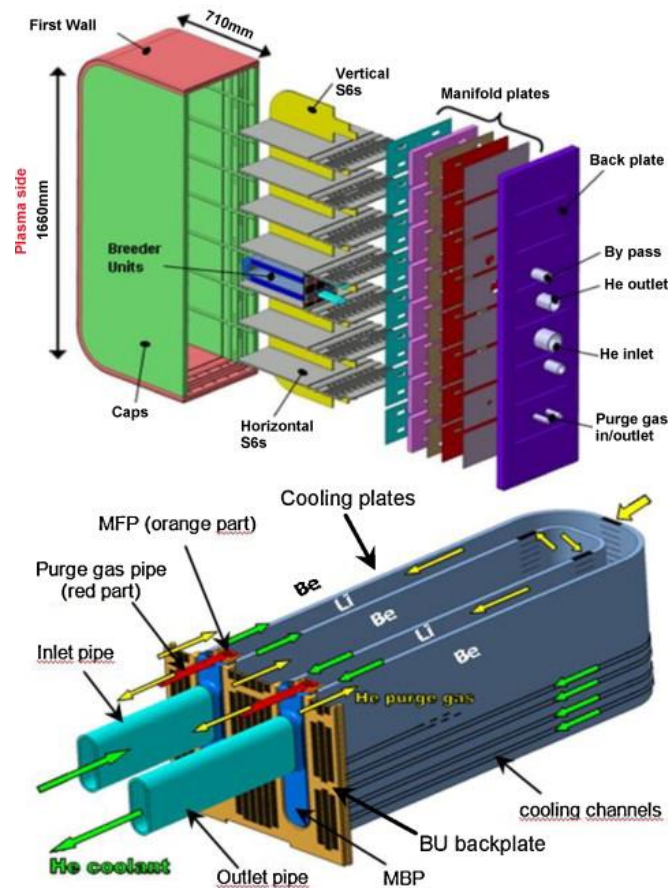
Figure 1–5: HCPB-TBM together with a magnified view of the BU, [6](Hernandez et al., 2012). Image reused with the permission of Elsevier.

As shown in Figure 1–5, beryllium pebble beds are physically divided from the lithium orthosilicate particles by Cooling Plates (CPs). CPs are two actively cooled Eurofer structures with a U-shape enclosing the lithium orthosilicate pebbles. CPs remove the heat produced in the lithium orthosilicate and beryllium pebble beds. The blue pipes shown in Figure 1–5 are the inlet and the outlet of the CPs for the coolant, while the red pipes are both outlets for the

helium purge gas. Purge gas enters into beryllium pebble beds from dedicated holes in the manifold (indicated in orange), then it flows into the lithium orthosilicate pebble bed and comes out through the purge gas pipes. The beryllium pebbles are surrounded by actively cooled Eurofer structures (shown in gray) such as the first wall and grids.

Pebbles are highly packed inside the box. The packing factor (PF) of pebble beds in a breeder blanket, defined as the ratio of pebbles volume to pebble bed volume, is about 64%. In this way the contact between pebbles and Eurofer walls is guaranteed and the heat transfer occurs without overheating during the entire life of the breeder material. High PFs assure safety conditions avoiding cracking of particles caused by vibration during operation. Cracking produces lack of contact between particles and walls in certain areas and generates sand of ceramic material that could obstruct the purge gas system.

1.3 Pebble Beds for solid breeder blankets

Pebble beds are assemblies of packed particles of a nearly spherical shape. The ceramic breeder pebbles are produced with a diameter range of about 0.25-1 mm, while the size of the beryllium pebbles is around 2 mm. The small sizes as well as the spheroidal shape are required to guarantee a homogenous filling of complicated blanket geometry, to minimize thermal cracking and volumetric swelling [7], [8] (Shikama et al., 2008; Ying et al, 2007).

Due to their discrete nature, pebble beds show a complex fully coupled thermomechanical behavior [9] (Ying et al, 2012). Under fusion relevant conditions, such as neutron irradiation, high heat flux and the cyclic loading due to the burn pulses of the plasma, the thermal expansion and irradiation-induced swelling of each particle generate stresses in the whole assembly. Particles rearrange themselves inside the box changing their packed state and accordingly the effective thermal conductivity of the bed. In turn, a variation of the thermal conductivity of the packed bed affects the temperature distribution changing the stress state inside the pebble bed once again.

Furthermore, a skeleton of solid particles and a matrix of interstitial gas coexist as multiphase material. Therefore, the heat transfer in the assembly is influenced by the skeleton-matrix combination. In this scenario the type of material, size, shape and density of the particles are of primary importance for the blanket design. These characteristics strongly influence the thermo-mechanical behavior of the bed which affecting project parameters like tritium inventory and the release rate [10] (Cristescu et al., 2007) and thus the functionality of the entire blanket.

Candidates for tritium breeder pebbles include several lithium-ceramic compounds e.g.: lithium orthosilicate (Li_4SiO_4), lithium metatitanate (Li_2TiO_3) and lithium metazirconate (Li_2ZrO_3). Beryllium metal or its compounds, such as $Be_{12}Ti$ or $Be_{13}Zr$ will be used as neutron multiplier. The characteristics of the pebbles are greatly influenced by the fabrication method. In Table 1–1, some fabrication processes and the resulting size, sphericity and density of the produced ceramic breeder pebbles are reported. Here, sphericity refers to the ratio between the maximum and the minimum dimension of a particle, while density represents the percentage of the theoretical density (TD) accounting for unavoidable pores generated inside pebbles during the fabrication process.

Table 1–1: Types of pebbles with fabrication process and some main characteristics

Material	Fabrication method	Particles Diameter (mm)	Sphericity	Density
Li_4SiO_4	Melting –spray [11] (Knitter et al., 2013)	~0.25-0.65	~1.05	~95%
Li_4SiO_4	Sol-gel [12] (Wu et al, 2010)	~1.2	~1.1	>75%
Li_2TiO_3	Sol-gel [13] (Hoshino, 2013)	~1-1.12	≤ 1.03	>85-65%
Li_2TiO_3	extrusion, spherodization and sintering [14] (Mandal et al, 2010)	~1.7-2	~1.02-1.1	~90%

Further details about fabrication methods and techniques to refine shape and density of particles are explained in the references reported in Table 1–1. In Figure 1–6 a comparison between pebbles produced by the melting-spray and sol gel methods are shown, respectively.
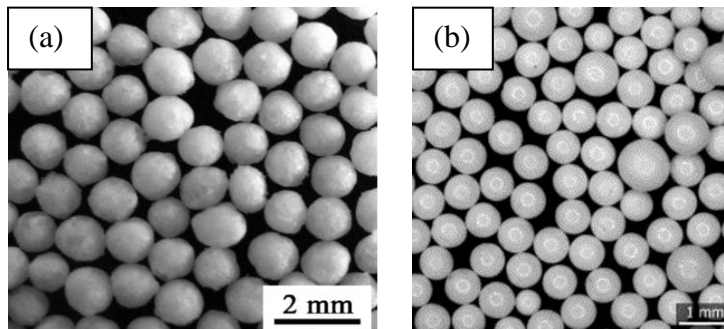

Figure 1–6: Li4SiO4 particles produced by: (a) the sol gel method [12] (Wu et al, 2010) and (b) the melting-spray process [11] (Knitter et al., 2013). Both images reused with the permission of Elsevier.

1.4 Motivation and goals

In the framework defining the complex coupled thermo-mechanical behavior of fusion pebble beds, a model describing the behavior of the individual particles and how their interactions affect the response of the granular bed is needed for the advancement of the breeder blanket design. While the Finite Element Method (FEM) is suitable to simulate large

volumes representing components with their real sizes, the Discrete Element Method (DEM) is a powerful tool to characterized discrete materials representing particles individually within a defined structure. DEM allows investigating pebble beds at granular level controlling parameters inaccessible in a FEM code such as pebble size, shape, packed state and modelling of the interstitial gas among particles. In this sense DEM is the only tool able to bridge the gap between microscopic and macroscopic behavior guaranteeing the representation of phenomena experimentally inaccessible.

In KIT an in-house DEM code exists for the investigation of the mechanical behavior of ceramic breeder pebble bed composed of perfect spherical particles. The aim of this work is to investigate the influence of the slight deviation from a perfect spherical shape of the currently produced pebbles on the mechanical behavior of pebble beds and to model the heat transfer in granular materials.

In order to investigate the influence of the particles shape, the in-house Discrete Element Method code has to be further extended. Since the real shape is more close to an oblate spheroid, an algorithm to create assemblies of ellipsoidal particles and to investigate their mechanical response has to be implemented. The main difference in the modelling of spheroidal and ellipsoidal particles is the need to represent the variation of the particle orientation during the compression. Furthermore, the curvature of the surfaces involved in the interaction between ellipsoidal particles and thus the contact area, changes with the position of the contact point, unlike spheres. However, depending on the method used to represent the ellipsoidal particles this problem can easily overcome.

In order to model the heat transfer in granular beds, a thermal DEM code has to be developed. The heat transfer in the bed depends on the thermal properties of the two component phases: solid pebbles and interstitial gas. In particular, the evaluation of the effective thermal conductivity of the bed is of primary importance to guarantee a correct estimation of the temperature field generated in the bed under neutron irradiation. The heat transfer in ceramic breeder pebble beds has to be simulated taking into account the influence of the interstitial gas, temperature of the system, compression state and level of neutron irradiation. Furthermore, since the gas is confined in the small gaps defined among particles, the implementation of the Smoluchowski effect to study the influence of the gas pressure on the thermal behavior of pebble beds is of primary importance. According to the Smoluchowski effect, the thermal conductivity of a confined gas decreases with decreasing pressure affecting in this way the effective thermal conductivity of the bed. Several works are

reported in literature providing analytical and experimental results accounting for the influence of the gas pressure in pebble beds. However, to my knowledge, nobody studied this effect by means of a DEM code until now.

1.5 Chapters description

In order to set a framework for the study reported in this thesis a literature review about previous studies, methods and related concepts is given in Chapter 2. After that the thesis proceeds with the description of the study related to the mechanical behavior of ellipsoidal particles under uniaxial compression. In Chapter 3 the method to generate an individual ellipsoidal particle and to create an assembly of packed particles is presented. By means of a DEM code, the interactions of each contact pair are studied and the mechanical behavior of the whole assembly under uniaxial compression is investigated. Finally, the influence of the aspect ratio and smoothness of the ellipsoidal particles on the macroscopic/microscopic behavior of the assemblies is discussed.

To represent the thermal behavior of pebble beds, an in-house thermal DEM code was developed. The thermal network model is introduced in Chapter 4, including sensitivity studies about temperature, gas pressure, compression state, packing factor, different solid materials and gas types. In Chapter 5 the application of the KIT thermal-DEM code to the breeder zone is reported modelling the temperature profile over the thickness of the bed as a function of the neutronic heating. Finally, the summary of the work is made in Chapter 6.

Chapter 2

Literature review

In this chapter, a literature review of works on the thermo-mechanics of pebble beds is presented. In the first section, the existing DEM approaches to study the thermo-mechanical behavior of granular materials are described, while in the second section experimental, analytical and numerical results about investigations on thermo-mechanics of ceramic breeder pebble beds are reviewed.

2.1 Discrete Element Method

The Discrete Element Method (DEM) is an essential numerical tool to investigate the micro-response of granular materials together with the macro-response of the granular assembly. It is suitable to investigate the behavior of a wide variety of discrete matters such as rock mechanics, powders and granular flows. Therefore it is employed in several fields such as: pharmaceutical industry, powder metallurgy, mineral processing and civil engineering. Here, an overview of the DEM approach with related possible applications is given first. Methods for the representation of non-spherical particles and the evaluation of their mechanical behavior are reviewed, and then a survey of the modelling of the heat transfer in granular materials is reported.

2.1.1 DEM overview

The DEM approach was first introduced by Cundall and Strack (1979) [15] to study the mechanical response of assemblies of packed particles. In DEM an individual particle is defined by its position inside the assembly, the size, the shape and its orientation if the particle is not spherical. A dedicated contact algorithm can provide information about contact forces acting among particles. Newton's equations of motion are then used to update positions and velocities of the particles. Both dynamic and static analyses of granular media can be carried out by means of this method. In this regard, one of the first studies was carried out by Herrmann and Luding (1998) [16].As reported in [16] (Herrmann and Luding, 1998), [17] (Thornton et al., 1998) and [18] (C. L. Martin et al., 2003), particle deformation, size segregation and force distribution can be numerically obtained by means of DEM tool. In 2000 Lu et al. [19] investigated the thermal creep in ceramic breeder pebble beds with a DEM code, while Clearly (2000) [20] performed a numerical campaign on the behavior of industrial particle flows. The DEM approach is crucial to study the macroscopic behavior of granular

media as a result of the interaction among particles gaining important information, such as the yield surface (Redaz and Fleck, 2001 [21]), particle rearrangement during compaction (Martin, 2004 [22]) and the crush probability (Marketos and Bolton, 2007 [23]). An et al. in 2007a [24] and in 2007b [25] investigated the contact force distribution inside pebble beds for assemblies surrounded by rigid walls, while in the same year Gilarbert et al.[26] studied the behavior of assemblies of packed particles in a periodic configuration.

In the same period, a DEM code was developed in KIT to study the mechanical behavior of ceramic breeder pebble beds under uniaxial compression (Gan, 2008 [27]; Gan and Kamlah, 2010 [28]; Gan et al., 2010 [29]; Zhao, 2011[30]; Annabattula et al., 2012a [31] 2012b [32]; Zhao et al., 2013 [33]; Pupeschi et al., 2016 [34]). First, the mechanical behavior of monosized spherical packed particles in a periodic boundary configuration was investigated by Gan (2008) [27] and Gan and Kamlah (2010) [28]. The micro mechanical behavior was investigated and its influence on the macroscopic behavior of the whole assembly was studied [28] (Gan and Kamlah, 2010). The code was used to study the influence of relevant parameters such us packing factor [28] (Gan and Kamlah, 2010) [30] (Zhao, 2011) [31] (Annabattula et al., 2012a), friction coefficient [30] (Zhao, 2011) [31] (Annabattula et al., 2012) and shear stiffness [30] (Zhao, 2011) as well as the effect of pebble failure in the macromechanical response [32] (Annabattula et al., 2012b) [33] (Zhao et al., 2013). With further extensions of the code, both the influence of the wall on the packing structure of the pebble beds [29] (Gan et al., 2010) and the particle size distribution on the mechanical behavior [31] (Annabattula et al., 2012a) were investigated. Recently, the KIT_DEM code was slightly modified [34] to investigate the cycling mechanical behavior of ceramic breeder pebble beds. Discussions about numerical results are reported in Section 2.2, which is dedicated to the overview of the numerical/experimental campaign carried out to characterize the behavior of ceramic breeder pebble beds.

Together with mechanical DEM studies of packed spherical particles, DEM modelling of non-spherical packed particles has received significant attention over the last 20 years. The awareness of the strong influence of the particle shape on the dynamic of granular systems raised the interest of the community in these studies. In the next section, a summary of different approaches for the representation of non-spherical particles together with the algorithms for the contact detection are presented.

2.1.2 Non-spherical particles in a DEM code

The numerical representation of the mechanical behavior of packed non-spherical particles requires an accurate analysis of both the contact algorithm and the method to determine the particles' orientation. While the contact algorithm strictly depends on the method chosen to represent the desired particle shape, the orientation is mainly defined by Euler angles (Goldstein et al., 2002) [35] or quaternions (Evans and Murad, 1977) [36]. The first approach suffers from the gimbal lock singularity. Therefore the second method is preferred for practical DEM implementations. In the following, common methods for the representation of non-spherical particles with the related contact algorithms are described.

Ellipsoids

The simplest non-spherical particle shape to be represented with a DEM code is the ellipsoid. Such particles can be generated using a parametric and/or an algebraic equation (Lin and Ng, 1995[37], 1997 [38]; Ouadfel and Rothenburg, 1999 [39]; Mustoe and Miyata, 2001[40]; Donev et al., 2005 [41]; Wynn, 2009 [42]; Yan et al., 2010 [43]; Baram and Lind, 2012 [44]; Zheng et al., 2013[45]). The individual pebble is characterized by its position in space and the length of the three principal axes. For non-spherical particles, the curvature of the contact surfaces and thus the contact area, changes with the position of the contact point. Therefore, the major challenge in modelling ellipsoids in DEM is the implementation of an efficient and stable contact detection algorithm. In 1999 Ouadfel and Rothenburg [39] developed an algorithm to determine the contact between two ellipsoids based on the intersection of their geometrical figures. An alternative to the geometrical intersection method is the geometric potential concept, which was developed, for three-dimensional geometry, by Lin and Ng in 1995 [37]. The approach is based on the geometric potential concept of ellipsoids. For two contacting ellipsoids, the two points with the lowest geometric potential mark the penetration in the related contacting particle. If the two points are inside the contacting particle, the two ellipsoids are in contact and the middle point of their connecting line identifies the contact point. In the same study [37], Lin and Ng (1995) developed another method called common normal method, which is based on two sets of equations: constraining equations guaranteeing that the contact point is on the particle surface and target equations that detect the minimum distance in the contact pair. An iterative method is used to solve the two sets of equations. This scheme entails high computational times frequently resulting in convergence problems. However, compared to the geometric potential method, the common normal method better defines the mechanics of the contact.

Super-quadrics

A general approach to represent non-spherical particles is the so-called super-quadric equation. The super-quadric equation was introduced by Barr (1981) [46] to describe particles with convex and concave shapes. In the equation

$$f(x,y,z) = \left(\left(\frac{x}{a}\right)^{\frac{2}{\varepsilon_2}} + \left(\frac{y}{b}\right)^{\frac{2}{\varepsilon_2}} \right)^{\frac{\varepsilon_2}{\varepsilon_1}} + \left(\frac{z}{c}\right)^{\frac{2}{\varepsilon_1}} - 1 \qquad \text{2.1}$$

a, b and *c* are the half-lengths of the principal particle axes, while ε_1 and ε_2 control the shape of the particles' cross section in the y-z and x-z planes, respectively. Figure 2–1 exemplarily shows different particle shapes obtained changing ε_1 and ε_2.
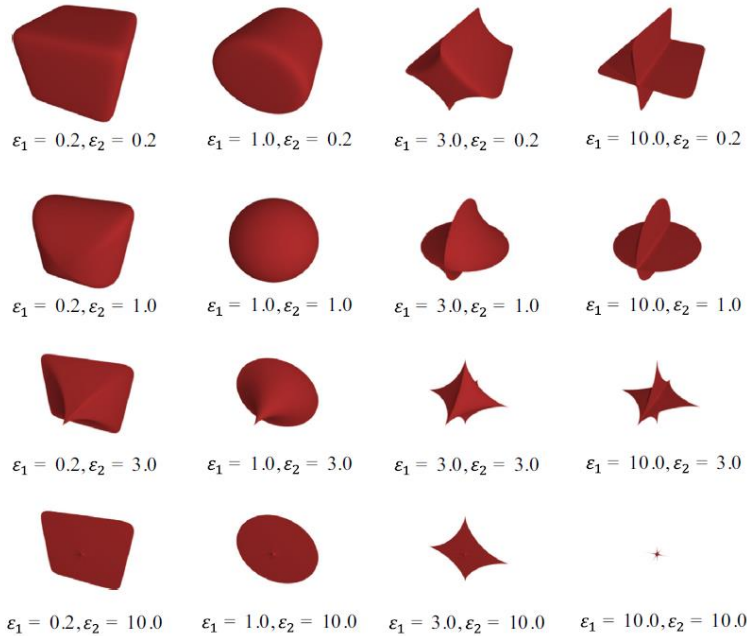

Figure 2–1: Examples of different particle shapes obtained changing ε_1 and ε_2 in the super-quadric equation, [49] (Lu et al., 2015). Image reused with the permission of Elsevier.

Spheres and ellipsoidal particles are obtained setting $\varepsilon_1 = \varepsilon_2 = 1$ and varying the length of the three main axes. Using a continuous function to represent the surface of the particles, non-linear iterative approaches are needed to detect the contacts among pebbles. The scheme is similar to the algorithm proposed by Lin and Ng (1995) [37] and described in the previous subsection on ellipsoids, therefore the same convergence problems are observed. In terms of contact detection, an alternative is represented by the so-called discrete function proposed by Williams and O'Connor on 1995 [47]. In this method, the surface of the particles, generated by the super quadratic method, are discretized by individual points. Using the geometric potential method, when a surface point of a particles lies inside the second particle, this is detected as contact (Hogue,1998) [48].

The discretization can be uniform or adaptive. The uniform discretization is suitable for symmetrical particles since points are uniformly distributed and equally spaced, while the adaptive discretization guarantees a different point distribution for an accurate representation of corners and edges [49] (Lu et al., 2015). Examples of uniform and adaptive discretization are shown in Figure 2–2(a) and (b), respectively. Even if this is a promising approach, open issues such as the correct number of points to be used, their distribution on the surface to guarantee a sufficient accuracy and a more suitable method to efficiently detect contact points need to be addressed.
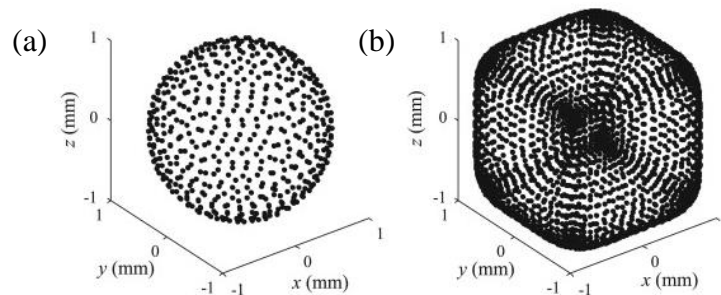

Figure 2–2: Particle shape representation using the discrete function: (a) uniform discretization (b) adaptive discretization, after [49] (Lu et al., 2015). Image reused with the permission of Elsevier.

Multi-Sphere

The Multi-Sphere (MS) method is the most popular approach in the DEM community to represent non-spherical particles (Ning et al., 1997 [50]; Favier et al., 1999 [51], 2001[52]; Thornton et al., 1999 [53]; Kafui and Thornton, 2000 [54]; D. Markauskas et al., 2010 [55]). In the MS method several spheres called "primary spheres" are clustered to form the desired geometry. In particular, the size, the number and the overlap of the spheres can be tailored to obtain the desired shape. To keep the geometry fixed, the relative position between the primary spheres of the clustered particle must not change. In Figure 2–3 various ellipsoidal shapes consisting of different clusters of primary spheres are shown. The main advantage of this method is the possibility to apply the fast and robust contact detection algorithm for spheres to the contact between primary spheres constituting different particles. Indeed, forces and torques acting between non-spherical particles are detected between the primary spheres clustering the related particles. Then, they are vectorially added and applied in the center of mass of each clustered particle. Due to the possible overlaps among primary spheres, composing the individual non-spherical particle, the artificial excess of mass has to be removed and the moment of inertia adjusted. Ferellec and McDowell (2008 [56], 2010a [57], 2010b [58]) adjusted the density of the primary spheres to correct the mass and moment of inertia of the composed particle. In 2013a [59]and 2013b [60], Parteli proposed a new

method. He divided the overlap between two primary spheres in two caps to remove the mass and the moment of inertia of the overlaps from the total amount of the respective quantity evaluated as the sum of the clustered primary spheres.
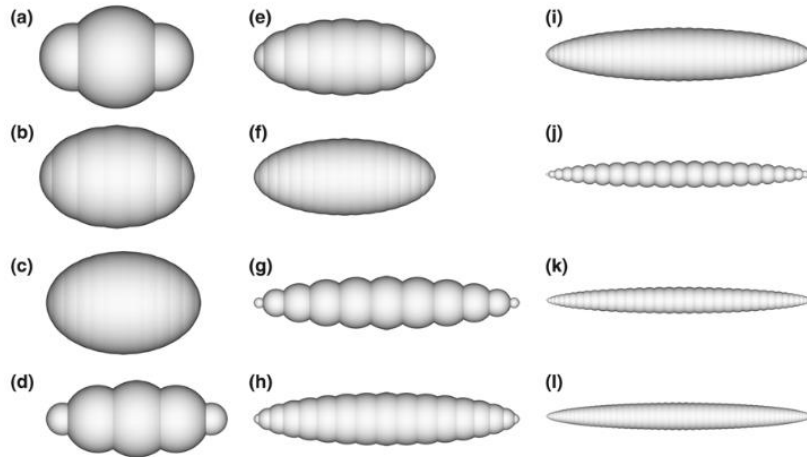

Figure 2–3: Representation of ellipsoids with various aspect ratios combining a different number of primary spheres with a defined radius [55] (Markauskas et al., 2010). Image reused with the permission of Springer Nature.

Depending on the desired level of surface smoothness, a different number of primary spheres are glued together. Since the contact between two composed particles is reduced to contacts between the primary spheres, it can happen that a primary sphere of a composed particle is in contact with two or more primary spheres of the contacting clustered particle. This, and more generally the lack of convexity of the composed particles raises a concern with respect to the MS method, namely the presence of multiple contact points between clustered particles and their detection.

Kruggel-Emden et al. (2008) [61], demonstrated that such multiple contacts may generate an unphysical behavior of the assembly leading to large deviations between numerical and experimental results. To get rid of this problem, Kodam et al. (2009) [62] proposed to change the contact law by adjusting the value of the elastic contact stiffness, the damping coefficient and the force model according to the number of primary spheres composing a particle and their overlaps. An easier and effective method, without variations of the force model's parameters was developed by Höhner et al. (2011) [63]. At each time step the incremental normal and dissipative force are divided by the number of multi contacts, while the increment of the tangential force is not directly updated. The tangential force is limited to the minimum value between the shear and the friction force. The friction force is already adjusted since it is evaluated as a function of the normal force. Therefore, only the increment of the shear force has to be divided by the number of the multi contact at each time step.

Other methods

Non-spherical particles can be composed of non-spherical geometric elements. Recently, the so-called 'spherosimplices' method became established. With this method, complex geometries are generated defining a skeleton using linear segments, points etc. Then, the shape of the particle is generated moving a sphere around segments and points composing the skeleton (Alonso-Marroquín et al., 2009 [64]). In this case, the most suitable of the contact algorithms described above can be applied as a function of the simulated particle shapes.

For non-spherical particles characterized by corners, edges and flat surfaces, the representation via polygons and polyhedrons is frequently proposed (Hart et al., 1988 [64]; Hopkins, 2014 [66]). As for the other methods, when non-spherical particles are used, the contact algorithm is the most difficult challenge to be faced. The contact detection algorithm has to account for all the combinations of elements such as corner–corner, corner–edge, corner–face, edge–edge, edge–face and face–face. The so-called 'common plane' (CP) algorithm was proposed (Cundall, 1988 [67]; Nezami et al., 2004 [68], 2006 [68]; Zhao et al.,2006a [70], 2006b[71]) to improve the computational efficiency of the algorithm.

2.1.3 Heat transfer modelling for ceramic breeder pebble beds

Pebble beds are multiphase materials in which both the solid and the gas phase filling the voids among particles coexist. The heat transfer inside pebble beds depends on the thermal properties of the two phases as well as on the overall system properties (e.g. gas pressure, temperature, mechanical state etc.). The solid to gas thermal conductivity ratio (k_s/k_g) influences the heat transfer distribution between the solid and the gas phase. The heat flows mainly through paths with higher thermal conductivity. Therefore, the heat transfer is uniformly distributed between the two phases when the ratio k_s/k_g is low; otherwise the heat flows mainly through the contacts between the particles [72] (Abou Sena et al., 2005). Thus, a variation of the compression state of the bed influences the heat transfer among particles especially when the ratio k_s/k_g is high. This is because varying the compression state, the number of contacts and the dimension of the existing contact areas change influencing the heat transfer and in turn the effective thermal conductivity of beds.

Heat transfer models describing the interactions among particles taking also into account the gaseous contribution are needed to investigate the heat transfer in granular matters. In particular several mechanisms have to be considered: the conduction within the solid material, conduction through the contact area between contacting particles, conduction in the gas phase,

gas convection and radiation between particles. However depending on the application field, involved materials and boundary conditions, some of the heat transfer mechanisms can be considered secondary or even neglected.

In the breeder beds, a purge gas flows among the packed pebbles with a low mass flow rate ~0.4 kg/s in order to guarantee the tritium extraction [73] (Franza et al., 2013). Considering the low mass flow rate, the gas can be considered as quasi-stagnant and thus the gas convection neglected since it will just slightly contribute to the heat transfer in the ceramic breeder beds. Besides, the contribution of thermal radiation is also marginal due to the involved small particle sizes (~0.25-0.65mm, [11](Knitter et al., 2013)) and the high packing factor (~64%) characterizing the breeder pebble beds. The contribution of the heat radiation increases with the particle temperature and size [74] (Asakuma et al., 2014), while it reduces with the increase of the bed density [75] (Lu et al., 1995). A high packing factor increases the absorption of radiation in the packed structure reducing the radiative bed density [75] (Lu et al., 1995). In [74] (Asakuma et al., 2014) it has been reported that the thermal radiation in packed beds is negligible, in the temperature range of 0-1440 °C, for particles with a diameter less than 1 mm. In the same study, the contribution of thermal radiation was found to be appreciable above 400 and 150 °C for particles with a diameter of 10 and 100 mm, respectively. In 2016 Wu et al.[76] found a negligible influence of the thermal radiation below 130 °C for graphite spheres of 60mm in diameter with an average packing factor of 61%. Therefore, the conduction within the solid material, through contact points and the conduction in the gas phase are expected to be the relevant mechanisms characterizing the heat transfer in ceramic breeder pebble beds. In the following, a related overview is given (see also Moscardini et al., 2018 [77]).

Batchelor and O'Brien (1990) [78] developed a theory to evaluate the heat transfer in granular materials. They derived the effective conductivity of a stationary granular material through which a stationary transport of heat or electricity exists. They considered a granular assembly composed of randomly arranged spheres in contact, or nearly in contact, immersed in a uniform matrix. The heat transfer was evaluated accounting for two main types of contacts: particles touching each other or with a separation gap. In the theory, it is supposed that the main contribution to the heat flux occurs through a certain percentage of the surfaces of the two contacting particles. Several works reported in literature [79] (Yun and Evans, 2010), [80] (Kanuparthi et al., 2008), [81] (Gan et al., 2014) use this theory to study the heat transfer in granular matters by means of a DEM code. Simulating the granular material as an

assembly of packed particles, each thermal contact is defined as a series circuit of three resistors. The three resistors identify the resistance to the heat transfer inside the two particles and in the contact region, which can be a separation gap or a contact area. Taking contacting particles as nodes, this defines a 3D random network model that describes the heat transfer in the whole assembly accounting for the conduction inside the solid material, through the contact region and in the gas phase. In [79] (Yun and Evans, 2010) and [80] (Kanuparthi et al., 2008) the Gauss–Seidel method was used to compute the evolution of the temperature in the linear system, while in [81] (Gan et al., 2014) a transient method was employed applying a thermal diffusion time to describe the characteristic time to transfer the heat between pebbles. In this framework, neither of the existing studies reported in literature take into account the influence of the gas pressure on the heat transfer in granular materials. In granular materials, the filling gas is confined in small gaps among the packed particles. According to the kinetic theory of gases, the thermal conductivity of an unconfined gas is independent of its pressure, while for a confined gas the thermal conductivity of the gas decreases with the pressure when the mean free path of the gas molecule reaches the dimensions of the confining space. This is the so-called Smoluchowski effect and it strongly influences the thermal behavior of granular materials [82] (Smoluchowski, 1924). In particular, as the mean free path is inversely proportional to the gas pressure, the reduction of the gas pressure may lead to an increase of the mean free path up to the order of magnitude of the confining dimension. In turn, with reduction of the gas pressure, the gas becomes more rarefied and the interaction between the gas molecules becomes more sporadic. In the extreme case, the heat is just transferred by interaction of the gas molecule with the confining boundaries. A parameter representing the likelihood of the molecule interactions is the Knudsen number defined as

$$K_n = \Lambda/L \qquad\qquad 2.2$$

where Λ [m] and L [m] are the mean free path and the geometrical dimension of the confining space, respectively. When K_n increases, the probability of interaction between gas molecules decreases defining three gas regimes [83] (Raed, 2013):

- Continuum regime: For $K_n < 0.001$ the heat in the gas is transferred by molecular interactions and the gas thermal conductivity as well as the thermal conductivity of the packed granular system is independent of the gas pressure. This is defined as the continuum regime, where the gas thermal conductivity is equal to its bulk value (unconfined gas).

- Transition regime: For $0.001 < K_n < 10$ the gas thermal conductivity and thus the effective thermal conductivity of the granular assembly drop as the gas pressure decreases. Decreasing the gas pressure the effective thermal conductivity of the bed drops, because the mean free path gradually reaches the order of magnitude of the dimension of the confining space, and the gaseous thermal transfer becomes less effective.

- Free molecule regime: For $K_n > 10$ the collision between molecules can be neglected, and the thermal energy is transferred by the interaction of the gas molecule with the confining surfaces (very rarefied gas). This regime is called free molecule regime. The thermal conductivity of the gas and thus the effective thermal conductivity of the assembly are low and again are independent of the gas pressure.

The combination of the three regimes provides the well-known S-shape curve, which is the result of the reduction of the gas thermal conductivity with its pressure. Figure 2–4 exemplarily shows some S-shape curves representing the nitrogen thermal conductivities at room temperature in function of the gas pressure, for different pore sizes enclosing the gas. The curves were reproduced according to the analytical studies reported in [83] (Raed, 2013). The plateau at high and low pressures identifies the continuum and the free molecule regimes, respectively, while for intermediate values of the gas pressure the transition region is found.

Without the implementation of the Smoluchowski effect, the thermal conductivity of the gas is always overestimated determining an unrealistic temperature field in the bed. Therefore, in order to properly evaluate the heat transfer in the breeder beds, the implementation of the gas pressure dependence is required.
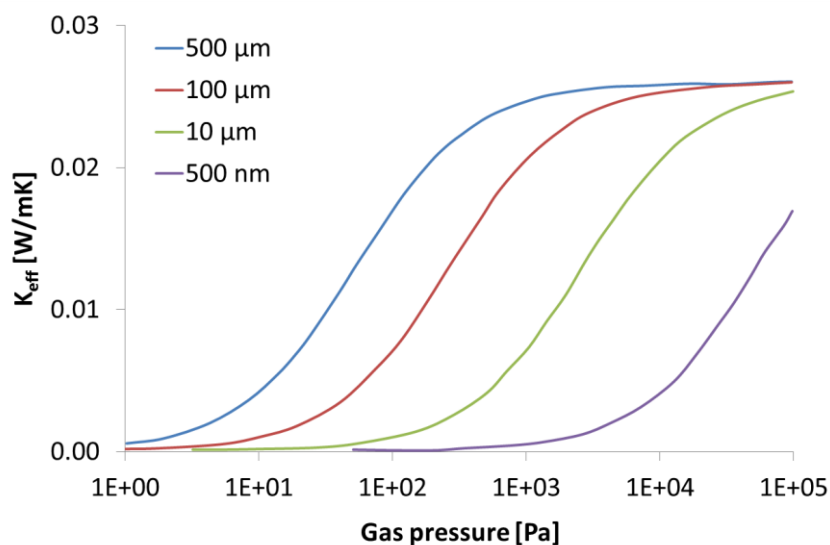

Figure 2–4: Smoluchowski effect for the nitrogen thermal conductivities at room temperature in function of the gas pressure and for different pore sizes. Reproduced according to results reported in [83] (Raed, 2013).

2.2 Overview of the experimental/numerical studies on the thermo-mechanics of ceramic breeder pebble beds

The thermo-mechanical behavior of pebble beds is affected by several parameters such as the mechanical state, packing factor, gas type, solid material, gas pressure, temperature etc. Therefore, the effective mechanical and thermal properties of a granular material cannot be derived from the properties of a single pebble or its base material. For this reason, experimental and numerical investigations of pebble beds are both essential to understand the pebble bed thermo-mechanics. In this section, an overview of the related experimental and numerical investigations to characterize the thermo-mechanics and the effective properties of ceramic breeder pebble beds is given.

2.2.1 Studies of mechanics in ceramic breeder pebble beds

Aiming to characterize the mechanical response of breeder beds, Uniaxial Compression Tests (UCT) have been carried out on assemblies of packed particles by using different experimental set-ups, materials and boundary conditions [34] (S. Pupeschi et al.,2016), [84]-[91] (Ying et al., 1998; Lu et al., 2000; Reimann and Wörner, 2001; Piazza et al., 2002; Reimann et al., 2002; Buhler and Reimann, 2002; Dell'Orco et al., 2016; Zhang et al., 2016). In the UCT, the pebbles are placed in a cylindrical container with a H/D ratio less than 1. This is to avoid that the increase of the effective constraints at the cylindrical wall (due to friction) leads to a non-uniform compression state along the bed's thickness. Moreover, the radial dimension of the container should be much larger than the diameter of the individual pebbles in order to assure negligible wall effects on the packing structure and to obtain a mechanical response of the bed governed by its bulk behavior. Furthermore, a sufficient number of particles has to be used to guarantee a representative behavior.

During the UCT, the pebbles contained in the cylindrical cavity are compressed in the axial direction by a piston connected to a testing machine. As result of the test, the macroscopic bed strain, corresponding to the variation in percentage of the pebble bed height, is determined as a function of the macroscopic stress applied axially on the bed cross-section. The characteristic mechanical behavior of a pebble bed exhibits non-linear elasticity and in addition with an irreversible residual strain after the unloading, which is the result of a significant rearrangement of the particles inside the bed. Figure 2–5(a) shows the stress-strain curves obtained from UCT experiments carried out with metatitanate breeder pebble beds at room and high temperature [88] (Reimann et al., 2002). When the ceramic breeder is

compressed at high temperature (over 600 ºC), thermal creep becomes evident determining an increase of the strain under a constant stress.
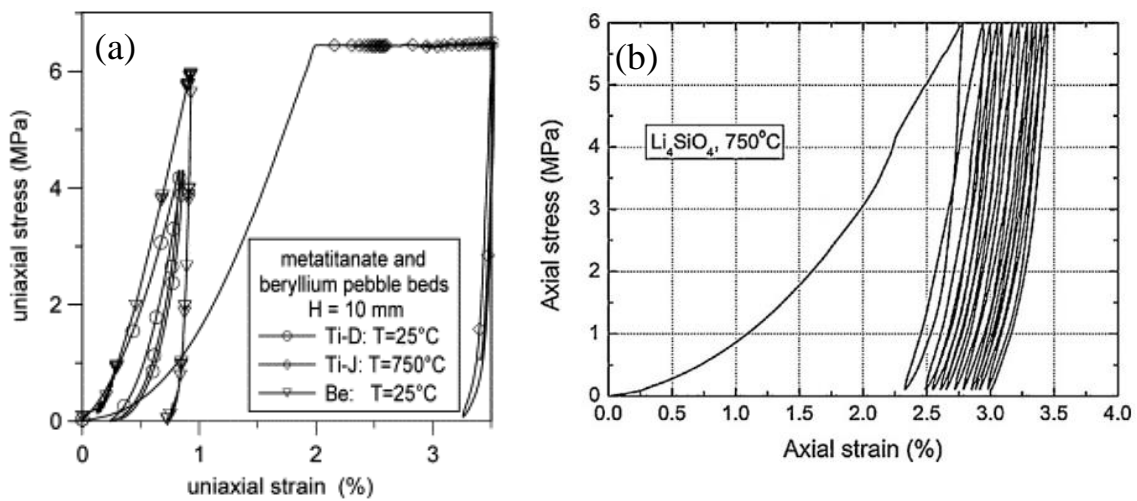

Figure 2–5: Typical stress-strain curves obtained from UCT experiments. a) Experiments carried out with fusion pebble beds at different temperatures, [88] (Reimann et al., 2002). b) Cyclic behavior of lithium orthosilicate at high temperature, [91] (Zhang et al., 2016). Both images reused with the permission of Elsevier.

UCT experimental campaigns have been carried out in [91] (Zhang et al., 2016) and [34] (S.Pupeschi et al., 2016) to investigate the mechanical behavior of pebble beds under cycling loading. Figure 2–5(b) exemplarily shows the mechanical behavior of a ceramic breeder material under cyclic loading at 750°C [91] (Zhang et al., 2016). When a granular material is cyclically loaded, the largest part of the irreversible residual strain is generated during the first few cycles [91] (Zhang et al., 2016); then smaller increments of the bed compaction occur as the cycling proceeds [34] (S.Pupeschi et al., 2016).

In order to reproduce numerically the mechanical behavior of pebble beds, the Discrete Element Method (DEM) and continuum approaches can be used. In the continuum approach, the effective properties of the beds are implemented in a Finite Element Method (FEM) code to simulate its macro-response. In [90] (Dell'Orco et al., 2016) the developed code was validated with experimental results obtained with the HELICA and HEXCALIBER mock-ups. In [92] (Ying et al., 2012) the continuum approach was found to adequately represent the macroscopic thermomechanical behavior of breeder beds. The continuum approach allows simulating large volumes giving information about the behavior of the whole investigated structure. However, the individual components of the investigated structure have to be simulated as continuum materials. Therefore, when pebble beds are simulated as continuum materials, the knowledge of the effective properties of the bed and how they are affected by the micro-mechanisms generated during the operation, is essential for a correct estimation of

the bed behavior. In this sense the DEM tool is necessary to evaluate the effective properties and the behavior of the bed as result of the interaction among particles accounting for all micro thermo-mechanical mechanisms. Simulating the individual interactions at the particle scale, it is possible to investigate the influence of parameters such as the compression state, packing factor, friction coefficient, particle size distribution and particle shape. In this sense, in addition to the macroscale stress-strain response of the assembly, relevant information about crush probability, void fraction distribution, yield surface, and force distributions are achievable.

The DEM approach for fusion relevant applications was first used by the University of California Los Angeles (UCLA) to study the micro mechanics of breeder beds [85] (Lu et al., 2000). In this work, the thermal stress induced by the thermal expansion of the particles composing a constrained bed was modelled and compared with experimental data. The variation of the effective modulus of deformation was determined as a function of the thermal cycles and compared with the experimental results. In the first cycle, numerical results were found quite in line with the experiments. However, due to the breakage of particle during the experiments a large error between simulations and experiments occurred in the successive cycles. Later on, in [24] (An et al., 2007a) and [25] (An et al., 2007b), the mechanical behavior of rigid spheres packed inside containers with elastic walls and compressed in axial direction was investigated. In [24] (An et al., 2007a) the mechanical performance of breeder pebble beds under the thermal creep deformation was investigated. Results demonstrated that the creep strain rate of pebble bed is higher than bulk material at stationary. In [25] (An et al., 2007b) it was found that both the packing factor as well as the bed geometry can influence the mechanical response of the bed. For the simulated bed geometries, the wall effect on the mechanical behavior of the pebble beds was found to be negligible compared to the inner structures of the pebble force chains. Furthermore, from statistical data of the internal contact forces, it was found that the coordination number of the pebbles, which is defined as the average number of contacts per particle, determines the main variations in the overall behaviors of the pebble beds.

In more recent works at UCLA, an open-source DEM code was used to study the mechanical behavior of monosized packed assemblies with PBC under uniaxial compression [93], [94] (Van Lew et al., 2014 and 2015). In particular, in [93] Van Lew et al. (2014) studied the thermo-mechanics of breeder beds experiencing pebble failure. It was found that the effective thermal conductivity rapidly decreases when the percentage of failed pebbles in

the bed increases. As pebbles fail, the inter-particle forces drop leading to an increase of the temperature in the neighboring pebbles, which results in a reduction of the effective thermal conductivity. In [94] Van Lew et al. (2015) investigated the influence of Young's modulus on the mechanical behavior of pebble beds. Due to the different fabrication processes, pebbles show different microstructures and thus different mechanical behaviors. In this study, the authors carried out crushing experiments on different pebbles determining a wide range of crush loads. The different crush loads were associated to different Young's moduli, which were defined as a reduction of the highest value reported in literature for highly sintered pellets of the same material. The obtained values were applied into the DEM simulation. When the Young's modulus is reduced, a more compliant behavior of pebble beds with smaller peak contact forces in beds and thus fewer crushed pebbles are predicted.

At KIT, an in-house DEM code is under development since 2008 to investigate the mechanical behavior of ceramic breeder pebble beds. In 2008, Gan[27] and in 2010 Gan and Kamlah [28] implemented the Random Close Packing (RCP) algorithm for the generation of random and densely packed assemblies of monosized spherical particles. The method is a purely geometric approach based on the RCP described in [95] (Jodrey and Tory, 1985) with a periodic boundary configuration. The approach guarantees reaching a Packing Factor (PF) of approx. 64%, being consistent with the reference value of the actual European breeding blanket design. The generated PF is defined as the fraction of the total volume occupied by the particles over the volume of the virtual box in which particles are packed. With the implementation of periodic boundary conditions, the packed state of the assembly refers to the bulk zone of pebble beds. In the same study [28] (Gan and Kamlah, 2010), the DEM method to compress in uniaxial direction the generated assemblies was presented. The uniaxial macroscopic strain ε is gradually applied up to the maximum value, then ε is gradually removed until the stress approaches zero. The DEM simulations conducted with this code accurately reproduced the characteristic bulk mechanical behavior of fusion ceramic breeder pebble beds giving results in good agreement with the UCT experimental outcomes [28] (Gan and Kamlah, 2010). During their studies Gan [27] (2008) investigated the microscopic behavior of the assemblies in terms of internal force distributions defining correlations to determine the average normal force, maximum force and average number of contacts as a function of the hydrostatic pressure. In 2010 Gan et al. [29] further extended the code in order to study the influence of the walls on the packing structure of pebble beds. Rigid wall conditions were simulated and particles were packed into a cylindrical container to compare the numerically obtained packing structure with X-ray tomography results [29] (Gan et al.,

2010). In Figure 2–6, the packing factor distribution obtained with the numerical simulation (red line) for a highly packed assembly of monosized particles along the main axes of the cylinder container is compared to the packing structure obtained in the experiments (gray dots). The numerically result was found to accurately reproduce the packing structure obtained with the X-ray tomography. In the upper and bottom regions, the large fluctuations of the void fraction show the influence of the walls on the packing factor which stabilizes in the bulk region. The fluctuations are generated due to the ordered packing structure developed near the walls.

In 2010 Zhao [30] and then in 2013 Zhao et al. [33] further extended the code to investigate the influence of friction coefficient, shear stiffness and pebble failure on the macroscopic mechanical behavior of assemblies of packed spheres. A strong influence of the friction coefficient and shear stiffness was discovered. A high friction coefficient results in a stiffer behavior while, when the shear stiffness decreases, a softer mechanical behavior was determined. It was found that the crushing events of pebbles induced instabilities in the overall stress–strain responses. Furthermore, no significant localization of crushed pebbles during the failure propagation was observed.
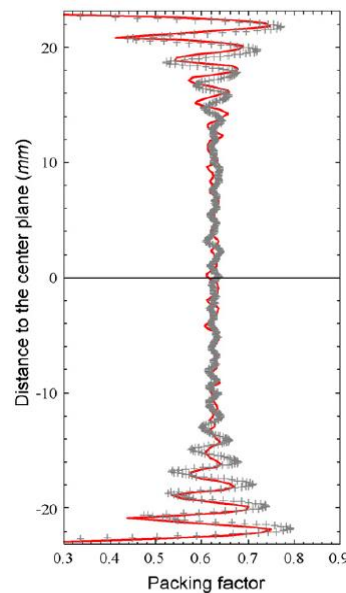

Figure 2–6: Comparison between numerical (red line) and experimental results (gray dots) of the packing factor distribution of a highly packed assembly of monosized particles along the main axes of the cylinder container, [29] (Gan et al., 2010). Image reused with the permission of Elsevier.

In 2012 Annabattula et al. [31] further extended the code in order to simulate assemblies of packed particles with different radius. The obtained results showed a stiffer behavior of assemblies composed of monosized particles compared to binary and polydispersed

assemblies with the same initial PF. As for monosized particles, the initial PF was found to strongly influence the behavior of the bed. Assemblies with higher PF show a stiffer behavior with a smaller residual strain after unloading. Results of this numerical campaign are reported in Figure 2–7. Figure 2–7(a) shows the influence of the packing factor "η" on binary assemblies. In Figure 2–7 r* is the ratio between the radius of the smaller particle over the radius of the larger particle, while V* is the ratio between the volume occupied by larger particles over the volume occupied by all particles. The behavior of monosized binary and polydispersed assembly with a similar initial PF is compared in Figure 2–7(b).
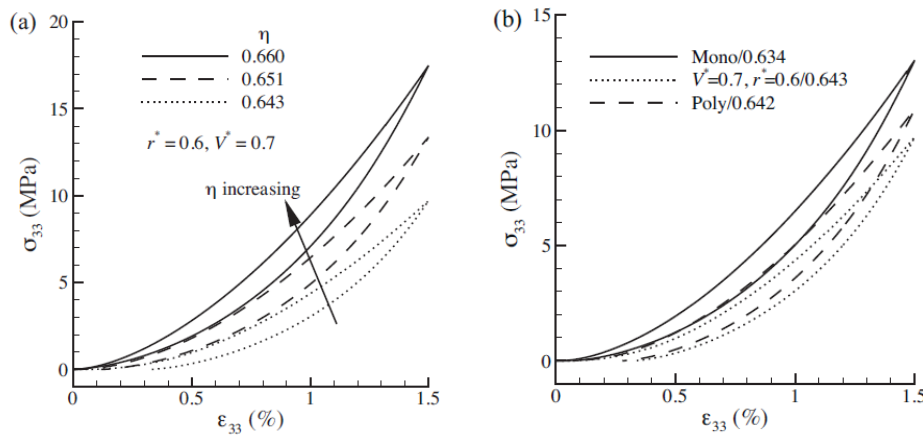
Figure 2–7: Average stress–strain response of: (a) binary pebble assemblies at different packing factors, (b) mono size, binary and polydisperse pebble assemblies with a similar packing factor. Packing factors are reported in the legend, [31] (Annabattula et al., 2012). Image reused with the permission of Elsevier.

Recently the KIT-DEM code was slightly modified by Pupeschi et al. [34] (2016) to estimate the mechanical behavior of ceramic breeder pebble beds under a cyclic mechanical loading. Figure 2–8(a) shows the influence of the cyclic loading on the residual strain foundin [34] (Pupeschi et al., 2016) after the 1st and 30th cycle for the material 20 LMT (Li$_4$SiO$_4$ + 20 mol% Li$_2$TiO$_3$), while in Figure 2–8(b) the variation of the residual strain after two consecutive cycles as a function of the cycle number is reported. In the legend of the graphs, LMT means lithium metatitanate, 20 indicates the mol% of Li$_2$TiO$_3$, 30 distingues the cases investigated up to 30 cycles while 2, 4 and 6 is the maximum applied load in MPa. Numerical results show a progressive compaction of the bed due to the cyclic loading. It was found that the largest part of the irreversible strain is determined by the first 10–15 cycles, and then a progressive smaller increment of the compaction occurs.

Recently, the influence of a considerable number of cycles on the behavior of packed assemblies was investigated [96][98] (Wang et al., 2015; Zhang et al., 2017a-2017b). Results show a progressive compaction of the bed with the cycling loading, resulting in an increase of

the effective bed stiffness. In [96] (Wang et al., 2015) the compaction was found to obey a stretched exponential evolution law. This means that the large compaction of the bed initially observed then decreases with the cycle number. As a consequence of the induced irreversible deformation of the bed, the packing fraction rapidly increases during the first cycles to then level off obeying to the same evolution law. In [97] (Zhang et al., 2017a) UCT experiments were conducted along with DEM numerical simulations to investigate the macro and micromechanical response of breeder beds subjected to cyclic loading. The distribution of the internal forces shows no influence of the mechanical cycling, while the coordination number clearly shows a major rearrangement of the particles during the first cycles.
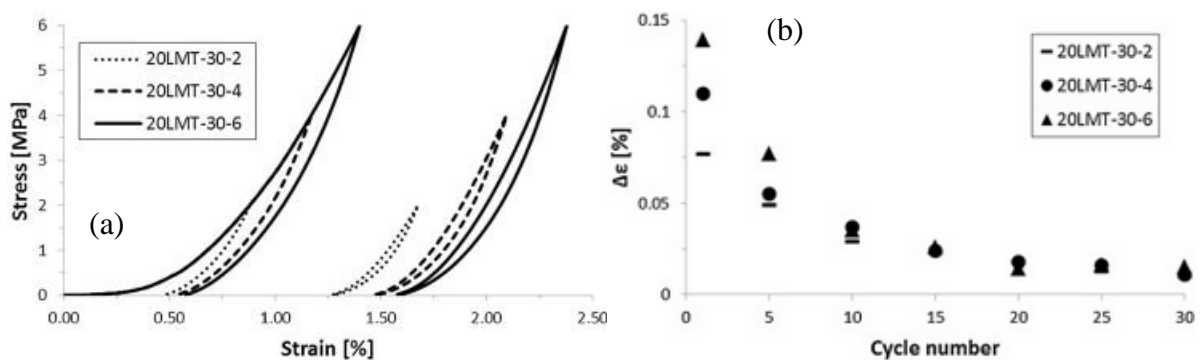
Figure 2–8: (a) Stress-strain curves for the 1st and the 30th loading/unloading cycles with different maximum compressive load, after [34] (Pupeschi et al., 2016). (b) Variation of the residual strain after two consecutive cycles as a function of the cycle number, after [34] (Pupeschi et al., 2016). Both images reused with the permission of Elsevier.

2.2.2 Effective thermal conductivity of ceramic breeder pebble beds

In order to study the thermal behavior of the breeder zone of a solid breeder blanket, the heat transfer inside pebble beds has to be investigated. To this end, the characterization of the effective thermal conductivity of the pebble beds is strongly required as this is an important parameter for the thermal design of the breeder zone. Due to discrete nature of a packed bed, its thermal conductivity is affected by the thermal properties of both the solid and the gas phase. In literature, experimental and numerical investigations on the effective thermal conductivity of pebble beds are reported [99] (Abou-Sena et al., 2005). In the following, a review of the main works characterizing the effective thermal conductivity of certain ceramic breeder pebble bed materials is presented, organized in separate passages for different breeder materials.

Lithium-orthosilicate, Li_4SiO_4

In 1990, Dalle Donne and Sordon [100] measured the effective conductivity of Li_4SiO_4 pebbles bed in stagnant helium at 1 bar. A temperature range of 50-350°C was considered and

monosized pebbles of 0.5 mm packed at ~60% were investigated. Results are reported in Figure 2–9(a). The effective thermal conductivity increases with the temperature about from 0.7 to 0.9 [W/mK]. In 1994, the study was further extended for polydispersed Li_4SiO_4 pebbles with a diameter range of 0.35-0.6 mm [101] (Dalle Donne et al., 1994). In the experiments, a packing factor of 64.4% was reached and the temperature range of 40-720°C was investigated. The experimental results were correlated by means of the equation

$$k = 0.708 + 4.51 * 10^{-4}T + 5.66 * 10^{-7}T^2,$$ 2.3

where k is in [W/(m K)] and T is in [°C]. The results are reported in Figure 2–9(a) and compared to results obtained in [100] (Dalle Donne and Sordon, 1990). The increase of the effective thermal conductivity with temperature was confirmed. Then, in 2000 Dalle Donne et al. [102] performed experiments using a pebble size range of 0.25-0.63mm with a packing factor of ~65%. The effective thermal conductivity was correlated to the bed temperature by

$$k = 0.768 + 0.496 * 10^{-3}T,$$ 2.4

where k is in [W/(m K)] and T is in [°C]. The results are presented in Figure 2–9(a) by a solid line. The effective thermal conductivity increases with temperature, as well, however the slope of the fitting line is lower compared to the dashed line fitting the experimental results obtained in [101] (Dalle Donne et al., 1994). During the experimental campaign carried out in [102] (Dalle Donne et al., 2000), the influence of the helium pressure (1 to 3bar) used as filling gas was studied. The results are plotted in Figure 2–9(b). The experiments showed that for the investigated pressures, the effective thermal conductivity doesn't change. In 2001, Enoeda et al. [103] measured the effective conductivity of Li_2TiO_3, Li_4SiO_4, Li_2ZrO_3 and Li_2O pebble beds varying the gas pressure from 0.001 to 0.2 MPa at about 520 °C. Furthermore, the temperature dependence was measured in the range of 425-775 °C for Helium at 0.1 MPa. Regarding Li_4SiO_4, pebbles with a size range of 0.25-0.63 mm were packed at ~61%. The experimental results for the thermal conductivity of Li_4SiO_4 pebble beds as a function of temperature and gas pressure are reported in Figure 2–9(a) and Figure 2–9(b), respectively. While a negligible dependence on temperature was observed, a strong influence of the gas pressure was found.

In Figure 2–9(b) the experimental results and the analytical values determined in [103] (Enoeda et al., 2001) from the correlations derived by Bauer and Schlunder (SBZ) [104] (Bauer and Schlunder, 1978) and Hall and Martin (HM) [105] (Hall and Martin, 1981), respectively, are compared. These correlations are both based on a mathematical model that

describes heat transfer in a basic cell. A strong dependence on the gas pressure was found. The thermal conductivity decreases with the gas pressure depicting the typical S-shape, which is representative of the Smoluchowski effect.
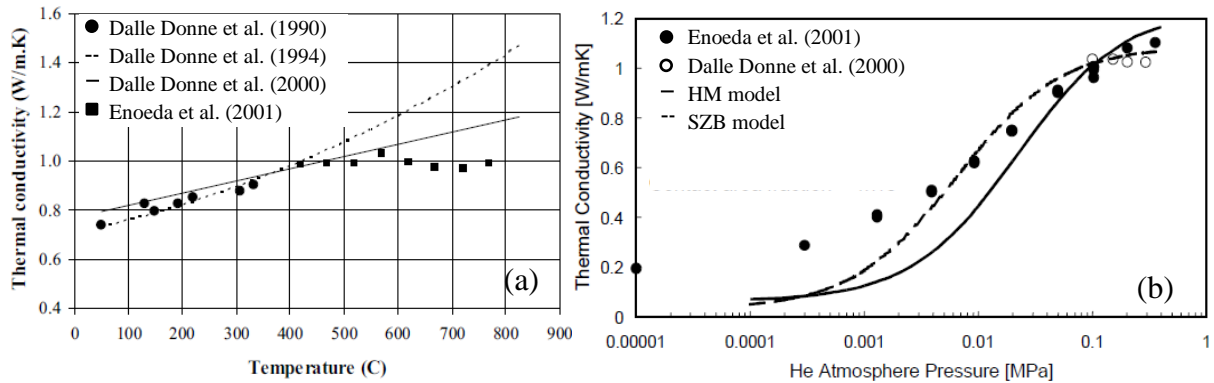

Figure 2–9: (a) Effective thermal conductivities of Li_4SiO_4 reported in literature, (b)Smoluchowski effect obtained analytically and with experiments. After [99] (Abou-Sena et al. 2005) and [103] (Enoeda et al., 2001), respectively. Both images reused with the permission of Taylor & Francis.

In 2002, Reimann and Hermsmeyer [106] measured the effective thermal conductivity of compressed ceramic breeder pebble beds investigating the influence of the interstitial filling gas. Pebbles of Li_4SiO_4 produced at KIT with a size range of 0.25-0.65 mm and packed at 64% were studied in helium and air for a maximum bed deformation of 4.5% and temperatures up to 800°C. Figure 2–10 shows the influence of the bed strain on the measured effective thermal conductivity for different combination of solid material, gas type and average bed temperature. In this study, the increase of the effective thermal conductivity with temperature was confirmed. A strong influence of the gas type was observed. Changing the filling gas from helium to air, a reduction greater than 50 % was detected. A slight increase of the effective thermal conductivity with the strain was observed.
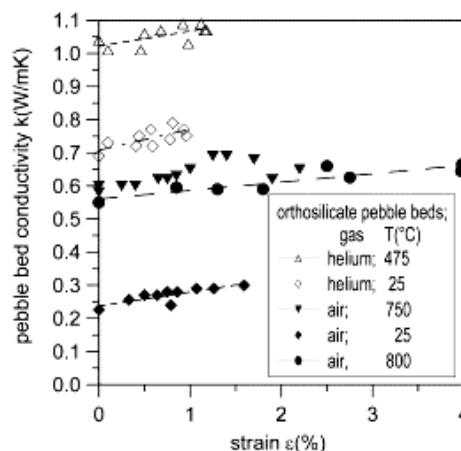

Figure 2–10: Thermal conductivity of Li_4SiO_4 in helium and air at different temperatures as a function of the bed strain evaluated with UTC experiments, [106] (Reimann and Hermsmeyer, 2002). Image reused with the permission of Elsevier.

The results obtained in helium atmosphere at elevated temperatures confirmed the correlation of Dalle Donne et al. [102]. The correlation reads as

$$k = 0.768 + 0.496 * 10^{-3}T + 0.045 \, \varepsilon, \qquad\qquad 2.5$$

where k is in [W/(m K)], T is in [°C] and ε is the uniaxial strain in [%]. Eq. 2.5 reduces for uncompressed beds to Eq. 2.4.

In 2015, Feng et al. [107] investigated the effective thermal conductivity of monosized pebbles of 1.0 mm with a packing factor of about 63%. During this experimental campaign, the thermal conductivity, thermal diffusivity α_d and specific heat capacity c_p were determined in the temperature range of RT-600°C. It was found that the thermal diffusivity decreases when the temperature increases while the other two properties increase with temperature. The following correlations as a function of temperature were found for the effective conductivity, thermal diffusivity and specific heat capacity, respectively:

$$k = 0.97198 + 5.04496 * 10^{-4}T + 3.30432 * 10^{-7}T^2, \qquad\qquad 2.6$$

$$\alpha_d = 0.5476 - 4.08679 * 10^{-4}T + 1.95265 * 10^{-7}T^2, \qquad\qquad 2.7$$

$$c_p = 1.57753 + 0.00179 \, T + 2.22244 * 10^{-6}T^2 \quad . \qquad\qquad 2.8$$

Recently, Pupeschi et al. [108] (2017) investigated the effective thermal conductivity of the EU Reference (EU Ref.) and advanced lithium orthosilicate materials. The current European reference breeding material consists of two phases, namely about 90 mol% lithium orthosilicate (Li_4SiO_4) and 10 mol% lithium metasilicate (Li_2SiO_3). Due to the fabrication process (melt-spraying method developed by Pannhorst et al. in 1998 [109]), pores are generated inside the pebbles influencing the rupture strength. To improve the mechanical performances, by reducing the process related defects, a new experimental facility was developed at KIT to produce Advanced Ceramic Breeder (ACB) pebbles by a melt-based method [110] (Kolb et al., 2011). To further enhance the mechanical properties, lithium metatitanate (Li_2TiO_3) was introduced as a second phase. In this study, three types of advanced compositions were investigated: 20LMT (20 mol% Li_2TiO_3), 25LMT (25 mol% Li_2TiO_3) and 30LMT (30 mol% Li_2TiO_3). The experiments were carried out in a temperature range of RT–700 °C. Both helium and air were used as filling gas at a pressure range of 0.12–0.4 MPa. In addition, the bed was compressed up to 6 MPa to study the influence of the compressive load on the bed's effective thermal conductivity. Figure 2–11 shows the results obtained in [108] (Pupeschi et al., 2017). These results confirmed the severe reduction of the

effective thermal conductivity when changing the filling gas from helium to air as observed in [103] (Enoeda et al., 2001). In both atmospheres, the effective thermal conductivity was found to increase with the temperature, while no significant effect of the compressive load was found. The chemical composition of the solid materials slightly influenced the effective thermal conductivity, while a clear dependence on the gas pressure was observed in helium atmosphere.
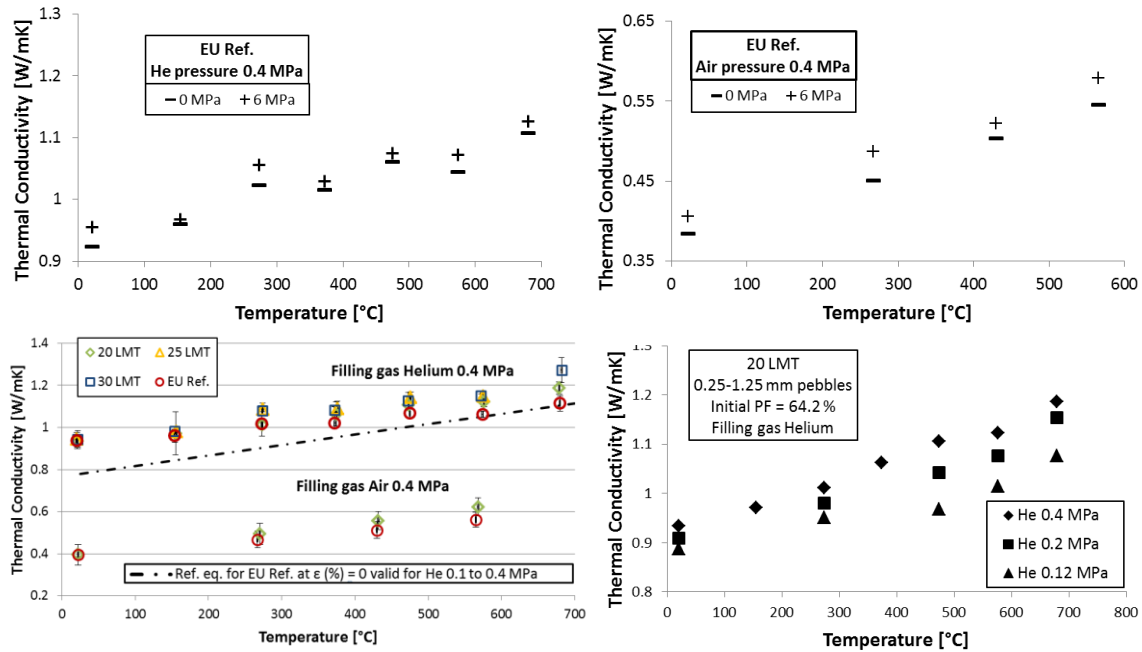

Figure 2–11: Thermal conductivities of EU Ref. material pebble beds in helium and air obtained from experiments carried out in [108] (Pupeschi et al., 2017). Images reused with the permission of Elsevier.

Lithium-metazirconate, Li₂ZrO₃

In 1991, Sullivan et al. [111] measured the effective thermal conductivity of Li_2ZrO_3 pebble bed in helium at 0.1 MPa in the temperature range of 70-500°C. Monosized pebbles with a diameter of 1.2 mm and a packing factor of 60% were investigated. Results of this work are shown in Figure 2–12. An increase of the effective thermal conductivity with temperature was observed.

In 1995, Lorenzetto [112] determined the effective thermal conductivity of Li_2ZrO_3 pebble beds in helium at 0.1 MPa for monosized pebbles of 1.2 mm in diameter packed at 63%. In the investigated temperature range of 100-1175°C, the correlation

$$k = 0.66 + 1.17 * 10^{-7}T^{2.2}$$

2.9

was proposed to describe the effective conductivity as a function of the temperature [112] (Lorenzetto, 1995). Here k is in [W/(m K)] and T is in [°C]. In this experimental campaign,

the increase of the effective thermal conductivity with temperature was confirmed, see Figure 2–12.

In 1998, Earnshaw et al. [113] performed experiments with monosized particles of Li_2ZrO_3 with a diameter of 1.2 mm and a packing factor ranging from 63 to 65%. The effective thermal conductivity was evaluated in the temperature range of 75-1170°C. The effect of the helium pressure, used as filling gas, was determined in the pressure range 0.01-300 KPa. At 100KPa, the data were fitted with the relation

$$k = 0.69 + 2.2 * 10^{-10}T^3. \hspace{3cm} 2.10$$
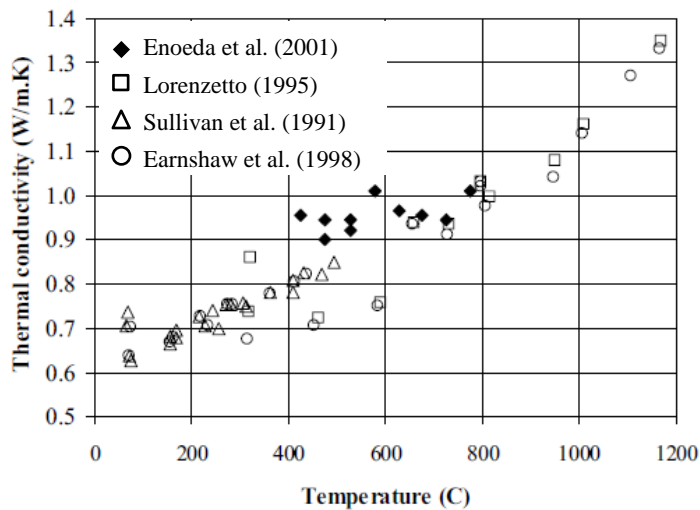
Figure 2–12: Effective thermal conductivity of Li_2ZrO_3 in helium reported in literature. After [99] (Abou-Sena et al., 2005). Image reused with the permission of Taylor & Francis.
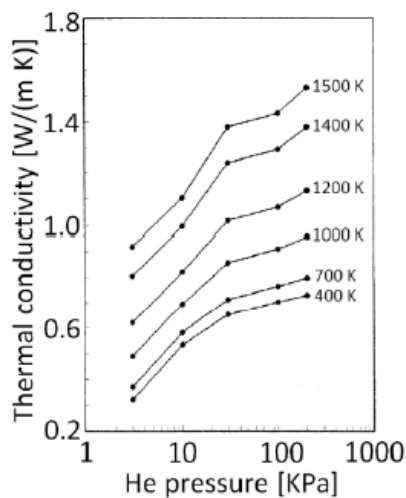
Figure 2–13: Effective thermal conductivity of Li_2ZrO_3 in helium as a fuction of the gas pressure at different bed's temperatures, [113] (Earnshaw et al., 1998). Image reused with the permission of Taylor & Francis.

The effective thermal conductivity of the bed was found to increase with both the temperature of the bed and the helium purge gas pressure. The variation of the effective thermal conductivity

with the temperature is reported in Figure 2–12 , while the dependence from the pressure is shown in Figure 2–13. The effective thermal conductivity of Li_2ZrO_3 in helium was investigated by Enoeda et al. in 2001 [103]. Measurements were carried out in the pressure range of 0.0001-0.1 MPa with polydispersed particles (diameter range of 0.8-1.2mm) packed at ~53.4% in the temperature range of 425-775°C. In Figure 2–12 the measured thermal conductivities are reported and compared to the previous studies described above. The studies show a consistial increase of the effective thermal conductivity with temperature and they are in good agreement with each other.

Lithium-methatitanate, Li_2TiO_3

The effective thermal conductivity of Li_2TiO_3 pebble beds in helium atmosphere was investigated by Enoeda et al. in 2001 [103]. Measurements were made with polydispersed pebble diameters of 0.8-1.2mm packed at ~59% in helium at 0.1 MPa. It was found that the effective thermal conductivity increases from about 1 to1.2 [W/mK]. Results of this study are compared with other studies in Figure 2–14.

In 2003, Hatano et al. [114] published their study on the effective thermal conductivity of Li_2TiO_3 pebble bed. In a temperature range of 420-775 °C measurements were performed for single and binary size beds in helium varying the gas pressure from vacuum to 0.2 MPa. A packing factor of 60 and 80 % was reached for monosized pebbles (diameter of 1.91 mm) and for binary size pebbles (0.28-1.91 mm), respectively. In Figure 2–14 the results of this study are reported and compared to the results obtained in [103] (Enoeda et al., 2001). While monosized pebbles at 60 % of PF show a poor dependence on temperature, the effective thermal conductivity of the assembly composed of binary size pebbles increases with temperature in agreement with results obtained in [103] (Enoeda et al., 2001).

In 2002, during the experimental campaign carried out to study the effective thermal conductivity of Li_4SiO_4 mentioned before, Reimann and Hermsmeyer [106] measured the effective thermal conductivity of compressed Li_2TiO_3 investigating, in addition, the influence of the interstitial gas. Different kinds of pebbles, provided from different associations with different characteristics, were investigated. They were designated as follow: Ti-D and Ti-E from CEA with a pebble diameter range of 0.8-1.2mm. Ti-J and Ti-J-bin from JAERI, monosized (2 mm) and binary (0.2 - 2 mm) pebbles, respectively. Ti-D and Ti-E were packed at 63% and 63.2%, respectively while Ti-J at 64.3% and Ti-J-bin at 81.2%. In Figure 2–15, the obtained results at different temperatures as a function of the bed strain are reported. As for the experiments with Li_4SiO_4, the effective thermal conductivity in helium was found to be much higher than in air or argon and it slightly increases with strain.
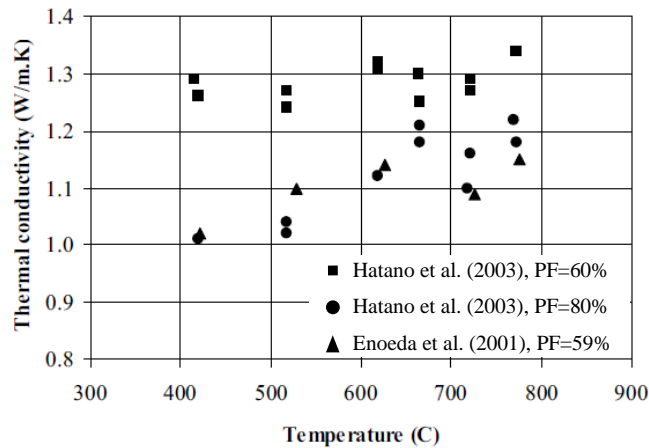
Figure 2–14: Effective thermal conductivities of Li$_2$TiO$_3$ in helium reported in literature. After [99] (Abou-Sena et al., 2005). Image reused with the permission of Taylor & Francis.

In 2007, Abou Sena et al. [115] measured the effective thermal conductivity of Li$_2$TiO$_3$ pebble beds as a function of the bed temperature in the temperature range 50-500 °C. Pebbles with diameters of 1.7-2 mm were packed at 61% with helium as interstitial gas at atmospheric pressure. A decrease of the effective thermal conductivity with increasing temperature from 1.4 (at 500°C) to 0.94 (at 50°C) W/mK was reported.
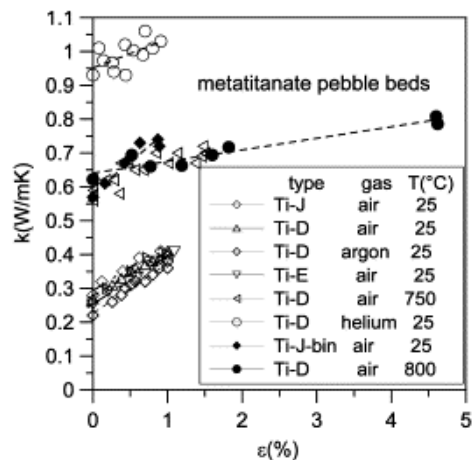
Figure 2–15: Effective thermal conductivities of different Li$_2$TiO$_3$ pebbles evaluated in helium, air and argon at different temperatures and strain levels,) [106] (Reimann and Hermsmeyer, 2002. Image reused with the permission of Elsevier.

In 2016, Panchal et al. [116] investigated the effective thermal conductivity of Li$_2$TiO$_3$ pebble beds in stagnant helium by means of the Finite Element Analysis (FEA) code COMSOL [117]. Different uniform packing structures (simple cubic, body centered cubic and face centered cubic arrangement) and random close packing (RCP) structures were considered. The random packing structure was generated with a DEM code. The heat transfer through pebble beds was simulated through both solid and fluid conduction while thermal radiation was ignored. The comparison among results obtained with this FEM code, available

experimental data and values obtained with the numerical correlation of Zehner-Schlunder is reported in Figure 2–16. The results predicted an increment of the effective thermal conductivity with both temperature and packing factor. For randomly close packed Li_2TiO_3 pebble beds the numerical results were found to be in agreement with the available experimental data and the numerical correlation of Zehner-Schlunder.
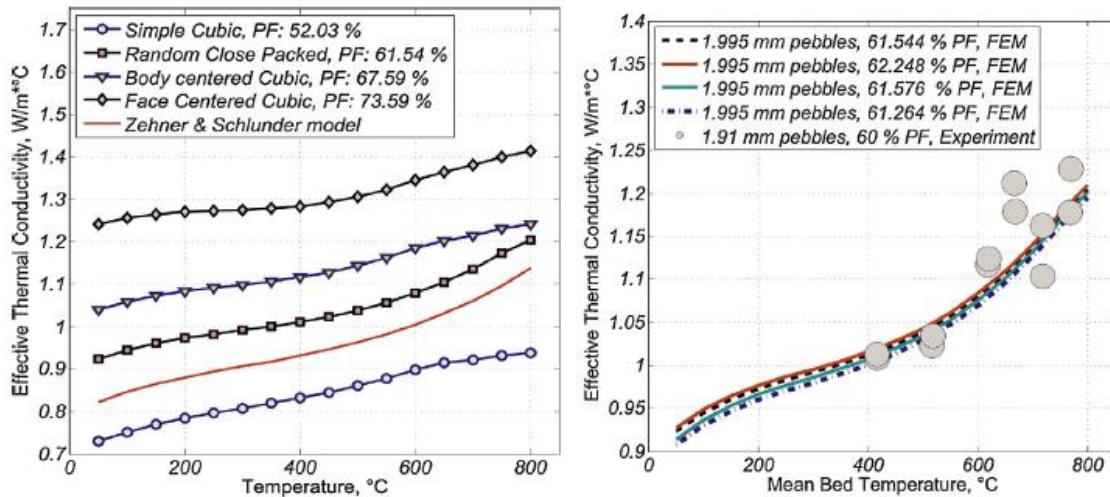

Figure 2–16: Effective thermal conductivities of Li_2TiO_3 in stagnant helium evaluated with COMSOL and compared with existing experimental data and analytical values, [116] (Panchal et al., 2016). Image reused with the permission of Elsevier.

Lithium-oxide, Li_2O

In 1994, Enoeda et al. [117] presented their results on the effective thermal conductivity of Li_2O pebble beds. The effective thermal conductivity was measured in the temperature range 150-650 °C. Monosized pebbles of 1 mm packed at 48% in helium at 1 atm were investigated. The effective thermal conductivity showed poor temperature dependence and it slightly decreases with the increase of temperature. The results of this study are reported and compared to the studies developed in [103] (Enoeda et al., 2001) for pebble beds of Li_2O in Figure 2–17.

In [103] (Enoeda et al., 2001), polydispersed pebble beds of Li_2O with a size ranging from 0.85 to 1.18 mm were packed at 62.1%. The investigated temperature range was 425-775 °C, while the interstitial filling gas was helium at 0.1MPa. In this experimental campaign the effective thermal conductivity show poor temperature dependence and some values tend to decrease.

The experimental, numerical as well as analytical results show that the effective thermal conductivity of a packed bed is mainly influenced by the properties of the solid material and filling gas in addition to the PF, particle size, temperature, gas pressure and compression state. Aside from few cases [103] (Enoeda et al., 2001), [114] (Hatano et al., 2003) and [117]

(Enoeda et al., 1994), the effective thermal conductivity of the bed was found to increase with the temperature. Among the ceramic Li-compounds candidated as breeder material, the Li_2O has the highest thermal conductivity. Therefore, pebble beds of Li_2O showed the highest thermal conductivity [99] (Abou-Sena et al., 2005) compared to the other beds. Results showed a strong influence of the of the filling gas pressure on the effective thermal conductivity of the bed [103] (Enoeda et al., 2001), [113] (Earnshaw et al., 1998). In the pressure range of 0.0001-0.1 MPa the effective thermal conductivity was found reducing with the pressure. For values above 0.1 MPa, the pressure dependence was found to be negligible [102] (Enoeda et al., 1994), [103] (Enoeda et al., 2001). A moderate increase of the thermal conductivity with the increase of the strain of the pebble bed was detected in the experimental campaigns [106] (Reimann and Hermsmeyer, 2002),[108] (Pupeschi et al., 2017).
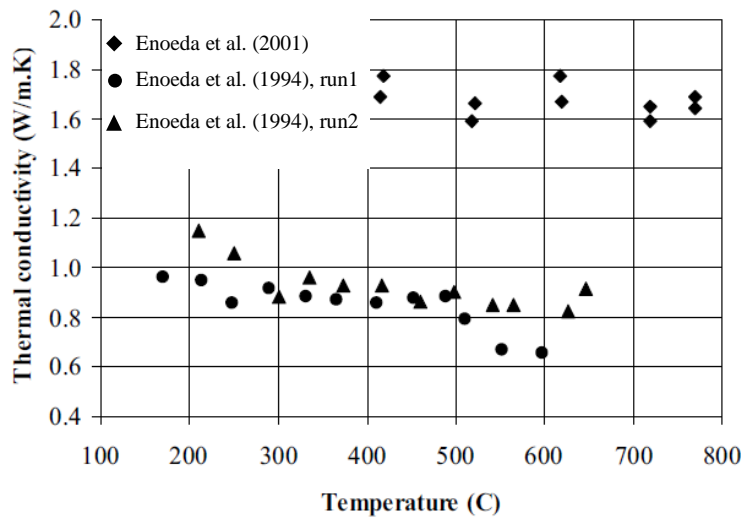

Figure 2–17: Comparison among experimental results of effective thermal conductivity of Li_2O in helium. After [99] (Abou-Sena et al., 2005). Image reused with the permission of Taylor & Francis.

Chapter 3

DEM for ellipsoidal packed particles

The currently produced ceramic breeder pebbles are characterized by a spheroidal shape. The existing small deviation from a perfect sphericity can affect the overall mechanical behavior of the pebble bed. In this chapter the influence of the particles' shape on the mechanical behavior of the bed is investigated by means of a dedicated extension of the existing in-house KIT-DEM code (see also Moscardini et al., 2017 [119]). First, the applied method to represent the currently produced pebbles as ellipsoidal particles is reported in detail. Then, the implemented algorithms to generate highly packed assemblies and to study the mechanical behavior under uniaxial compression are described, respectively. The particle's orientation and the relation between macro and micro mechanics are discussed. Finally, sensitivity studies carried out by varying key parameters governing the mechanical behavior are reported.

3.1 Generation of assemblies of ellipsoidal particles

In this section the implementation of the Multi-Sphere (MS) method to represent the individual ellipsoidal particle is presented, first. Then, the modifications to the random close packing algorithm for ideal spheres to generate highly packed assemblies of ellipsoidal particles are described in detail.

3.1.1 Multi-Sphere approach to generate ellipsoidal particles

Among the available methods reviewed in the Chapter 2 to represent ellipsoidal particles, the MS method was selected. In the MS approach, several primary spheres are clustered to reproduce the desired particle geometry. The main advantage of the MS method is that the robust contact algorithm developed for spherical particles is still applicable between the primary spheres composing two contacting non-spherical particles. By tailoring the size and number of the primary spheres and adjusting their relative position (allowing overlaps among them), the desired shape is obtained.

The studies reported in this thesis were performed on assemblies consisting of mono-sized ellipsoidal particles. The number of the particles N_p [/] to be packed inside the assembly, their aspect ratio a_r [/], the number of primary spheres N_s [/] composing the individual ellipsoidal particles and their radius are set as input parameters. The major axis of the ellipsoidal particle is fixed as a function of the aspect ratio, which is here defined as the ratio between the major

axis and the diameter of the central primary sphere. Each ellipsoidal particle is composed aligning the centers of the primary spheres. An odd number of primary spheres was used to generate the individual ellipsoidal particle matching its center of mass with that one of the central sphere. This simplifies the implementation of the equations of motion. Furthermore, if the primary spheres have different radii, the sphere with the maximum radius R_{max} [m] is located in the middle of the major axis of the ellipsoid while the other spheres are aligned, in a symmetric way, outwards with decreasing radius. The overlap between the primary spheres δ_s [m] is related to the aspect ratio as well as to the number of the clustered primary spheres (N_s) and to their radius. In particular, $\delta_s = \delta\, R_{sm}$ [m] is calculated from the fraction δ [/] of the smaller radius R_{sm} [m] of any two consecutive primary spheres in overlap. The value of the fraction δ is determined in this work by

$$\delta = \frac{\left(2\sum_{i=1}^{N_s} R_i\right) - \left(2\,R_{max}a_r\right)}{\left(\sum_{i=1}^{N_s} R_i\right) - R_{max}}. \qquad 3.1$$

Here, R_i [m] is the radius of the i-th primary sphere composing the individual ellipsoidal particle. From Eq. 3.1, δ is a constant for an ellipsoidal particle and it is determined by means of a pure geometrical calculation, and, thus δ_s changes as a function of R_{sm} along the chain of primary spheres. Now, once the primary spheres are located inside the ellipsoidal particle, their relative position must not change to maintain the geometry. Figure 3–1 shows a scheme of an ellipsoidal particle composed of 5 primary spheres with different radius.
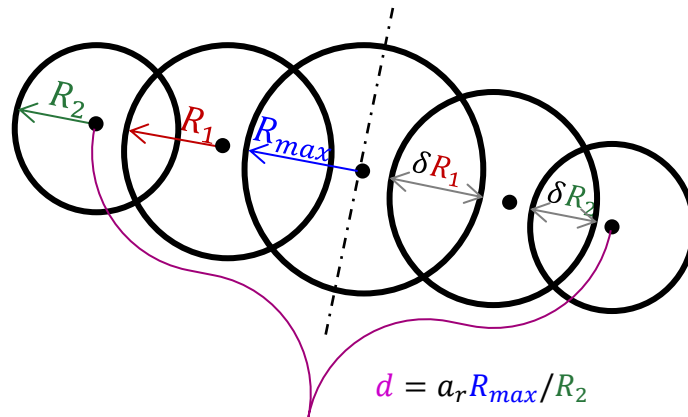

Figure 3–1: Simplified scheme of an ellipsoidal particle composed of 5 primary spheres with different radius

To explain the procedure to generate the required number of ellipsoidal particles inside a virtual box, the basic example of ellipsoidal particles composed of three monosized spheres is considered hereafter. Initially all primary spheres ($N_p * N_s$) required to create the ellipsoidal particles are randomly generated in a cubic box with an edge length L [m]. In Figure 3–2(a)

the virtual cubic box with the centers of the primary spheres is exemplarily shown. Therefore, to create, say, an assembly with N ellipsoidal particles, 3N primary spheres are randomly generated inside the virtual box. Each ellipsoidal particle and each sphere is numbered sequentially. According to the assigned number, the spheres are then classified in three groups, namely spheres "a" (from 1 to N), spheres "b" (from N+1 to 2N) and spheres "c" (from 2N+1 to 3N). Each ellipsoidal particle is formed by aligning three spheres belonging to the groups "a", "b", and "c" with a fixed distance and overlap depending on the desired aspect ratio. The spheres "a" and "b" become the external primary spheres of the ellipsoidal particle while the sphere "c" is placed in the middle of the line joining centers of "a" and "b" to form the ellipsoidal particle. In Figure 3–2(b), the composed ellipsoidal particle is shown. In particular, the ellipsoidal particle number 1 is created moving sphere "b" N+1 in the direction of sphere "a" 1. Thereafter, sphere "c" 2N+1 is moved in the middle (Figure 3–2(a)).With the same method, the other ellipsoidal particles are generated (e.g., the ellipsoidal particle number *i* is composed of the spheres *i*, N+*i* and 2N+*i* belonging to the groups "a", "b" and "c", respectively).
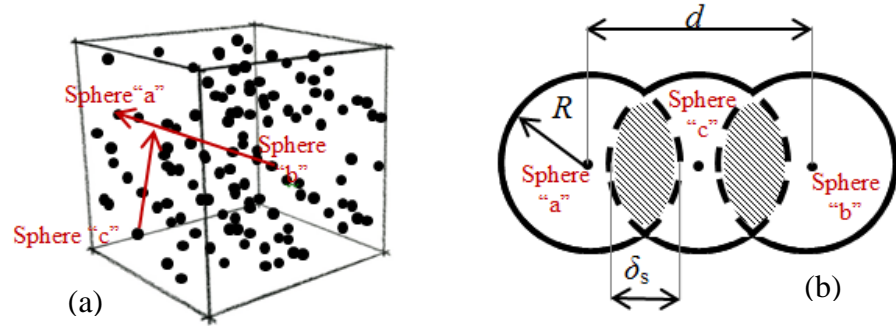

Figure 3–2: (a) Centers of the spheres in the virtual cubic box; (b) Composed ellipsoidal particle, [119] (Moscardini et al., 2017).

The coordinates of the motion of a sphere "b" along the line shown in Figure 3–2-(a) are given by

$$
\begin{cases}
x(t_f) = x_a + t_f(x_b - x_a) \\
y(t_f) = y_a + t_f(y_b - y_a), \\
z(t_f) = z_a + t_f(z_b - z_a)
\end{cases}
\qquad 3.2
$$

where subscript a indicates the position of sphere "a", while subscript b indicates the initial position of sphere "b". The value t_f [/] for the final position *(x(t_f)* [m], *y(t_f)* [m], *z(t_f)* [m]) of sphere "b" is chosen such that a given aspect ratio a_r is obtained. For the composite particle in Figure 3–2(b), the aspect ratio is given by:

$$
a_r = \frac{d + 2R}{2R},
\qquad 3.3
$$

where R [m] is the radius of a primary sphere and

$$d \text{ [m]} = \sqrt{(x(t_f) - x_a)^2 + (y(t_f) - y_a)^2 + (z(t_f) - z_a)^2} \; , \qquad 3.4$$

is the distance between the two external spheres in the final configuration. Plugging $x(t_f)$, $y(t_f)$, $z(t_f)$ into Eq. 3.4 the value of t_f is obtained as

$$t_f = \frac{d}{\sqrt{(x_b - x_a)^2 + (y_b - y_a)^2 + (z_b - z_a)^2}}, \qquad 3.5$$

where d is defined as a function of the aspect ratio from the Eq. 3.3. The final position of the center of sphere b is obtained from inserting the solution t_f into Eq. 3.2. If more than 3 primary spheres with the same or different radius have to be aligned, the explained procedure does not change and the additional spheres are added as a function of the overlap δ_s.

When all particles are formed, two different kinds of overlaps exist. The first one is between the primary spheres composing the same ellipsoidal particle δ_s, while the second one δ_p [m] occurs between the spheres of two different ellipsoidal particles in contact. This is an artifact due to placing primary spheres randomly and forming composite particles from them. The next subsection deals with the procedure to remove this second kind of unphysical overlaps from the assembly.

3.1.2 Random Close Packing Algorithm for ellipsoidal particles obtained by the MS method

The Random Close Packing Algorithm (RCP), first proposed by Jodrey and Tory (1985) [95] and successively used by Gan and Kamlah (2010) [28] to generate random and densely packed assemblies of spherical particles, was adapted in order to be consistent with the MS method previously described. The modified RCP iteratively removes the overlap δ_p between the primary spheres belonging to two different ellipsoidal particles in contact. The primary spheres are characterized by an outer radius $RO_i = r_i * R_{out}$ [m] and an inner radius $RI_i = r_i * R_{in}$ [m], where r_i [/] $= R_i / R_{max}$ represents the ratio between the radius of the current primary sphere R_i to the radius of the central primary sphere R_{max}. For monosized primary spheres, r_i is always equal to 1. For both monosized and not-equal sized assemblies, R_{out} [m] and R_{in} [m] are two values valid for all primary spheres in the individual time step of the iteration, and, preserving the ratio r_i, R_{out} and R_{in} are defined as follows:

○ R_{out} is initially set in order to make an ideal starting packing factor $PF^{(0)} = 1$, which is evaluated as the ratio between the volume taken by the ellipsoidal particles and the volume of the virtual cubic box. Therefore, R_{out} characterizes overlaps between particles.

- o R_{in} is defined as the half of the distance between the centers of the two closest primary spheres of two different ellipsoidal particles. It is the value for which no overlaps among ellipsoidal particles occur in the whole assembly.

In Figure 3–3(a), a schematic view of two ellipsoidal particles in overlap is shown, while in Figure 3–3(b) R_{out} is shown together with R_{in} for the two closest primary spheres in contact in an individual iteration step.
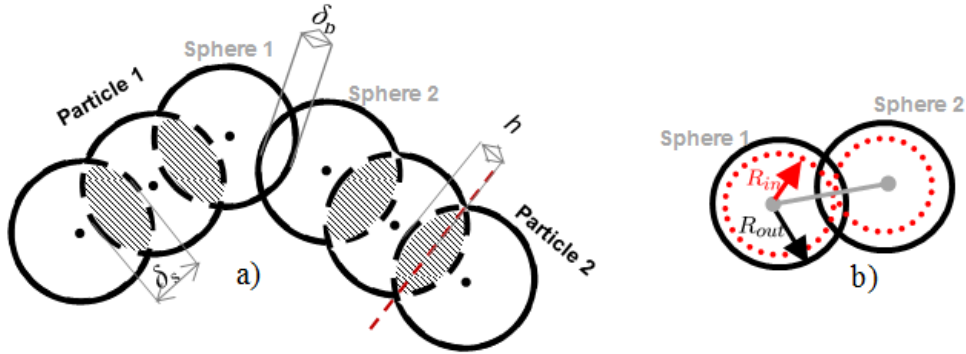

Figure 3–3: a) Ellipsoidal particles in overlap; b) Outer and inner radius of monosized spheres, [119] (Moscardini et al., 2017).

R_{out} and R_{in} are adjusted to approach each other step by step by removing the worst overlap of the current iteration. When $(R_{out} - R_{in})/ R_{out}$ falls below a certain threshold, the assembly is considered to be free of overlaps and the start configuration for the subsequent mechanical simulation is reached.

The initial configuration to begin the RCP procedure is defined as follows. First, the spherical particles are generated randomly into the virtual cubic box as described in the previous subsection. Afterwards, the initial value of R_{out} is set to get an ideal starting packing factor $PF^{(0)}$ [/] equal to 1 and preserving the ratio between radius of primary spheres. $PF^{(0)}$ is given by

$$PF^{(0)} = \frac{V_p N_p}{V} = 1 \,,$$

3.6

where V_p [m^3] and N_p are the volume and the number of the composed ellipsoidal particle contained in the volume V [m^3] of the virtual box, respectively. The volume of the composed ellipsoidal particle is calculated as difference between the total volume of the primary spheres and the total volume of the spherical caps in overlap as

$$V_p = \left(\sum_{i=1}^{N_s} V_{s,i} \right) - \left(\sum_{i=1}^{N_s-1} V_{sc,i} + V_{sc,i+1} \right),$$

3.7

where N_s, $V_{s,i}$ and ($V_{sc,i} + V_{sc,i+1}$) [m³] are the number of the primary spheres clustered to form the individual ellipsoidal particle, the volume of the i-th primary sphere and the total volume of the spherical cap defined from the sphere i and $i+1$, respectively. $V_{sc,i} + V_{sc,i+1}$ and $V_{s,i}$ are given by

$$V_{sc,i} + V_{sc,i+1} = \pi\, h_i^2 \left(R_{out}\, r_i - \frac{h_i}{3} \right) + \pi\, h_{i+1}^2 \left(R_{out}\, r_{i+1} - \frac{h_{i+1}}{3} \right) \qquad 3.8$$

$$V_{s,i} = \frac{4}{3}\pi\, (R_{out}\, r_i)^3, \qquad 3.9$$

As shown in Figure 3–4, h_i and h_{i+1}[m] are the heights of the two spherical caps of two consecutive primary spheres in overlap of the same ellipsoidal particle and evaluated as

$$h_i = X\, R_{out}\, r_i \delta\,;\quad h_{i+1} = (1 - X)\, R_{out}\, r_i \delta \qquad 3.10$$

where

$$X[/] = \frac{2\, r_{i+1} - r_i \delta}{2\, r_{i+1} + 2\, r_i - 2\, r_i \delta} \qquad 3.11$$

is the fraction of the distance in overlap defining the height of the spherical cap of the smallest particle between two consecutive spheres. Plugging h_i and h_{i+1} into Eq. 3.8 and then $V_{sc,i} + V_{sc,i+1}$ into the Eq. 3.7 the volume of the ellipsoidal particle is defined as a function of R_{out}. Substituting V_p into the Eq. 3.6, R_{out} is defined as a function of PF[(0)]. Finally, the primary spheres in the ellipsoidal particles are scaled considering R_{out} as starting radius. Now the initial configuration is ready and the iteration process to remove overlaps starts.
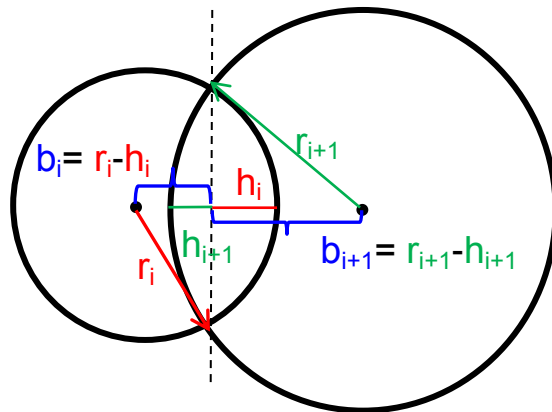

Figure 3–4: Geometric scheme for the evaluation of the volume of the spherical caps of two consecutive primary spheres in overlap belonging to the same ellipsoidal particle.

The initial value of R_{out} defines the largest overlap between any two particles in the assembly. During each of the following iteration steps, the code detects the overlaps between

primary spheres of contacting particles and creates a list starting from the largest overlap. The inner radius is then calculated as function of the worst overlap as defined above. The primary spheres in contact are moved away from each other equally by a distance of R_{out}-R_{in} along the line that connects the two centers. Then the other primary spheres composing the ellipsoidal particles in contact are accordingly moved to maintain the particle's shape and spatial orientation. Afterwards, as described in [27] (Gan, 2008) the outer radius is contracted according to

$$\mathcal{X}_c^{i+1}[/] = \mathcal{X}_c^i \frac{(1/2)^j \, C_r}{N_p}, \qquad\qquad 3.12$$

where $\mathcal{X}_c^i[/] = R_{out}^{(i)}/R_{out}^{(0)}$ and j $[/] = \left[-\log_{10} \Delta\eta^{(i)}\right]$. Here, i is the iteration number, and $\Delta\eta$ [/] is the difference between the packing factors calculated by the scaling radii R_{out} and R_{in}. More details are reported in [27] (Gan, 2008) for random packing of spherical particles. The parameter C_r [/] is the contraction rate, and it is the input parameter that controls how much the outer radius is contracted in each iteration step. As reported in [27] (Gan, 2008), for assemblies of packed spheres, the resulting packing factor can be roughly controlled by C_r. In order to check this property for ellipsoidal particles, three assemblies of 5000 monosized ellipsoidal particles were generated for each value of C_r. Each ellipsoidal particle has an aspect ratio of ~1.12 (rounded to the second digit) and it is composed of 3 monosized primary spheres. In Figure 3–5 the obtained packing factors for the selected values of C_r are reported.
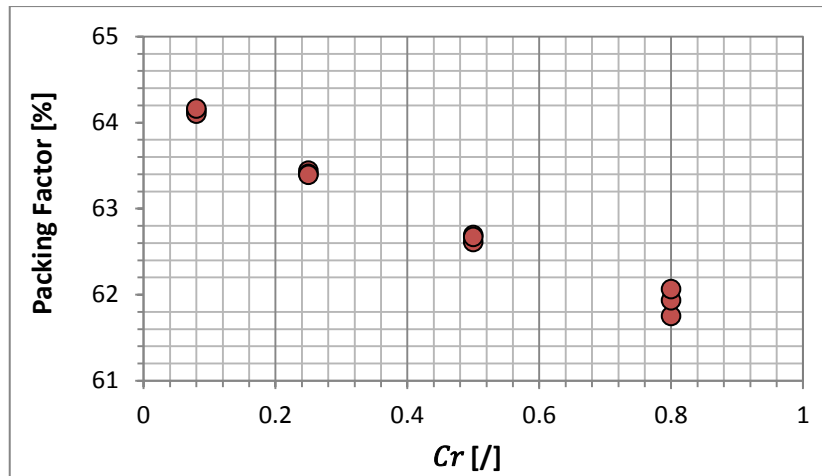

Figure 3–5: Packing factor obtained from selected values of contraction rate C_r for assemblies of 5000 ellipsoidal particles with an aspect ratio of ~1.12, [119] (Moscardini et al., 2017).

First, we observe that for the same value of the contraction rate nearly the same packing factor is obtained for different assemblies. Second, the trend of an increase of the packing factor with decreasing contraction rate can clearly be recognized. This together confirms that also for ellipsoidal particles the packing factor of an assembly can roughly be controlled by

the contraction rate. Figure 3–6 exemplarily shows one of the generated assemblies of ellipsoidal particles having an aspect ratio of ~1.12 and an overlap between the primary spheres of ~1.88*R*. The assemblies are visualized with a dedicated script in Mathematica 10.3 [120] (http://www.wolfram.com/). Figure 3–7 shows the intersections between the directions representing the particles' orientation and a sphere with a unit radius. Each direction is oriented in space by means of the direction cosine and determines two intersection points with the sphere's surface. The quasi-uniform distribution of the points on the spheres' surface indicates the randomness of the particles' orientation.
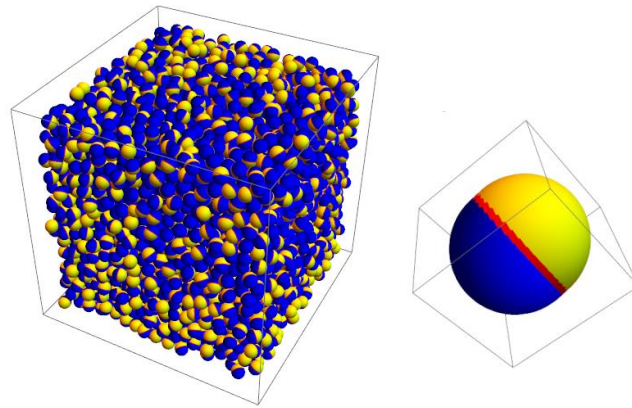
Figure 3–6: Assembly of 5000 mono-sized ellipsoidal particles composed of 3 equal-sized spheres in overlap, [119] (Moscardini et al., 2017).
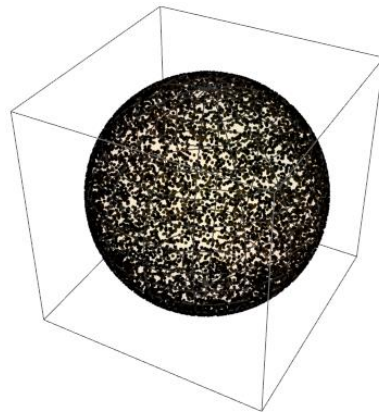

Figure 3–7: Projection of the particles' orientation on the surface of a sphere with a unitary radius

3.2 Discrete Element Method for ellipsoidal particles

In order to study the mechanical behavior of assemblies of ellipsoidal particles, uniaxial compression tests (UCT) are simulated by applying a prescribed deformation in a series of load steps separated by time increments Δt. After each change of the prescribed deformation, the equations of motion are solved until an equilibrium state is reached. Artificial damping [28] (Gan and Kamlah, 2010) is introduced to gradually remove all kinetic energy from the system to reach the quasi-static condition. During such a physical process of relaxation

towards equilibrium, the equations of motion are solved numerically by an explicit time stepping scheme.

As previously described, the ellipsoidal particles are generated by means of the MS method and the contact detection is carried out between the primary spheres composing different particles. Therefore, the contact detection algorithm developed for spherical particles in [28] (Gan and Kamlah, 2010), is still applicable. The deformation of the primary spheres is considered to be purely elastic with normal and tangential interactions. The normal force is evaluated by the Hertzian contact law [121] (Johnson, 1985)

$$f_{N,j}^{(I_n,Q_m)}[N] = -\frac{4}{3} E^* \sqrt{R^{rd}} (\delta_j)^{3/2} \, n_j \, . \tag{3.13}$$

Here, $f_{N,j}^{(I_n,Q_m)}$ is the normal force between the two primary spheres n and m constituting two different ellipsoidal particles I and Q defining the contact j. Furthermore, δ_j is the overlap in the contact j defined between the two primary spheres constituting the two different particles I and Q, while n_j is the outward normal at the primary spheres in contact j. Finally, since the particles in contact are made of the same material in our case, the effective Young's modulus E^* [Pa] is expressed as $E^* = E/2\,(1-\nu^2)$, while the reduced radius R^{rd}[m] is defined as $R^{rd} = R_{Q_m} R_{I_n}/(R_{Q_m} + R_{I_n})$. The tangential force acting between I_n and Q_m is taken as the minimum between the friction and the shear force according to [122] (Bicanic, 2004) as

$$f_{T,j}^{(I_n,Q_m)}[N] = -\frac{\Delta \dot{x}_{T,j}}{|\Delta \dot{x}_{T,j}|} \min \left(\mu \left| f_{N,j}^{(I_n,Q_m)} \right|; \, K_s \, r_c \, |\Delta \dot{x}_{T,j}| \, \Delta t \right), \tag{3.14}$$

where $\Delta \dot{x}_{T,j}$ [m/s] is the sliding velocity in the contact j that occurs between the two primary spheres constituting different particles, i.e. the difference in velocities of the surfaces of the corresponding primary spheres in this contact. The parameters μ [/] and K_s [Pa] are the friction coefficient of the contacting surface and the shear stiffness, respectively. Last, r_c is the radius of the contact area, which is expressed as r_c [m]$= \sqrt{\left(\frac{1}{R_{Q_m}} + \frac{1}{R_{I_n}} \right) \delta_p}$ [121] (Johnson, 1985). The contact forces acting on I_n are applied to Q_m with the same magnitude but opposite orientation to satisfy the principle of action and reaction.

As shown in Figure 3–8, due to the shape approximation introduced by the MS method, more than one contact can occur between two particles. This phenomenon is called multi

contact (MC). This means that the code can detect more than one contact acting on the particle I from the same primary sphere of the particle Q. The number of the multi contacts N_{IQ}^{MC} [/] between two particles I and Q depends on the number of the primary spheres, on the overlap between them and on the relative position of the two contacting particles. For example, for two particles in contact each being composed of three primary spheres, the maximum number of multiple contacts is 9. The possibility of multiple contacts is an intrinsic feature of the MS geometry, which does not happen between true ellipsoids due to their convexity. However, since we want to approximate real ellipsoids by MS particles, we need to deal with artifacts due to multiple contacts such as overestimation of the resulting stresses.
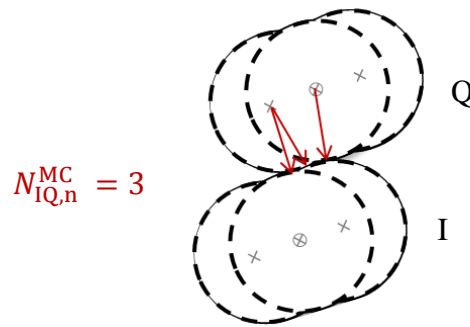

Figure 3–8: Multiple contacts between two particles I and Q at some time step n,) [119] (Moscardini et al., 2017.

To approach the ellipsoid situation by reducing the effect of the multiple contacts, it was suggested in [63] (Höhner, 2011) to divide the increment of both normal and tangential force at each time step n by the current number $N_{IQ,ni}^{MC}$ of multiple contacts between particles I and Q. Thus, the contact forces are updated based on the previous value of time step n-1. The normal force is updated according to

$$\hat{f}_{N,k_q,n}^{(I,Q)} = \hat{f}_{N,k_q,n-1}^{(I,Q)} + \frac{\Delta f_{N,k_q,n}^{(I,Q)}}{N_{IQ,n}^{MC}} \; ; \quad k_q = 1, \dots , N_{IQ,n}^{MC} \; , \qquad 3.15$$

where $\hat{f}_{N,k_q,n}^{(I,Q)}$ represents the adjusted magnitude of the normal force at time step n in a multiple contact k_q [/], which particle I has with particle Q. Furthermore, the increment $\Delta f_{N,k_q,n}^{(I,Q)}$ is the difference between $f_{N,k_q,n}^{(I,Q)}$ and $f_{N,k_q,n-1}^{(I,Q)}$, which are the corresponding magnitudes of Eq. 3.13 at time steps n and n-1, respectively.

The procedure to scale the tangential force on the multi contacts number requires a further observation. At each time step, the magnitude of the tangential force is defined as the minimum value between the friction force and the shear force, as reported in Eq. 3.14. At this point, the magnitude of the friction force, which depends on the normal force, is already

updated by means of Eq. 3.15. Therefore to avoid a further adjustment of the friction force during the same iteration, the code scales only the magnitude of the shear force according to

$$\hat{f}_{T_s,k_q,n}^{(I,Q)} = \hat{f}_{T_s,k_q,n-1}^{(I,Q)} + \frac{\Delta f_{T_s,k_q,n}^{(I,Q)}}{N_{IQ,n}^{MC}} \; ; \quad k_q = 1, \dots , N_{IQ,n}^{MC} \; . \tag{3.16}$$

In Eq. 3.16, $\hat{f}_{T_s,k_q,n}^{(I,Q)}$ represents the adjusted magnitude of the shear force at time step n in a multiple contact k_q, which particle I has with particle Q. $\Delta f_{T_s,k_q,n}^{(I,Q)}$ is the difference between $f_{T_s,k_q,n}^{(I,Q)}$ and $f_{T_s,k_q,n-1}^{(I,Q)}$, which are the magnitudes of the shear force $K_s \, r_c \, |\Delta \dot{x}_{T,j}| \, \Delta t$ at time steps n and n-1 respectively. Afterwards the minimum value between the friction and the shear force is evaluated. The adjusted magnitude of the normal force from Eq. 3.15 is then multiplied by the normal unit vector giving

$$\hat{\boldsymbol{f}}_{N,j}^{(I_n,Q_m)} = \hat{f}_{N,k_q,n}^{(I,Q)} \, \boldsymbol{n}_j \tag{3.17}$$

On the other hand, the adjusted magnitude of the tangential force, which is the minimum value between $\mu \hat{f}_{N,k_q,n}^{(I,Q)}$ and $\hat{f}_{T_s,k_q,n}^{(I,Q)}$, is multiplied by the tangential unit vector yielding

$$\hat{\boldsymbol{f}}_{T,j}^{(I_n,Q_m)} = = = -\frac{\Delta \dot{x}_{T,j}}{|\Delta \dot{x}_{T,j}|} \min \left(\mu \, \hat{f}_{N,k_q,n}^{(I,Q)} \, ; \hat{f}_{T_s,k_q,n}^{(I,Q)} \right), \tag{3.18}$$

The principle of action and reaction is satisfied, as the same adjusted contact force magnitudes are taken to act on particle Q. Details related to this approach are reported in [63] (Höhner, 2011). Once the normal force $\hat{\boldsymbol{f}}_{N,j}^{(I_n,Q_m)}$ and tangential force $\hat{\boldsymbol{f}}_{T,j}^{(I_n,Q_m)}$ are determined for each contact j between I_n and Q_m , their vectorial sum is used to evaluate the total force

$$\boldsymbol{F}_{TOT}^I \, [N] = \sum_j (\hat{\boldsymbol{f}}_{N,j}^{(I_n,Q_m)} + \hat{\boldsymbol{f}}_{T,j}^{(I_n,Q_m)}) \tag{3.19}$$

acting on the particle I, as well as the external torque

$$\boldsymbol{M}_{TOT}^I [Nm] = \sum_j \boldsymbol{r}_j \times (\hat{\boldsymbol{f}}_{N,j}^{(I_n,Q_m)} + \hat{\boldsymbol{f}}_{T,j}^{(I_n,Q_m)}) \tag{3.20}$$

where $\boldsymbol{r}_j$ is the position vector between the contact point j and the center of mass of the ellipsoid. The resulting forces $\boldsymbol{F}_{TOT}^I$ evaluated as the vectorial sum of the all forces acting on the three primary spheres clustered to form the ellipsoidal particle and the torques $\boldsymbol{M}_{TOT}^I$ acting on the particles determine their motion in the assembly. In classical mechanics, the motion of a rigid body is described by a translational and a rotational motion. The

translational motion is independent of the particle shape and it is defined by means of Newton's second law as

$$m^{\mathrm{I}}\,\ddot{x}^{\mathrm{I}} = \boldsymbol{F}^{\mathrm{I}}_{\mathrm{TOT}}\ ,$$

3.21

where m^{I} [kg] and $\ddot{x}^{\mathrm{I}}$ [m/s^2] are the mass and the acceleration determined by the position vector of the center of mass of particle I, respectively.

3.2.1 Equations of motion

Unlike the translational motion, the rotation is affected by the particle shape. For a non-spherical particle, the implementation of the moment of inertia in the global coordinate system is cumbersome. In order to simplify the implementation of the tensor of the moment of inertia, the rotational motion is expressed in a local coordinate system instead of the global coordinate system fixed to the assembly's cubic box. The origin of the local coordinate system is located at the center of mass of the particle with the axes oriented along the main axes of inertia as shown in Figure 3–9.
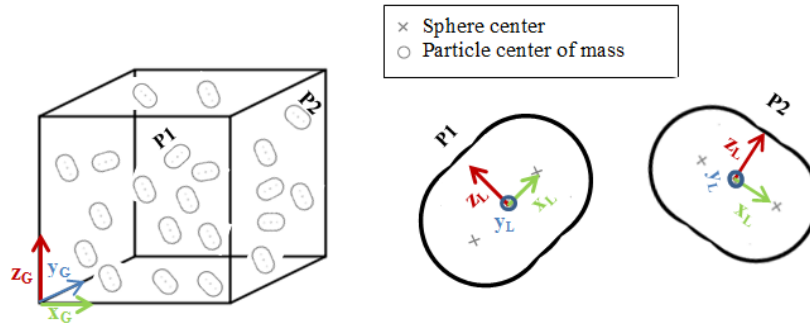

Figure 3–9: Global and local coordinate system, [119] (Moscardini et al., 2017).

Due to the particle's symmetry, the inertia tensor becomes in this coordinate system diagonal containing only the principal moments of inertia I_{xx}, I_{yy} and I_{zz} [kg m^2]. In this work, I_{xx}, I_{yy} and I_{zz} are assumed to be equal to the principal moments of inertia of a real ellipsoid charactherized by the same axis of the ellipsoidal particles here generated.

The rotational accelerations in the local frame are then evaluated by means of the Euler equations [123] (Truesdell, 1991)

$$\begin{cases} M^{\mathrm{I}}_{\mathrm{x,L}} = \dot{\omega}^{\mathrm{I}}_{\mathrm{x,L}}\,I_{\mathrm{xx}} + (I_{\mathrm{zz}} - I_{\mathrm{yy}})\omega^{\mathrm{I}}_{\mathrm{y,L}}\omega^{\mathrm{I}}_{\mathrm{z,L}} \\ M^{\mathrm{I}}_{\mathrm{y,L}} = \dot{\omega}^{\mathrm{I}}_{\mathrm{y,L}}I_{\mathrm{yy}} + (I_{\mathrm{xx}} - I_{\mathrm{zz}})\omega^{\mathrm{I}}_{\mathrm{x,L}}\omega^{\mathrm{I}}_{\mathrm{z,L}} \\ M^{\mathrm{I}}_{\mathrm{z,L}} = \dot{\omega}^{\mathrm{I}}_{\mathrm{z,L}}I_{\mathrm{zz}} + (I_{\mathrm{yy}} - I_{\mathrm{xx}})\omega^{\mathrm{I}}_{\mathrm{y,L}}\omega^{\mathrm{I}}_{\mathrm{x,L}} \end{cases} ,$$

3.22

where $\omega^I_{x,L}$, $\omega^{\mathrm{I}}_{\mathrm{y,L}}$, and $\omega^{\mathrm{I}}_{\mathrm{z,L}}$ [1/s^2] are the components of the vector $\boldsymbol{\omega}^{\mathrm{I}}_{\mathrm{L}}$ of angular velocity in the local coordinate system L, while $M^{\mathrm{I}}_{\mathrm{x,L}}$, $M^{\mathrm{I}}_{\mathrm{y,L}}$, and $M^{\mathrm{I}}_{\mathrm{z,L}}$ are the components of the vector

of the resulting torque $\boldsymbol{M}_{\text{TOT}}^{\text{I}}$ acting on particle I in the local coordinate system. Eq. 3.22 can be solved for the vector of rotational acceleration, which can then be transformed into the global coordinate system G to calculate the velocities and the positions of the particles by means of the Verlet Algorithm for the integration of the ordinary differential equations of motion [124][125] (Swope et al.,1982; Verlet,1967). The transformations between the two coordinate systems are performed via a rotation matrix. The rotation matrix can be expressed in terms of Euler angles or in terms of quaternions. However, the first approach suffers from the gimbal lock singularity. Therefore, due to the absence of singularities, the unit quaternion is the most suitable approach to be implemented in the DEM code.

3.2.2 Particle orientation

Quaternions were introduced in the nineteenth century by Hamilton [126] (Hamilton, 1844) and successively used to describe the rotational motion of a particle defining its orientation in space [127]-[131] (Kosenko, 1998; Celledoni and Säfström, 2006; Hairer and Vilmart, 2006; Zhao and vanWachem, 2013; Withmore and Hughes, 2000). A quaternion q is composed of a scalar q_0 and a vector part $\boldsymbol{q}$

$$q \ [/] = [q_0, \boldsymbol{q}], \tag{3.23}$$

where

$$\boldsymbol{q} = q_1\boldsymbol{i} + q_2\boldsymbol{j} + q_3\boldsymbol{k} \ . \tag{3.24}$$

Here, q_0, q_1, q_2 and q_3 are real numbers and $\boldsymbol{i}, \boldsymbol{j}$ and $\boldsymbol{k}$ are unit vectors along to the *x, y* and *z* axis in the global coordinate system, respectively. By means of so-called unit quaternions the pure rotation of a vector is described by two geometrical quantities: the angle of rotation α_r [rad] and the unit vector $\breve{\boldsymbol{q}}$ about which the rotation takes place. Accordingly, such unit quaternion is defined as

$$q = \left[cos\frac{\alpha_r}{2}, sin\frac{\alpha_r}{2} \ \breve{\boldsymbol{q}}\right], \tag{3.25}$$

where

$$\|\breve{\boldsymbol{q}}\| = 1. \tag{3.26}$$

After prescribing a load step, the numerical integration of the equations of motion during a relaxation process towards equilibrium is based on time steps. At time step n, by means of the angle of rotation

$$\alpha_{r,n} = \|\boldsymbol{\omega}_n\|\Delta t \tag{3.27}$$

and the normalized vector

$$\breve{q}_n = \frac{\boldsymbol{\omega}_n}{\|\boldsymbol{\omega}_n\|} \qquad\qquad 3.28$$

about which the rotation takes place, the unit quaternion $\hat{q}_n$ describing the particle rotation from time step n-1 to time step n is expressed as

$$\hat{q}_n = \left[cos\frac{\|\boldsymbol{\omega}_n\|\Delta t}{2}, sin\frac{\|\boldsymbol{\omega}_n\|\Delta t}{2}\frac{\boldsymbol{\omega}_n}{\|\boldsymbol{\omega}_n\|} \right]. \qquad\qquad 3.29$$

Here, $\boldsymbol{\omega}_n$ is the angular velocity at time step n and Δt is the time increment between time steps, meaning that $\hat{q}_n$ represents the variation of the orientation in a time step Δt. To represent the change from the initial orientation of a particle to the current orientation at time step n, the direct multiplication method was implemented. In this approach [130][131] (Zhao and vanWachem, 2013; Withmore and Hughes, 2000), the unit quaternion to enter in the current time step n is evaluated by

$$q_n = \prod_{m=1}^{n} \hat{q}_{n-m}. \qquad\qquad 3.30$$

Then, the unit quaternion for the next time level q_{n+1} is determined by

$$q_{n+1} = \hat{q}_n q_n , \qquad\qquad 3.31$$

where $\hat{q}_n$ is the unit quaternion between the time steps n-1 and n, while q_n is the product of the unit quaternions between t=0 and the time step n-1. Therefore q_n represents the total rotation from the original orientation at t=0 to the orientation at time step n-1. The non-commutative multiplication of quaternions is defined as $pq = [p_0 q_0 - \boldsymbol{pq}, p_0\boldsymbol{q} + q_0\boldsymbol{p} + \boldsymbol{p} \times \boldsymbol{q}]$, which can also be represented by a matrix operation [130] (Zhao and vanWachem, 2013). In this updating method, the typical approach based on Taylor series is avoided and the multiplication replaces the addition operator in the time integration. The multiplication between unit quaternions preserves their unit length and the further re-normalization, usually adopted after the addition operation, can be avoided. Once the components of quaternion q_n are defined in the global coordinate system, the rotation matrix

$$\underline{\underline{R}} = \begin{pmatrix} 1 - 2(q_2^2 + q_3^2) & 2q_1q_2 - 2q_0q_3 & 2q_0q_2 + 2q_1q_3 \\ 2q_1q_2 + 2q_0q_3 & 1 - 2(q_1^2 + q_3^2) & 2q_2q_3 + 2q_0q_1 \\ 2q_1q_3 - 2q_0q_2 & 2q_0q_1 + 2q_2q_3 & 1 - 2(q_1^2 + q_2^2) \end{pmatrix} \qquad 3.32$$

can be obtained. By means of the rotation matrix, the transformations between the global and the local coordinate systems L and G can be carried out as

$$\begin{pmatrix} V_{x,L} \\ V_{y,L} \\ V_{z,L} \end{pmatrix} = \underline{\underline{R}} \begin{pmatrix} V_{x,G} \\ V_{y,G} \\ V_{z,G} \end{pmatrix} \qquad\qquad 3.33$$

$$\begin{pmatrix} V_{x,G} \\ V_{y,G} \\ V_{z,G} \end{pmatrix} = \underline{\underline{R}}^T \begin{pmatrix} V_{x,L} \\ V_{y,L} \\ V_{z,L} \end{pmatrix} \qquad\qquad 3.34$$

Here, $\underline{\underline{R}}^T$ is the transposed rotation matrix, while the column matrices $\underline{V}_L = (V_{x,L}, V_{y,L}, V_{z,L})^T$ and $\underline{V}_G = (V_{x,G}, V_{y,G}, V_{z,G})^T$ consist of the Cartesian components of some vector $\boldsymbol{V}$ in local and global coordinates, respectively. In the present study, the rotation matrix is used to transform the column matrix $\underline{M}^I_{TOT,G}$ of the torque, Eq. 3.20, and the column matrix of the rotational velocity $\underline{\omega}^I_G$ from the global to the local coordinate system through Eq. 3.33. Based on these local components, the components of the rotational acceleration in the local coordinate system are obtained from Eq. 3.22. Afterwards, the transposed rotation matrix is used to transform the column matrix $\underline{\dot{\omega}}^I_L$ of the rotational accelerations from the local to the global coordinate system by means of Eq. 3.34. This has to be done for each ellipsoidal particle at each time step n. Furthermore, the quaternion and the rotation matrix of every particle need to be updated at each time step.

3.3 Numerical simulations

In this section, numerical results obtained with the above described DEM code are reported and discussed. Uniaxial compression of assemblies composed of ellipsoidal particles is simulated and the micromechanics and the macro-response of the assemblies are studied. The influence of the particles' size and shape was investigated. The effect of the MC was estimated.

3.3.1 Boundary conditions and material parameters

In order to represent the bulk behavior of the pebble bed in the blanket, periodic boundary conditions were applied all around a virtual box consisting of packed ellipsoidal particles. Using periodic boundary conditions, any wall effect on the packing structure is avoided, while the bulk behavior of the pebble bed in the blanket is reproduced with a reasonably low number of particles. Periodic boundaries were already implemented for spheres in the existing KIT-DEM-code [27][28] (Gan, 2008; Gan and Kamlah, 2010). For ellipsoidal particles, the implementation was slightly modified to consider each ellipsoidal boundary

pebble as a cluster of spheres. Further details about the implementation of periodic boundary conditions for packed spheres are reported in [27] (Gan, 2008).

The assemblies are gradually compressed applying a constant strain increment (1.25e-3% for simulations with ellipsoidal particles and 2.5e-3% for simulations with spheres) in the axial direction up to the maximum strain of 1.25%. The applied strain increments are chosen to represent quasi-static loading conditions. The maximum macroscopic axial strain of 1.25% is used in accordance with a previous study [28] (Gan and Kamlah, 2010). To represent the so-called uniaxial compression test (UCT), the assembly is kept at fixed width in the other two space dimensions perpendicular to the direction of uniaxial loading, while the periodicity of the system is maintained. When the maximum strain is reached, the assembly is gradually unloaded until the stress σ_{33} approaches zero. For each iteration, the stress is evaluated by the interaction forces acting between pebbles [28]. The assemblies generated by means of the RCP contain 5000 mono-sized ellipsoidal particles of Li_4SiO_4 packed in a virtual cubic box. The physical and mechanical properties used are given in Table 3–1. In this work the shear stiffness is $K_s = 16/3G_{eff}$ [33] (Zhao et al., 2013), where $G_{eff}[Pa] = E/4(1 + v)(2 - v)$.

Simulations with a starting PF ranging from ~62.5% to ~64.27% were carried out to study its impact on the assemblies' mechanical behavior. High starting packing factors are reached by means of the developed RCP without the use of artificial gravity or preloading generating assemblies free of overlaps with a low number of contacts. During the very first few compression steps the number of contacts among particles rapidly increases to then approach a much reduced rate of growth. However, the variation of the PF during these very first few compression steps is negligible. Therefore the starting packing factor is representative of the initial bulk packing structure. The influence of the particle shape was examined by varying both the radius of the primary spheres composing the individual ellipsoidal particle and the aspect ratio in the range of 0.2-0.25mm and ~1.03-1.12, respectively. The investigated range is consistent with the sphericities of the currently produced pebbles. The reported aspect ratios have been rounded at the second digit.

Table 3–1: Physical and mechanical properties of pebbles

Parameter	Value
Density of bulk material ρ	2260 kg/m^3 [132] (Löbbecke and Knitter, 2007)
Young's modulus E	90 GPa [133] (Zaccari and Acquaro, 2007)
Poisson Ratio v	0.25 [133] (Zaccari and Acquaro, 2007)
Friction coefficient μ	0.1 [28] (Gan et al., 2010)
Shear Stiffness K_s	~55 GPa

3.3.2 Mechanical response

Influence of the packing factor

In order to investigate the influence of the packing factor on the stress-strain curves, assemblies of monosized ellipsoidal particles with an aspect ratio equal to ~1.12, individually composed of three monosized spheres with a radius of 0.25mm, were generated. Numerical results are shown in Figure 3–10(a). In agreement with the previous studies carried on assemblies of spherical pebbles [28] (Gan and Kamlah, 2010), the initial PF was found to noticeably affect the mechanical response of the investigated assemblies. A slight modification of the initial PF results in a considerable variation of the generated stress state, which has potential impact on the overall thermo-mechanical properties of the beds. Reducing the initial PF the assemblies exhibit a more compliant behavior showing a larger residual strain after unloading. In particular, the assembly characterized by the highest PF shows the stiffer behavior (higher stress for a given strain), and at the same time the lowest residual strain of about 0.8% after the unloading. The generated stress at the end of loading reaches about 3.5 MPa. At the other end, the loosely packed assembly (PF≈62.5%) shows a lower stress build-up for the same maximum imposed strain. This assembly reaches a maximum stress of 0.35 MPa at the end of loading while showing a residual strain of 1.16% after unloading. This indicates a massive rearrangement of the elastic particles contained in the assemblies during compression. Using the in-house DEM code previously developed [27] (Gan, 2008), assemblies of monosized spheres with initial PFs similar to those used for Figure 3–10(a) for assemblies of ellipsoidal particles have been generated and successively investigated. The sphere radius is set to 0.25mm. The obtained stress-strain curves are shown in Figure 3–10(b).
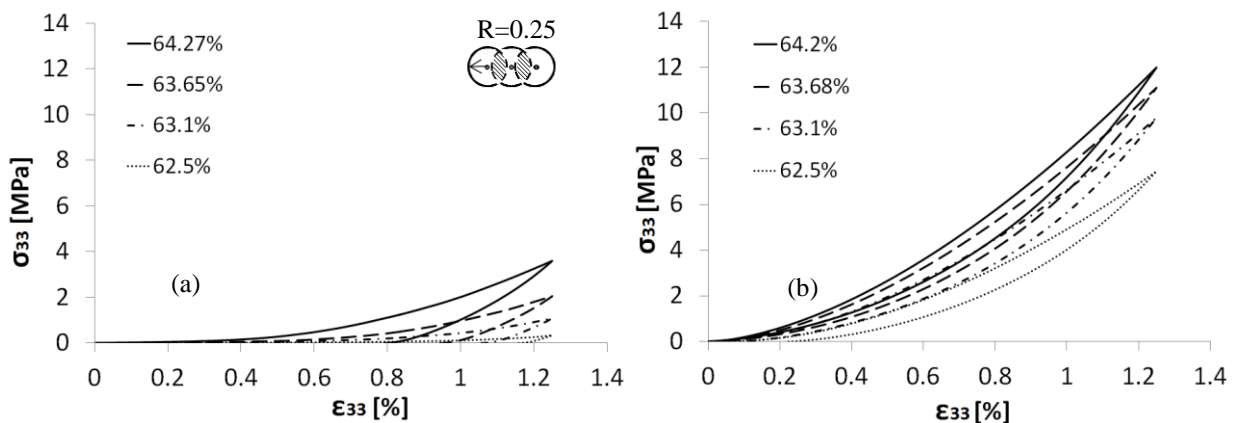
Figure 3–10: Stress-strain curves for assemblies (a) of ellipsoidal particles with ar ~1.12 and (b) equal-packed spheres with R=0.25mm, [119] (Moscardini et al., 2017).

The assemblies composed of mono-sized spheres show a much stiffer mechanical response than the equivalently packed assemblies of ellipsoids with a relatively small or even negligible residual strain after unloading. This evidences that assemblies of mono sized spheres are more close to their maximum achievable PF in comparison to assemblies of ellipsoids with the same initial PF. Therefore, even if the initial packing factor is the same, the assemblies of ellipsoidal particles are less dense in this sense of being more far away from the theoretical maximum PF. In this regard, Donev et al., in 2004 [134] demonstrated that compared to the maximum packing factor obtained with spheres ordered in the face centered cubic configuration (≈ 0.7405), laminate crystal packing of ellipsoids in face-centered layer reaches higher density for a wide range of aspect ratios. In particular, for prolate ellipsoids a maximum packing factor of ~0.77 is reached with an aspect ratio of about 1.7. Therefore, since for face-centered structures ellipsoidal particles reach higher packing factors compared to spheres, it is reasonable to expect a similar behavior for random structures. Results suggest that a slight deviation from a perfectly spherical shape can remarkably influence the packing behavior of a pebble bed, shifting the maximum obtainable PF to higher values. Furthermore, during the compression (or packing) the ellipsoidal particles have a higher mobility in the assembly (in comparison with spherical pebbles) due to the extra degree of freedom associated to the rotation. Particles can change their orientation finding more easily a new equilibrium configuration compared to spherical pebbles. This, together with the assembly being further away from its maximum PF, explains the softer mechanical behavior of the investigated assemblies.

Influence of the shape

Firstly, sensitivity studies were performed on assemblies of monosized ellipsoidal particles with the same initial packing factor of about 63.65-63.66% varying the aspect ratio in the range ~1.03-1.12. Particles are individually composed by three monosized spheres with a radius of 0.25mm. Numerical results are reported in Figure 3–11. The curves exhibit a strong dependence of the mechanical behavior on the particle shape. A small reduction of the aspect ratio results in a remarkable increment of the maximum stress and in a distinct reduction of the residual strain after unloading. Decreasing the aspect ratio from around 1.12 to 1.03, the behavior of the investigated assemblies becomes stiffer approaching the curve of the spherical particles of 0.25mm of radius. This is an evidence of the proper implementation of the method for non-spherical particles presented in this paper. The increase of the maximum stress at the end of loading was found to be nonlinear with the reduction of the particles' aspect ratio. As a

consequence of the results reported in Figure 3–11, the influence of the particle shape on the pebble packing behavior can be stated such that even if the assemblies are generated with very similar PF, assemblies with higher aspect ratio in the simulated range are further away from the corresponding maximum obtainable PF.
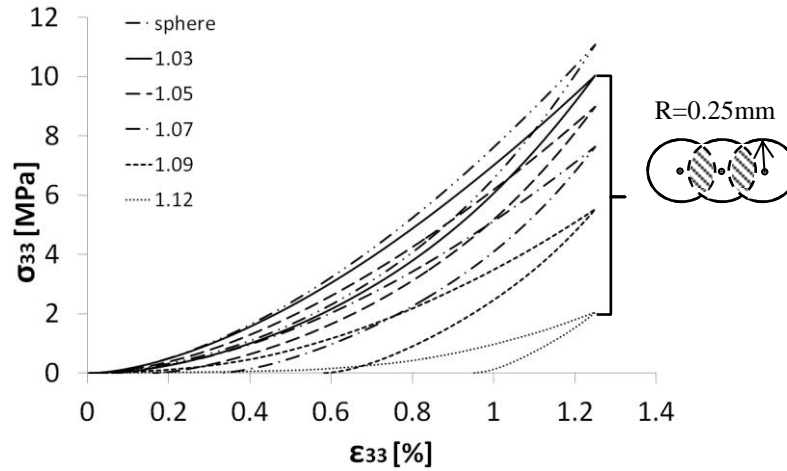

Figure 3–11: Stress strain curves of assemblies of ellipsoidal particles with an initial PF~63.66% and aspect ratios in the range 1, … , ~1.12, [119] (Moscardini et al., 2017).

The more compliant mechanical behavior of the assemblies consisting of ellipsoidal particles, compared to the equivalent packed assembly of spheres is due to two reasons. The first one is that structures generated with ellipsoidal particles are further away from their respective maximum obtainable PF in comparison to assemblies of spheres with same PF, in particular for the assemblies with higher aspect ratio. The second reason is the higher mobility of the ellipsoidal particles, due to additional degrees of freedom in rotation, compared to spheres. The slightly different mechanical behavior between spheres and ellipsoidal particles with an aspect ratio of ~1.03 is mainly due to the higher mobility of the ellipsoids in the assembly, while we associate the softer behavior at higher aspect ratios to these structures being further away from their maximum PF, mostly. These statements are further validated by the graphs reported in Figure 3–12 and in Figure 3–13. Figure 3–12 shows the coordination number (CN) evaluated for the loading path, in function of the hydrostatic pressure. For ellipsoidal particles, CN is evaluated as the ratio between the effective number of contacts in the whole assembly and the number of ellipsoidal particles. The effective number of contacts is evaluated counting eventual multiple contacts between a pair of particles as a single contact. For a fixed value of hydrostatic pressure, the coordination number increases with increasing aspect ratio. This confirms that ellipsoidal particles with a higher aspect ratio rearrange more easily with the result of increasing their contacts with the neighbours. As a consequence, a higher coordination number is reached at the same level of hydrostatic pressure.
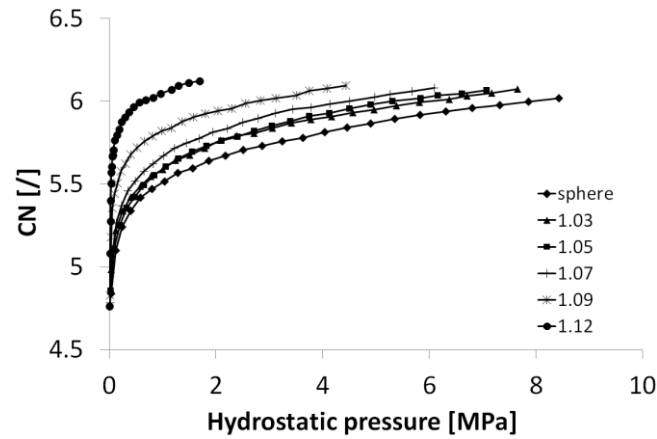
Figure 3–12: Coordination number vs hydrostatic pressure for assemblies of particles with a PF ~63.66% and aspect ratios in the range 1, …,~1.12, [119] (Moscardini et al., 2017).

Figure 3–13 exemplarily displays the oedometric modulus during the unloading path as function of the uniaxial strain for different aspect ratios. The oedometric modulus (E) was continuously calculated as $E_i = \Delta\sigma_{33,i}/\Delta\varepsilon_{33,i}$ during the unloading until the stress in the assembly approaches zero. Here $\Delta\varepsilon_{33,i}$ is the difference of the strain between two consecutive time steps while $\Delta\sigma_{33,i}$ is the respective stress change. In order to smooth out numerical oscillations of E_i, the value of the oedometric modulus to be plotted in Figure 3–13 at each strain step is obtained by averaging 5 consecutive values of E_i for spheres and 10 for the ellipsoidal particles according to the different applied strain increment discussed in Section 3.3.1. The calculated values were then plotted in Figure 3–13 as function of the mean values of the strain evaluated in the corresponding range. A decrease of E with releasing the compressive load is observed for all investigated aspect ratios. For a fixed value of strain, the oedometric modulus decreases with increasing the aspect ratio. This confirms that assemblies of ellipsoidal particles have a more compliant mechanical behavior and this effect is enhanced with higher aspect ratios. All these observations together suggest that it is easier to impart deformation in systems of ellipsoidal particles compared to spheres.
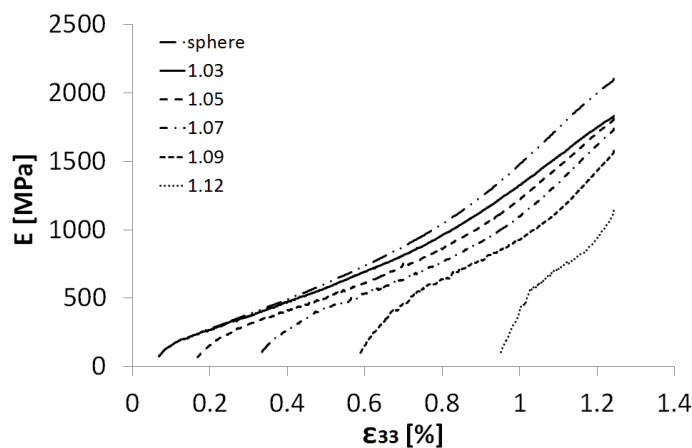
Figure 3–13: Oedometric modulus vs hydrostatic pressure for assemblies of 5000 particles, PF~63.66% and aspect ratios in the range 1, … , ~1.12, [119] (Moscardini et al., 2017).

A further sensitivity study was carried out varying the radius of the spheres composing each ellipsoidal particle assigning a different size of the radius along the major axis. Four assemblies consisting of 5000 monosized ellipsoidal particles with an aspect ratio of 1.1 were generated with a PF of ~63.6%. In the first assembly, the ellipsoidal particles are composed of three monosized spheres with a radius of 0.25mm, thus the ratio between the size of the central sphere over the size of the two external spheres is $R_e/R_c=1$. In the other three assemblies the central sphere has always a radius of 0.25mm, while the ratio R_e/R_c is equal to 0.95, 0.91 and 0.8, respectively. A representation of the four types of ellipsoidal particles with the related assemblies is shown in Figure 3–14, while the corresponding numerical results are presented in Figure 3–15.

$R_e/R_c=1$ $\qquad$ R_e/R_c $\qquad$ $R_e/R_c=0.91$ $\qquad$ $R_e/R_c=0.8$
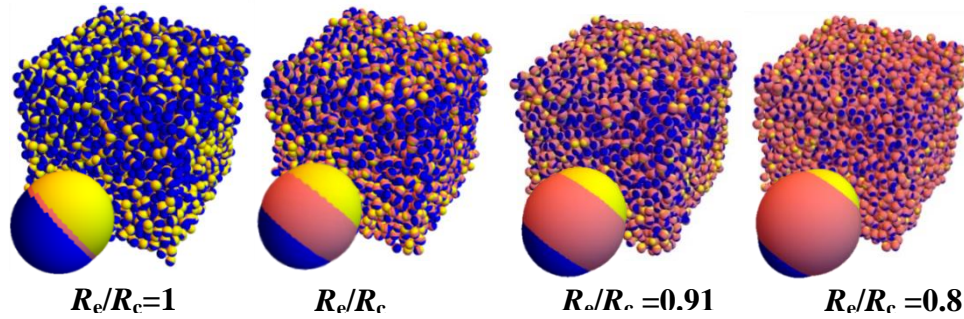
Figure 3–14: Four assemblies consisting of 5000 monosized ellipsoidal particles with same aspect ratio of 1.1 and PF~63.6% , composed by primary spheres with different radii.
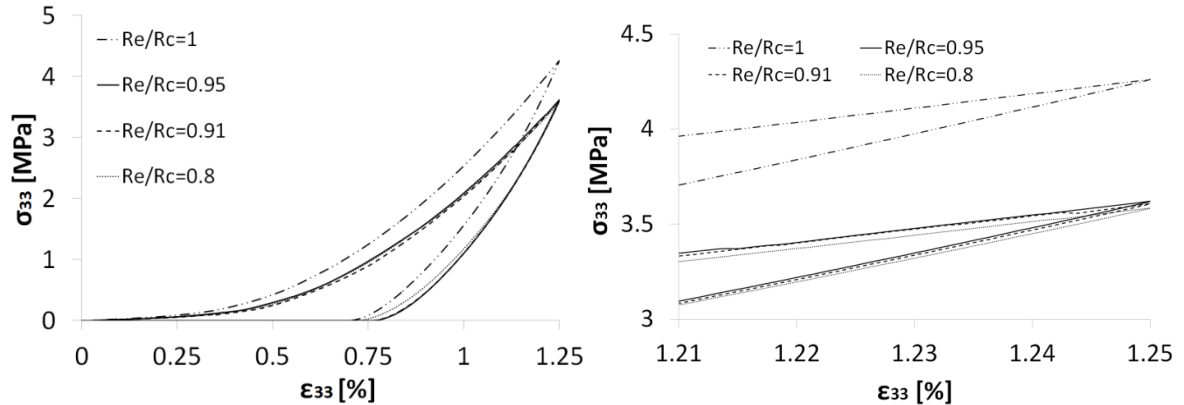
Figure 3–15: Stress-strain curves for assemblies of monosized ellipsoidal particles composed by primary spheres with different radii. The right graph is the magnified part at high stresses.

The stress-strain curves reveal an influence of the ratio R_e/R_c on the mechanical behavior of the assemblies. A reduction of ~5% of the radius of the external spheres determines a reduction of the maximum stress of ~14%. Further reductions of the radius of the external spheres have no effects on the macro mechanical behavior of the assembly. Therefore, even at a minimum value of the ratio R_e/R_c, the increase of the mobility of the particles in the assembly due to the reduction of the external particle's radius is limited.

Multi-contact effect

The results described above have been obtained by implementing in the code the method described in the Section 3.2.1 to reduce the influence of MCs. For a broader understanding of the issue, the influence of MCs was investigated whether counting or not MCs for the same assembly first. Then, keeping fixed the aspect ratio, the mechanical behavior of assemblies composed by ellipsoidal particles of 3, 5 and 7 spheres was investigated.

In Figure 3–16, three stress–strain curves are shown: the solid line is related to the assembly of spheres with a radius of 0.25mm, the dotted and the dashed lines refer to assemblies of ellipsoidal particles with an aspect ratio of ~1.03 accounting for MCs and not, respectively. The initial PF is ~63.66% in all three cases. Accounting for the additional contact forces introduced by the MCs, an overestimation of the stress is observed. The simulated curve gets even over the stress-strain curve of the sphere assembly. This was judged as an unrealistic behavior compared to true ellipsoids. The effect of the MCs on the coordination number, as a function of the strain, is shown in Figure 3–17.

The method implemented in the code to reduce the influence of the MCs introduces an asymptotic approximation towards the results of sphere assemblies, as Höhner *et al.* (2011) highlights in [62]. Moreover, to represent a more realistic contact model, a non-linear contact law was applied in this work, unlike the linear contact model implemented in [63](Höhner *et al.*, 2011). This non-linearity is assumed to lead to a larger difference between results obtained leaving the MCs and removing the MCs. Therefore, the correction introduced by the method to remove the effect of the MCs is expected to be more important compared to the linear contact model especially when a large number of multi contacts are detected.
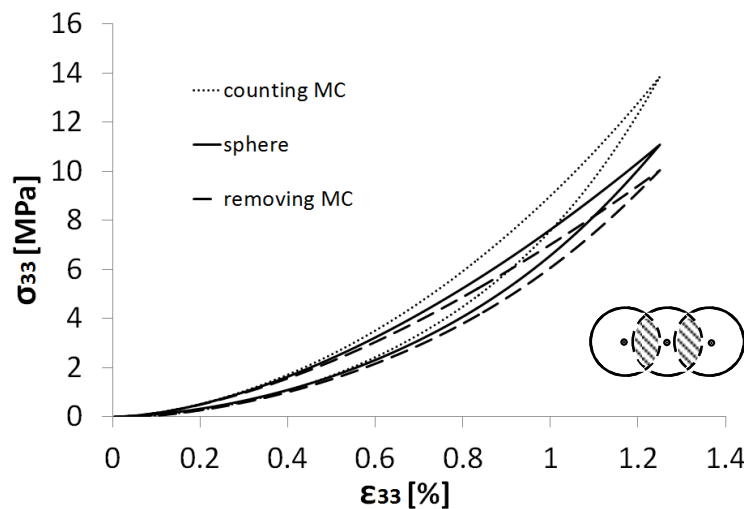

Figure 3–16: Comparison between mechanical behavior of equal-packed assemblies (PF~63.66%) of spheres (*R*=0.25mm) and of ellipsoidal particles (a_r~1.03), accounting for MCs and not, [119] (Moscardini et al., 2017).
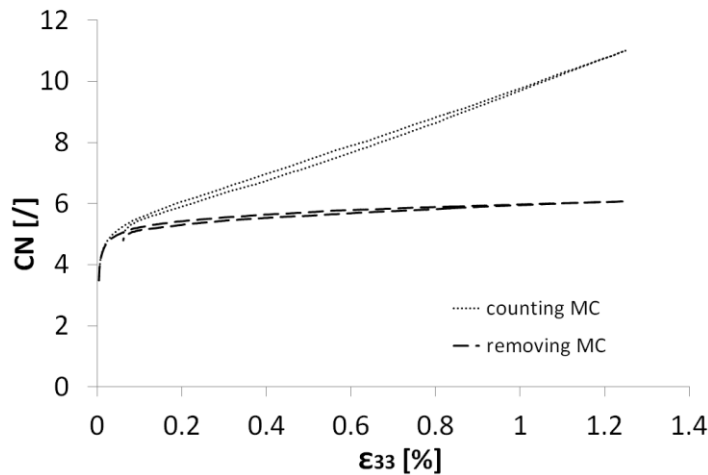
Figure 3–17: The evolution of coordination number for given values of strain whether counting or not the MCs, [119] (Moscardini et al., 2017).

Sensitivity studies were conducted to investigate the effectiveness of the implemented method to remove the MCs. To this end the mechanical behavior of three assemblies consisting of monosized particles with an aspect ratio of 1.12 composed of 3, 5 and 7 monosized primary spheres was studied. The radius of the primary spheres is 0.25mm; the three assemblies have a similar PF of about 63.6%. The assemblies were subjected to uniaxial compression. Figure 3–18 shows the obtained stress-strain curves, while in Figure 3–19 the MCs number in function of the imposed strain on the three assemblies is presented. Results for the assemblies of ellipsoidal particles composed of 3 and 5 primary spheres show a negligible influence of the number of the primary spheres on the mechanical behavior. In this case, the code is able to properly remove the effect of the overestimation of the stress induced by MCs. However, when 7 primary spheres are used to generate the ellipsoidal particles, a stiffer behavior is observed. Each contact generates a contact area between primary spheres belonging to two different ellipsoidal particles. When MCs occur, multi-contact areas are detected between two contacting ellipsoidal particles. These multi-contact areas can overlap in part each other generating a redundancy, which increases when for a given aspect ratio more primary spheres are used. It is assumed that the generated redundancy of the contact area in overlap together with the use of the non-linear contact law determine a limit for the applicability of the method to remove the MCs. Indeed, when more primary spheres are used for a given aspect ratio, larger deviations from the correct result are generated. This suggests a relation between the number of primary spheres used to compose an individual ellipsoidal particle and its aspect ratio. In particular, while a low number of primary spheres has to be avoided to guarantee a sufficient smoothness of the particles' surface, a high number of primary spheres can generate an eccessive redundancy of the multi-contact area in overlap.
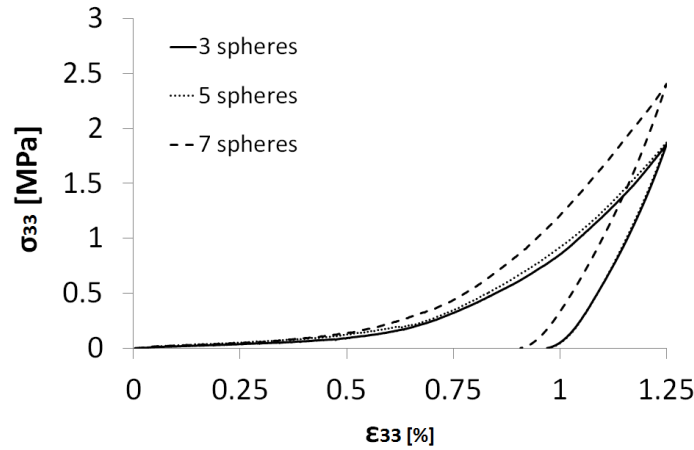
Figure 3–18: Stress-strain curves obtained with three assemblies of monosized ellipsoidal particles (a=1.12) composed of 3, 5 and 7 monosized spheres (R=0.25mm), respectively.
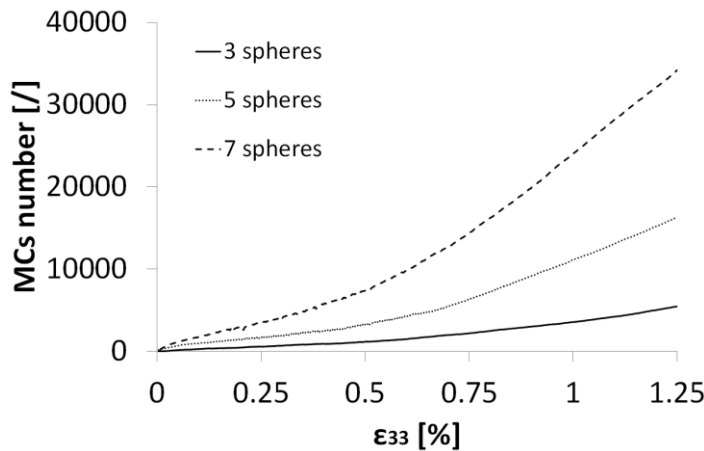

Figure 3–19: MCs number in function of the imposed strain on three different assemblies of monosized ellipsoidal particles (a=1.12) composed of 3, 5 and 7 monosized spheres (R=0.25mm).

For the chosen aspect ratio of 1.12, the ellipsoidal particles composed of 3, 5 and 7 spheres exhibit an overlap between two consecutive primary spheres of ~1.88R, ~1.94R and ~1.96R, respectively. Therefore, moving from 5 to 7 primary spheres the overlap between two consecutive spheres increases by 2 percentage points(from 194 to 196% of the radius) against an increase of 6 percentage points between 3 and 5 primary spheres (from 188 to 194% of the radius). This suggests that, for the investigated aspect ratio, the increase from 3 to 5 primary spheres lead to an effective improvement of the smoothness of the particle surface limiting the redundancy of the multi-contact area in overlap. When more than 5 spheres are used for the investigated aspect ratio of 1.12, the improvement of the smoothness of the particle surface is negligible, while the redundancy of the multi-contact area in overlap strongly increases as the number of the MCs. This lead to an unrealistic behavior due to the pileup of the stress determined from the approximation introduced by the applied method. From these preliminary studies it can be concluded that the implemented method is able to properly

remove the effect of MCs reducing the effect of the redundancy, until an effective improvement of the smoothness of the surface is achieved for the investigated aspect ratio.

3.3.3 Statistical analysis

By means of the DEM simulations, the micro response at the pebble scale can be studied. The probability distribution of the normal contact forces as well as the dependence of the contact forces on the macroscopic stress was investigated for assemblies of ellipsoidal particles. Results were then compared to values obtained from assemblies of packed spheres.

The normal force f_{ave} is the mean value of all normal interactions inside the assembly, while the maximum normal force f_{max} is the maximum absolute value among all the normal forces acting on the considered particle. Figure 3–20(a) shows the probability distributions of the normalized normal forces f/f_{ave}, while Figure 3–20(b) illustrates the distribution of the normalized maximum normal forces f_{max}/f_{ave}. Results refer to five assemblies of monosized ellipsoidal particles with different aspect ratios and one assembly of monosized spheres with the same initial packing factor of 63.66% at the strain rate of 1.25%. As shown, both probability distributions are substantially unaffected by the investigated aspect ratios of the packed particles. For both probability distributions, the assemblies composed of ellipsoidal particles with different aspect ratios show similarities. They all perfectly overlap with each other and with the probability distributions of spheres. In agreement with previous studies carried out for assemblies of monosized spheres with different initial packing factors [28] (Gan and Kamlah, 2010), the peak of the distribution is located at $f/f_{ave}< 1.0$. However, the peak of the probability distribution of the normalized maximum contact force is located at 1.5, suggesting that most of particles inside the assembly have a maximum contact force larger than f_{ave}.
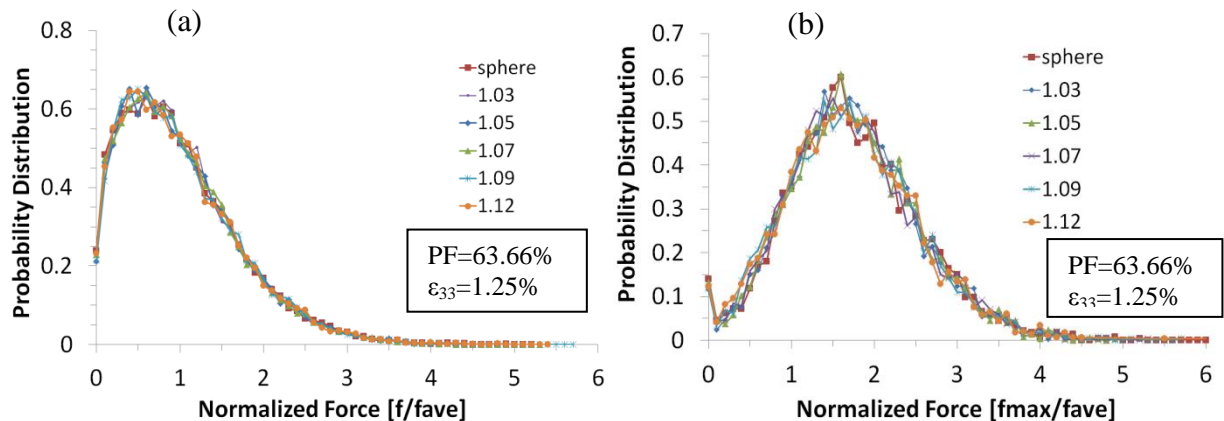

Figure 3–20: Probability distribution of normalized normal (a) and maximum (b) contact forces for assemblies of ellipsoidal particles with different aspect ratios and spheres.

Figure 3–21 shows the variation of the average normal force (a), maximum normal force (b), and scaled coordination number (c) as a function of the hydrostatic pressure for assemblies composed of monosized ellipsoidal particles with different aspect ratios. Results are compared to the assembly of monosized spheres with the same initial packing factor.

As shown in Figure 3–21(a), data points are well fitted with the linear correlation

$$f_{ave}[N] = 0.213\, p_h\,,$$
<div align="right">3.35</div>

where, p_h is the hydrostatic pressure. Therefore, knowing the hydrostatic pressure, the average normal force acting on the packed particles is determined by means of the Eq.3.35 regardless of the particle shape. On the contrary, as already shown in Figure 3–12, there is not a unique correlation linking the CN of ellipsoidal particles with different aspect ratios to the hydrostatic pressure. However, as shown in Figure 3–21(b), by scaling the value of CN with the parameter

$$\Sigma \left[\frac{N}{mm^3}\right] = \frac{PF\, f_{ave}}{\frac{3}{4\pi}V_p}$$
<div align="right">3.36</div>

a unique linear correlation is found:

$$CN * \Sigma\, [N/mm^3] = 49.85\, p_h.$$
<div align="right">3.37</div>

Here, knowing the PF, the particle volume V_p and evaluating f_{ave} by means of Eq.3.35, CN is determined as a function of the hydrostatic pressure regardless of the particle shape of monosized packed particles. The way to calculate the quantities in Eqs. 3.36 and 3.37 is described in detail below. Starting from the definition of hydrostatic pressure [27] (Gan, 2008)

$$p_h\,[MPa] = \frac{\sigma_{11} + \sigma_{22} + \sigma_{33}}{3} = \frac{1}{3V}\left(\sum_{I<J} \delta^{(I,J)} f_N^{(I,J)}\right),$$
<div align="right">3.38</div>

where, $\delta^{(I,J)}$ [mm] is the distance between two contacting particles I and J and $f_N^{(I,J)}$[N] is the related normal force, further parameters have to be introduced. First, the distance

$$\delta^*[mm] = \left(\sum_{I<J} \delta^{(I,J)} f_N^{(I,J)}\right)/\sum_{I<J} f_N^{(I,J)}$$
<div align="right">3.39</div>

of the particles weighted by the normal force is defined. Then, the average normal force is evaluated as the ratio between the sum of the all normal forces acting among particles in the assembly counted twice and the total number of contacts ($CN * N_p$):

$$f_{ave}[N] = \frac{2\sum_{I<J} f_N^{(I,J)}}{CN\ N_p}.$$ 3.40

With the help of Eq. 3.39 and Eq. 3.40, $\sum_{I<J}\delta^{(I,J)} f_N^{(I,J)}$ and $\sum_{I<J} f_N^{(I,J)}$, respectively can be eliminated from Eq. 3.38, such that p_h becomes

$$p_h\ [MPa] = \frac{N_p\ CN\ f_{ave}\ \delta^*}{6V}.$$ 3.41

Using the definition of the packing factor as the ratio of the volume of all particles over the box volume, i.e. $PF = N_p V_p/V$, p_h is written as

$$p_h\ [MPa] = \frac{PF\ CN\ f_{ave}\ \delta^*}{6V_p}.$$ 3.42

Now, approximating V_p by the volume of a real ellipsoid, in which the two minor axes are equal to the radius of the primary spheres and the major axis is evaluated as a function of the aspect ratio of the ellipsoidal particles ($V_p = \frac{4}{3}\pi R^3 a_r$), Eq. 3.42 becomes

$$p_h\ [MPa] = \frac{PF\ CN\ f_{ave}\ \delta^*}{8\pi R^3 a_r}.$$ 3.43

Grouping the parameters derivable from experiments which are PF, R^3, a_r and $f_{ave,}$, Σ is obtained as

$$\Sigma\left[\frac{N}{mm^3}\right] = \frac{PF\ f_{ave}}{R^3 a_r} = \frac{PF\ f_{ave}}{\frac{3}{4\pi} V_p}$$ 3.44

and the Eq. 3.43 now reads as

$$p_h\ [MPa] = \frac{\delta^*}{8\pi}\ \Sigma\ CN.$$ 3.45

Comparing Eq. 3.45 with the equation of the linear interpolation shown in Figure 3–21(b), one gets $\frac{\delta^*}{8\pi} = 49.85$ giving $\delta^* = 0.5\ mm$ as constant value. This suggests that the weighted distance in the investigated assemblies is approximately equal to the minimum distance between two ellipsoidal particles, which minor axis is equal to the radius of the primary spheres of 0.25mm.

Figure 3–21(c) shows the maximum forces inside the assembly with respect to the hydrostatic pressure. Neglecting scatter in data due to few particles inside the assembly with a very high maximum force, an accurate estimation of the data is given by the correlation

$$f_{max} = 1.2081\ p_h^{0.9233}$$ 3.46

Together with numerical results obtained for the investigated assemblies, a solid blank line is shown in Figure 3–21(c). The line is the representation of the relation founded by Gan (2008) [27] ($f_{max} = 5.47\underline{+}0.474\, f_{ave}$) for assemblies of monosized spheres with different initial packing factors. In agreement with the previous study [27] (Gan, 2008), the founded correlation fits perfectly also assemblies of ellipsoidal particles with different aspect ratios. The evaluation of the maximum force together with the distributions of the normal contact forces is an essential input to estimate the crash probability of pebbles. With the equations reported in this section it is possible to access to micromechanical information of the investigated assembly just knowing the hydrostatic pressure and parameters derivable from experiments.
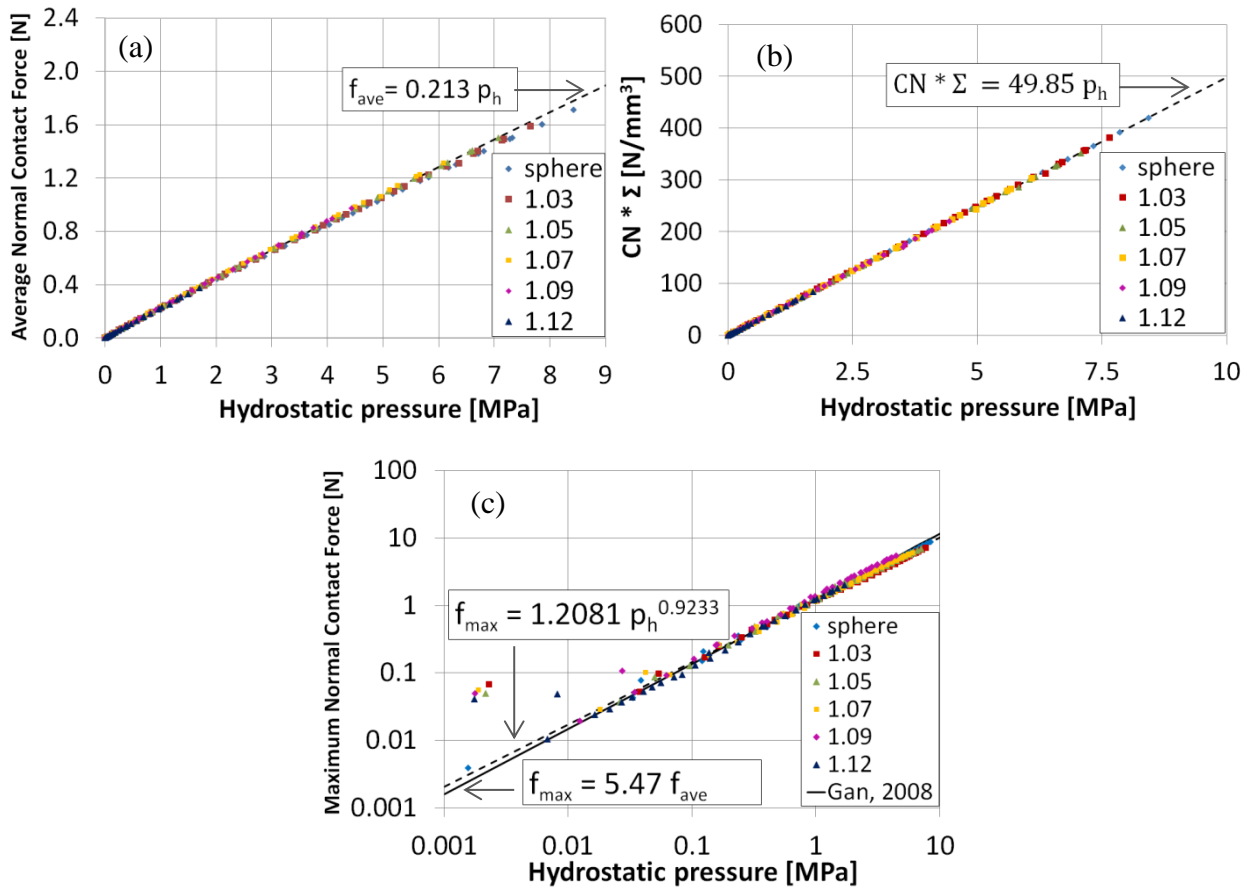
Figure 3–21: Average normal force (a), maximum normal contact force (c) and scaled coordination number (b) over hydrostatic pressure for assemblies of monosized spheres and ellipsoidal particle.

Chapter 4

DEM for heat transfer in packed spheres

Pebble beds are multiphase materials in which both the solid and the gas phase filling the voids between particles coexist. The heat transfer inside pebble bed depends on the effective thermal properties of the bed, thus on the thermal properties of the two phases as well as on the system properties (e.g. gas pressure, temperature etc.). In particular, the pressure of the system is a key parameter for the heat transfer in a packed granular assembly since the thermal conductivity of a confined gas decreases with decreasing pressure (known as Smoluchowski effect). In this chapter, an innovative thermal Discrete Element Method is presented. The method allows simulating the heat transfer inside packed spheres accounting for the influence of the gas pressure on the effective thermal conductivity, for the first time in a DEM code. First, the 3D thermal network model implemented to simulate the heat transfer among particles will be described in detail. Then the calibration and the validation of the code by comparison with existing experimental literature data will be presented.

4.1 3D thermal network model

In this section, the 3D thermal network model based on the theory proposed by Batchelor and O'Brien [78] and later used in [79] (Yun and Evans, 2010) and [80] (Kanupharti et al., 2008) was implemented to determine the heat exchange in packed systems under an imposed thermal gradient (see also Moscardini et al., 2018 [77]). The particle interconnection is defined by thermal resistors, which are the nodes of the network simulating the resistance to the heat transfer between two contacting particles as function of the thermal contact type. The further extension implemented to include the influence of the interstitial gas pressure by including the Knudsen number in the thermal contact conductance model is reported in detail. This decisive step allows to study, for the first time by means of a DEM code, the influence of the interstitial gas pressure on the heat transfer and thus on the effective thermal conductivity in the gas flow transition region named Knudsen domain.

4.1.1 Global thermal model

To investigate the heat transfer in a granular system and to determine the effective thermal conductivity of the packed assembly, an in-house thermal-DEM code was developed. A 3D thermal resistor network model was implemented to determine the heat exchange in packed systems under an imposed thermal gradient. Monosized and polydispersed packed granular

systems were generated by means of a modified version of the Random Close Packing (RCP) algorithm described in [28] (Gan and Kamlah, 2010) and [31] (Annabattula et al., 2012). The RCP presented in [28] (Gan and Kamlah, 2010) and [31] (Annabattula et al., 2012) generates assemblies of packed spheres in periodic configuration. As already explained in Chapter 3, with the implementation of periodic boundary conditions (PBCs), the generated assemblies represent the bulk region of the pebble beds. In order to apply a thermal gradient along the height of the assemblies, the RCP was slightly modified as in [29] (Gan et al., 2010). The PBCs in the upper and bottom boundaries were replaced by rigid walls. As thoroughly explained in the previous chapter and in [29] (Gan et al., 2010), during the iterations the desired packing factor is approached reducing the radius of the spheres. The diameter of the particles is equal to the desired value only if the objective packing factor is reached. Otherwise if a slight variation between the objective and the obtained PF occurs, the radius of the particles is scaled to match the objective PF with the desired particle size.

In a granular system two phases coexist. Pebbles as a whole identify the solid phase composing the skeleton of the system, while the interstitial gas represents the matrix of the system. In the implemented thermal contact conductance model, the pebbles are interconnected by thermal resistors defined by the different type of thermal contact. Thermal resistors represent the nodes of the thermal network. The heat q_{ij} transferred between the two particles i and j is

$$q_{ij} = C_{ij}^{eff}(T_i - T_j). \qquad 4.1$$

Here, T_i and T_j are the temperatures of particle i and j, respectively. An individual temperature is assigned to each particle. C_{ij}^{eff} [W/K] is the local effective conductance, which is evaluated as a function of the type of the thermal contact. Equations defining C_{ij}^{eff} will be reported in Section 4.1.2. Then, q_{ij} [W] can be evaluated at each time step for each contact in the whole assembly. The rate of temperature change $\dot{T}_i$ of the i-th pebble is updated as

$$\dot{T}_i = \sum_j \frac{q_{ij}}{m_i \, c_p}, \qquad 4.2$$

where m_i [kg] and c_p [J/kg K] are the mass and the heat capacity of the solid material, respectively. When a particle inside the assembly is in contact with a boundary particle, which is the periodic neighbor obtained as particle-image from the rigid translation of the pebble located inside the box to the opposite surface, the adiabatic condition $q_{ij} = 0$ is applied. For an imposed thermal gradient, the calculation ends when the assembly reaches the steady state configuration according to

$$\frac{\sum_i m_i c_p T_i^n - \sum_i m_i c_p T_i^{n-1}}{\sum_i m_i c_p T_i^{n-1}} < \text{TOL,} \qquad\qquad 4.3$$

where TOL is set to 10^{-10} for a typical time steps of ~0.01-1sec. The convergence criterion in Eq. 4.3 is formulated in analogy to a variation of the thermal energy in the assembly between two consecutive iterations. However, the chosen value for TOL refers to T expressed in degree Celsius. The thermal diffusion time defined as

$$\delta t = \frac{\rho \, c_p \, R_{min}^2 \tau^2}{k_s} \qquad\qquad 4.4$$

determines the time step required to achieve the solution for the explicit scheme used in the simulation [81] (Gan et al., 2014). Here, the ratio $\left(\frac{\rho \, c_p}{k_s}\right)^{-1}$ [m^2/s] represents the thermal diffusivity of the solid material, which determines the heat transfer rate in the particles. ρ [kg/m^3] and k_s [W/mK] are the density and the thermal conductivity of the solid material, respectively. The minimum thermal diffusion time in the assembly is defined by dividing the square of the minimum radius in the assembly R_{min}^2 [m^2] by the thermal diffusivity of the solid material. The parameter τ [/] is introduced to ensure stability of the calculation for several conditions (e.g. different gas pressure, gas type, solid materials, radius of the particles etc.). A value of τ =0.5 ensured the stability and the convergence of the simulations in every condition. However, under certain conditions such as low gas pressure or small pebble diameters τ=0.5 turned out to be too restrictive resulting in a long computation time. In these circumstances τ can be increased (e.g. to 1, 2, 4) to reduce the computational time as long as the convergence is assured without affecting the results of the simulation. Once that the steady state configuration is reached, the effective thermal conductivity of the assembly is evaluated as

$$k_{eff} = \frac{\sum_i q_{i,bw} \, H}{A \, (T_{top} - T_{bottom})}, \qquad\qquad 4.5$$

where $\sum_i q_{i,bw}$ [W] is the total heat transferred between pebbles and the bottom wall. H [m] and A [m^2] are the height and the cross sectional area of the assembly, respectively. $T_{top} - T_{bottom}$ is the imposed thermal gradient between the top and the bottom wall, set to 1K in this work.

4.1.2 Effective thermal contact conductance

In the 3D thermal network, each contact is defined as a series circuit consisting of three resistors. As exemplarily shown in Figure 4–1, the three resistors represent the resistance to the heat transfer in the two solid particles and in the thermal contact region. The respective

thermal conductances are namely C_i^s, C_j^s and C_{ij}^{ct} [W/K]. This basic configuration defines the local effective thermal conductance of the contact pair as

$$C_{ij}^{eff} = \left[\frac{1}{C_i^s} + \frac{1}{C_{ij}^{ct}} + \frac{1}{C_j^s} \right]^{-1}.$$

4.6

To evaluate C_i^s, C_j^s and C_{ij}^{ct}, the theoretical derivation developed in [78] (Batchelor and O'Brien, 1977) and applied in [79] (Yun and Evans, 2010) and [80] (Kanupharti et al., 2008) was adopted.
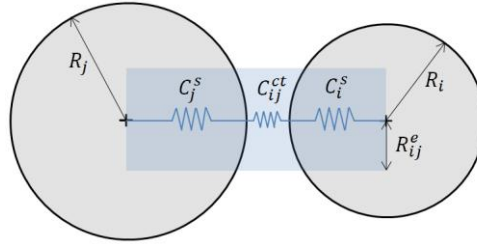

Figure 4–1: Contacts defined as a series circuit of three resistors: solid-contact-solid, [77] (Moscardini et al., 2018).

The thermal contact is assumed to be a contact area between touching particles (overlap type contact, Figure 4–2(a)) or a separation gap (gap type thermal contact, Figure 4–2(b)). When the distance between the centers of the two particles D_{ij} [m] is greater than the sum of their radii, the thermal contact is defined as a separation gap with a characteristic distance of

$$h_{ij} = D_{ij} - (R_i + R_j).$$

4.7

Otherwise, according to Hertzian contact theory, a contact area defined by a contact radius as

$$r_c = \sqrt{|h_{ij}| \frac{R_{ij}}{2}}$$

4.8

between the two pebbles exists. Here, $R_{ij} = \frac{2R_i R_j}{R_i + R_j}$ [m] is the equivalent radius. Thermal contact pairs are included in the computation if $h_{ij} < \varepsilon R_{ij}$, where ε is the cut-off range limit. In this work a value of 0.5 was adopted according to [79] (Yun and Evans, 2010) and [80] (Kanupharti et al., 2008). Batchelor and O'Brien [78] (1977) demonstrated analytically that the heat transport between two spheres mainly occurs across the particle surface closest to the contact region, where the contact region can be either a contact area or a separation gap. It is therein assumed that the heat is transferred through a cylindrical zone of radius $R_{ij}^e = \chi R_{ij}$ [m], as shown in Figure 4–1. The axis of the cylinder is aligned with the centers of the two particles and the effective radius R_{ij}^e is defined as a fraction χ [/] of the equivalent radius R_{ij}. χ gives the fraction of the sphere curvature involved in the heat transport. In literature this parameter is set to match experimental [79] (Yun and Evans, 2010) or numerical [80] (Kanupharti et al., 2008) results carried out by other numerical tools. This parameter strongly

influences the results of the DEM simulation, thus an initial calibration of the code is necessary. The code calibration will be reported in detail in Section 4.2.1.

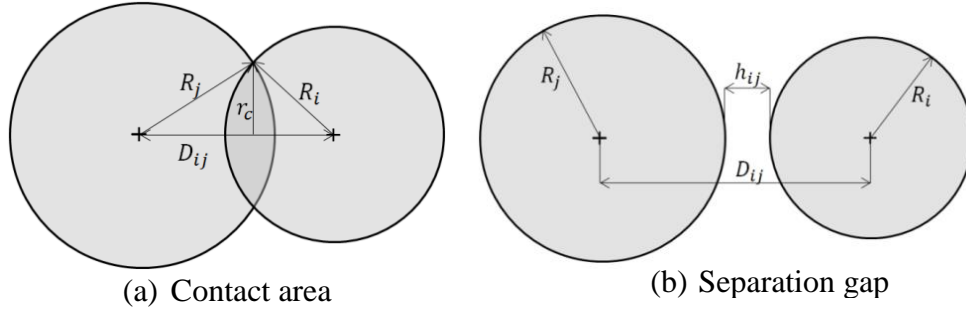(a) Contact area   (b) Separation gap

Figure 4–2: Types of thermal contact regions: a) Contact area for touching particles (overlap type contact), b) Separation gap for particles nearly in contact (gap type thermal contact), [77] (Moscardini et al., 2018).

According to Batchelor and O'Brien [78] (1977) C_i^s, C_j^s and C_{ij}^{ct} are evaluated as:

a. Conductance of the solid particles

$$C_n^s = \pi \, k_s \frac{R_{ij}^{e\,2}}{R_n} \, , n = i \text{ or } j \qquad\qquad 4.9$$

b. Conductance of the thermal contact C_{ij}^{ct}

➤ contact area between touching particles:

$$= \begin{cases} \pi \, k_g R_{ij}\left[\dfrac{2\eta_{ij}}{\pi} - 2\ln\eta_{ij} + \ln\alpha^2\right] & \text{if } \eta_{ij} > 100 \\ \pi \, k_g R_{ij}\left[0.22\,\eta_{ij}^2 - 0.05\eta_{ij}^2 + \ln\alpha^2\right] & \text{if } \eta_{ij} < 1 \\ \pi \, k_g R_{ij}\left\{\left[0.17 + \left(\left(\dfrac{200}{\pi} - 2\ln 100 - 0.17\right) * \dfrac{\eta_{ij}-1}{99}\right)\right] + \ln\alpha^2\right\} & \begin{array}{c}\text{otherwise linear}\\\text{interpolation}\end{array} \end{cases} \quad 4.10$$

➤ separation gap:

$$= \begin{cases} \pi \, k_g R_{ij} \ln\alpha^2 & \text{if } \xi_{ij} < 0.1 \\ \pi \, k_g R_{ij} \ln\left[1 + \dfrac{R_{ij}^{e\,2}}{R_{ij}h_{ij}}\right] & \text{otherwise} \end{cases} \qquad 4.11$$

Here, k_g [W/m K] and $\alpha = k_s/k_g$ [/] are the thermal conductivity of the interstitial gas and the solid to gas thermal conductivity ratio, respectively. $\eta_{ij} = \alpha\, r_c/R_{ij}$ [/] and $\xi_{ij} = \alpha^2\, h_{ij}/R_{ij}$ [/] are two non-dimensional parameters defining the conductance in the contact area and in the separation gap, respectively. The cut-off values for η_{ij} and ξ_{ij} reported in Eqs. 4.10 and 4.11 were estimated according to [78] (Batchelor and O'Brien, 1977). A further and innovative step introduced in this work is the implementation of the influence of the gas pressure, i.e. the Smoluchowski effect, on the heat transfer in a DEM code. To this end the theory of Batchelor and O'Brien [78] (1977), was modified as reported in the following section.

4.1.3 Implementation of the Smoluchowski effect

As previously explained in Chapter 2 - Section 2.1.3, for an unconfined gas the thermal conductivity is independent of its pressure, while it decreases with the pressure when the gas is confined in small gaps. This is the so-called Smoluchowski effect [82], which determines the well-known S-shape curve while plotting the effective conductivity of the packed bed with respect to the gas pressure. The S-shape curve can be divided in three zones: *continuum*, *transition* and *free molecule* regime. The three regimes define the mechanism of the heat transfer as a function of the Knudsen number, thus of the gas pressure (see Chapter 2, Section 2.1.3). In 1969 Kaganer [135] proposed a correlation for the estimation of the thermal conductivity k_g^c of a confined gas as a function of the Knudsen number as

$$k_g^c = \frac{k_g}{1 + 2 \beta K_n},$$
<div align="right">4.12</div>

with

$$K_n = \frac{\Lambda}{L} = \frac{\mathcal{K} T}{\sqrt{2} \pi d_m^2 p L}.$$
<div align="right">4.13</div>

Here, $\mathcal{K} = 1.38 \cdot 10^{-23}$ [J/K] is the Boltzmann constant, T [K] is the temperature, d_m [m] is the kinetic molecule diameter and p [Pa] is the gas pressure. Furthermore, k_g [W/m K] is the bulk thermal conductivity of the interstitial gas and β [/] represents the amount of energy transfer between the gas molecule and the solid material. It depends on the gas type, the solid material and the temperature of the system. Different correlations were proposed for the estimation of β. In this work, the correlation

$$\beta = \frac{2 - \alpha_c}{\alpha_c}.$$
<div align="right">4.14</div>

proposed by Wakao and Kagnei [136] (1982) was used. Here the thermal accommodation coefficient α_c [/] represents the effectiveness of the energy transfer between molecule and wall. It depends on the two phases composing the assembly as well as on the gas temperature. In this work the correlation

$$\alpha_c = \frac{C m_r}{(1 + m_r)^2}$$
<div align="right">4.15</div>

derived by Baule [137] (1914) and later modified by Goodman [138] (1980) was used, where $m_r = m_g/m_s$ [/] is the ratio of the gas (m_g) to solid (m_s) atomic masses [g/mol]. Furthermore, $C = 2.4$ [/] is an empirical constant used by Goodman to better reproduce the experimental results. Eq. 4.15 reduces to the Baule formula for $C = 2$ [/]. The theory of Batchelor and O'Brien [78] (1977), described above, was here modified to implement the Smoluchowski effect. To this end k_g was substituted by k_g^c [W/m K] in Eqs. 4.10, 4.11 and in

the parameter α. This innovative step allows taking into account the reduction of the gas thermal conductivity due to the reduction of the gas pressure. Plugging the Knudsen number, previously defined in Eq. 4.13 as Λ/L, k_g^c becomes
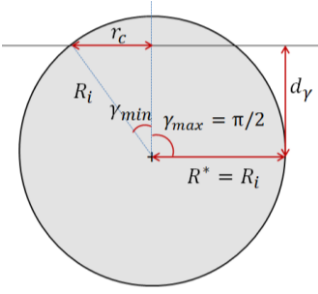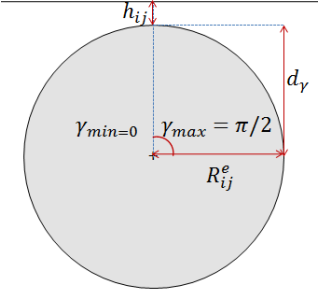
$$k_g^c = \frac{k_g}{1 + 2\,\beta\left(\dfrac{\Lambda}{d_{ave} + h_{ij}}\right)} \qquad 4.16$$

For each contact, the geometrical dimension L is replaced by the mean gap size $d_{ave} + h_{ij}$. When $h_{ij} < 0$, the thermal conductance is evaluated according to Eq. 4.10 (contact area between touching particles) and h_{ij} in Eq. 4.16 is set equal to 0, otherwise, i.e. for $h_{ij} > 0$, Eq. 4.11 (separation gap) is used. The evaluation of d_{ave} is based on the contact configurations reported in Table 4–1 and in Table 4–2.

Table 4–1: Evaluation of the gap size d_{ave} for the two configurations between two spheres, [77] (Moscardini et al., 2018).

Geometrical configuration of the contact	d_{ave}
Two spheres touching at a contact area of radius r_c ($R_i < R_j$)	$\gamma_{min} < \gamma < \gamma_{max}\,; \;\; \theta_{min} < \theta < \theta_{max}$ $\gamma_{max} = \sin^{-1}(R^*/R_i)\,; \;\; \theta_{max} = \sin^{-1}(R^*/R_j)$ $\gamma_{min} = \sin^{-1}(r_c/R_i)\,; \;\; \theta_{min} = \sin^{-1}(r_c/R_j)$ if $R_i < R_{ij}^e$ $R^* = R_i$ otherwise $R^* = R_{ij}^e$ $\bar{d}_\gamma = \dfrac{\int_{\gamma_{min}}^{\gamma_{max}} R_i\,(1-\cos\gamma)\,d\gamma}{\int_{\gamma_{min}}^{\gamma_{max}} d\gamma}$ $\bar{d}_\theta = \dfrac{\int_{\theta_{min}}^{\theta_{max}} R_j\,(1-\cos\theta)\,d\theta}{\int_{\theta_{min}}^{\theta_{max}} d\theta}$ $d_{ave} = \bar{d}_\gamma + \bar{d}_\theta$
separation gap ($R_i < R_j$)	As for the above case of two touching spheres with the exception of the following changes: $0 < \gamma < \gamma_{max}\,; \;\; 0 < \theta < \theta_{max}$ $r_c = 0$ $d_{ave} = \bar{d}_\gamma + \bar{d}_\theta$

Table 4–2: Evaluation of the gap size d_{ave} for the two configurations between sphere- wall, [77] (Moscardini et al., 2018).

Geometrical configuration of the contact	d_{ave}
Sphere - wall with a contact area of radius r_c $(R_j \rightarrow \infty)$	$\gamma_{min} < \gamma < \pi/2$ $\gamma_{min} = \sin^{-1}(r_c/R_i)$ $d_{ave} = \overline{d}_\gamma = \dfrac{\int_{\gamma_{min}}^{\pi/2} R_i \, (1 - \cos\gamma) \, d\gamma}{\int_{\gamma_{min}}^{\pi/2} d\gamma}$ The wall is considered as a sphere with an infinite radius, thus $\overline{d}_\theta$ approaches zero.
Sphere – wall with separation gap $(R_j \rightarrow \infty)$	As for the above case of a spheres touching a wall with the exception of the following changes: $0 < \gamma < \pi/2$ $r_c = 0$ $d_{ave} = \overline{d}_\gamma$

The two tables refer to the particle-particle and the particle-wall contacts, respectively. In the Bachelor and O'Brien theory [78] (1977), the contribution of the gas conduction in the zone nearby the contact area or in the separation gap (h_{ij}), is taken into account in the heat transport. The cylindrical zone, with radius $R_{ij}^e = \chi R_{ij}$, defines the fraction of the sphere curvature involved in the heat transport. Therefore, d_{ave} is the sum of the integrated distances $\overline{d}_\gamma$ and $\overline{d}_\theta$ over the specified portions of the sphere surface.

4.2 Code calibration and validation

In this section, the simulations carried out with the above described KIT thermal-DEM code are presented. In Section 4.2.1, the code calibration is reported. The parameter χ was set to match the experimental results carried out in KIT [108] (Pupeschi et al., 2017). Then, with the selected χ, several simulations were run to validate the code under different system conditions and with different materials. In particular, in Sections 4.2.2, 4.2.3, and 4.2.4 the experimental results obtained in [103] (Enoeda et al., 2001) and [108] (Pupeschi et al., 2017) were simulated varying the gas type, the gas pressure and the compression state, respectively. Finally, in Section 4.2.5 the comparison between numerical and experimental literature results for different solid breeder materials will be reported. The physical characteristics of the

studied solid materials and gases are summarized in Table 4–3 and Table 4–4, respectively. In Table 4–3 the densities of the ceramic materials are given as function of the porosity p_r. The thermal conductivities of the solid and gas materials were evaluated, by means of the correlations reported in Table 4–3 and in Table 4–4, at the investigated temperature of each simulation.

Table 4–3: Physical characteristics of the used solid materials

Material	Parameter		Value
EU Ref. (Li_4SiO_4 + 10 mol% Li_2SiO_3)	k_s	[W/m K]	Correlation fitting values reported in [139] (Löbbecke et al., 2009) for 89% TD (Theoretical Density): $7.317 * 10^{-12}T^4 - 1.302 * 10^{-8}T^3 + 8.712 * 10^{-6}T^2 - 0.002876\,T + 2.62$; T in °C
	c_p	[J/kg K]	$(-5.33 * 10^{-7}T^2 + 0.001925\,T + 1.238) * 1000$ [140] (Knitter, 2017); T in °C
	ρ	[kg/m³]	$2400(1- p_r)$; p_r=0.05
	m_s	[g/mol]	119.85
Li_2TiO_3	k_s	[W/m K]	$[(1 - p)^{2.9}](5.35 - 4.78 * 10^{-3}T + 2.87 * 10^{-6}T^2)$ [141] (Gierszewski, 1998), T in K $[(1 - p)/(1 + (1.06 - 2.88 * 10^{-4}T)p)](4.77 - (5.11 * 10^{-3}T) + (3.12 * 10^{-6}T^2))$ [142] (Saito, 1998); T in K
	c_p	[J/kg K]	$355\,(T - 100)^{1.1}/(1 + (0.3\,T^{1.05}))$ (Gierszewski, 1998), T in K $(0.73 + (8.44 * 10^{-4}T) - (1.67 * 10^{-7}T)) * 1000$ [142] (Saito, 1998); T in K
	ρ	[kg/m³]	$3430\,(1- p_r)$; p_r~0.08
	m_s	[g/mol]	109.76
Li_2ZrO_3	k_s	[W/m K]	$(1 - p)^{5/3}[(3.643/(1 + 0.00155\,T)) + 7.579 * 10^{-10}T^3]$ [143] (Gierszewski, 1993); with T in K
	c_p	[J/kg K]	$(1.022 - (3.696 * 10^{-5}T) - (2.791 * 10^{+4}T^{-2})) * 1000$ [144](Moore, 1989); with T in K
	ρ	[kg/m³]	$4150(1- p_r)$; p_r =0.2
	m_s	[g/mol]	153.1

Table 4–4: Physical characteristics of the used gas types

Material	Parameter		Value
Helium	k_g	[W/mK]	$3.366 * 10^{-3}T^{0.668}$ [99] (Abou-Sena et al., 2005); T in K.
	d_m	[m]	2.15e-10 [145] (Lide, 2004)
	m_g	[g/mol]	4
Air	k_g	[W/mK]	Correlation fitting values reported in [146](http://www.engineeringtoolbox.com) : $-1 * 10^{-11}T^3 - 4 * 10^{-8}T^2 + 8 * 10^{-5}T + 0.0241$; T in °C
	d_m	[m]	3.66e-10 [145] (Lide, 2004)
	m_g	[g/mol]	28.96

With application to breeder beds, several experimental campaigns have been carried out to characterize the thermal properties of the various ceramic breeder material candidates. In literature different correlations for the estimation of k_g and c_p for the same breeding material are reported [99] (Abou-Sena et al., 2005). In the present work, the influence of the thermal conductivity of the solid material on the effective thermal conductivity was investigated. For the EU Ref. the most recent and reliable thermal conductivity values were considered [139] (Löbbecke et al., 2009). They refer to a porosity of ~11%, while the pebbles used in the experiments [108] (Pupeschi et al., 2017) have a porosity of around 6%.

In Section 4.2.5 the investigation of the two other solid breeder materials Li_2TiO_3 and Li_2ZrO_3 is reported. The simulations with Li_2TiO_3 pebbles were carried out implementing the correlations reported in [141] (Gierszewski, 1998) and [142] (Saito, 1998). In the present work both monosized and polydispersed assemblies were studied. In Figure 4–3, the pebble size distribution used in the experiments carried out in KIT [108] (Pupeschi et al., 2017) is reported together with the produced assembly used for the numerical simulations. All assemblies consist of 5000 perfectly spherical particles packed in virtual box using the Random Close Packing (RCP) algorithm described before. The height of the assemblies was set to 20 mm while the dimension of the square cross section of the assemblies was evaluated as a function of pebble size and packing factor as $l^2 = \frac{V_{tot,s}}{H*PF}$. Here, $V_{tot,s}$ and H are the total volume of the spheres and the height of the assembly, respectively.
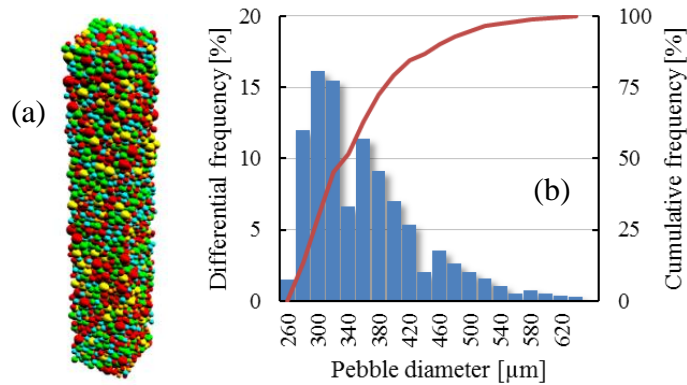
Figure 4–3: (a) Assembly generated with the size distribution showed in (b) of the EU Ref. [108] (Pupeschi et al., 2017), different colours represent different pebble size, [77] (Moscardini et al., 2018).

In Section 4.2.1, 4.2.2, 4.2.3 and 4.2.4 when the compression state is not specified, the reported results are the average value between uncompressed and compressed bed at 6 MPa in agreement with the experimental results reported in [108] (Pupeschi et al., 2017). This is justified by the small variation of the effective thermal conductivity with the compression

observed in [108] (Pupeschi et al., 2017) and in the numerical results discussed in Section 4.2.4. In the Section 4.2.5 uncompressed beds were used. Furthermore, in [108] (Pupeschi et al., 2017) a mechanical conditioning of three loading/unloading cycles up to 6 MPa was applied to obtain a well-defined mechanical state of the bed, while for the simulation the second loading cycle was considered representative of a consolidated bed. Indeed, considering the first four compressive loading-unloading cycles of the DEM simulation reported in Figure 4–4, a large residual strain is observed after the first unloading, while in the consecutive cycles the additional compaction of the bed is strongly reduced. For all assemblies, the uncompressed configuration refers to a very low compression level of about 20KPa. Due to the pure geometric method adopted to generate the assemblies by the RCP, few contacts among particles initially exist. Therefore, to increase the number of contacts bringing the starting configuration closer to real conditions, the slight compression of 20 KPa is needed.
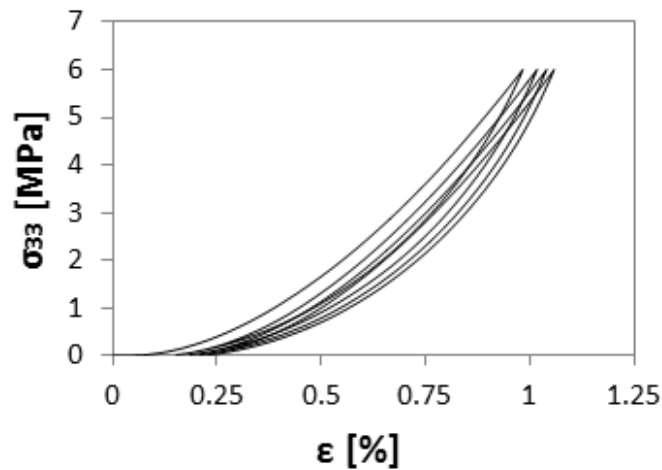
Figure 4–4: Uniaxial compression loading cycles, [77] (Moscardini et al., 2018).

4.2.1 Influence of χ parameter and code calibration

The parameter χ influences the value of the effective thermal conductivity since it determines the effective radius of the cylindrical zone involved in the heat transfer (Figure 4–1). In literature, χ is chosen to match experimental or analytical results. In Figure 4–5 the comparison between experimental and numerical results varying χ is shown, where χ was varied in the range 0.6-0.8 to study its influence on the bed's thermal conductivity. Numerical simulations and experiments were carried out with pebbles of EU Ref. in helium at ~64.2% packing factor with the polydispersed size distribution presented in Figure 4–3. As shown in the figure, the effective thermal conductivity decreases with decreasing χ according to the reduction of the fraction of the sphere surface considered for the heat transport. Nevertheless, the variation of χ does not change significantly the trend of the effective thermal conductivity vs. the temperature, shifting the curve to higher or lower values with the reduction or increase

of χ, respectively. For a given χ value, the temperature-dependent behavior is brought from the value of k_s and k_g^c at the investigated temperature, quantitatively matching the experimental results of the effective thermal conductivity without additional fitting. In this work a value of 0.71 was used to match the experimental results performed in KIT [108] (Pupeschi et al., 2017). Note that in the present study χ is set only once in order to calibrate the code and then kept fixed for all the other simulations (e.g. different solid materials, gas pressures/type and compression state). The choice of χ may differ for systems with differently sized particles, however due to the limited available data, χ=0.71 was used in this work for a size range from 0.25 to 1.9 mm, corresponding to experimental data from various sources [105] (Hall and Martin, 1981), [108] (Pupeschi et al., 2017) and [112] (Lorenzetto et al., 1995), which is the relevant size range in fusion applications.
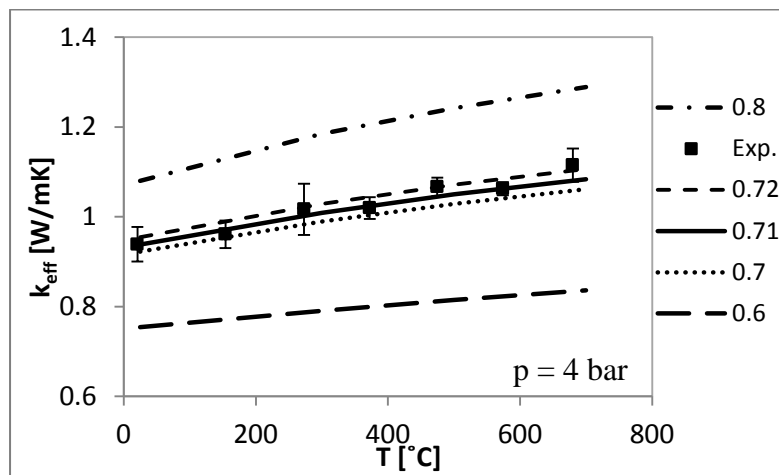
Figure 4–5: Influence of the χ parameter on the effective thermal conductivity (polydispersed assembly of EU Ref. in helium) and comparison with experimental results carried out in [108] (Pupeschi et al., 2017). [77] (Moscardini et al., 2018).

4.2.2 Influence of the gas type

In this section the influence of the gas type on the effective thermal conductivity was numerically investigated. Numerical simulations were carried out with the above mentioned polydispersed assembly of EU Ref. in helium and air at 4 bar. The investigated temperature range between room temperature and 700 °C is consistent with the expected operating temperature range of the ceramic breeder material and the experiments conducted in [108] (Pupeschi et al., 2017).

In Figure 4–6 the comparison between numerical and experimental results is shown. A good agreement with the experimental outcomes is observed. The DEM simulations accurately capture the different thermal behavior of the granular assembly in helium and air. An increase of the effective thermal conductivity with the temperature was found for all

investigated compositions in both atmospheres in agreement with experimental observations. As experimentally observed, a pebble bed in air shows a reduction of the effective thermal conductivity of about 45-55% compared to simulation for helium. This difference is determined by the different thermal conductivities of the two gases. In particular, in the considered temperature range, the thermal conductivity of unconfined helium is about five times higher than the thermal conductivity of unconfined air.
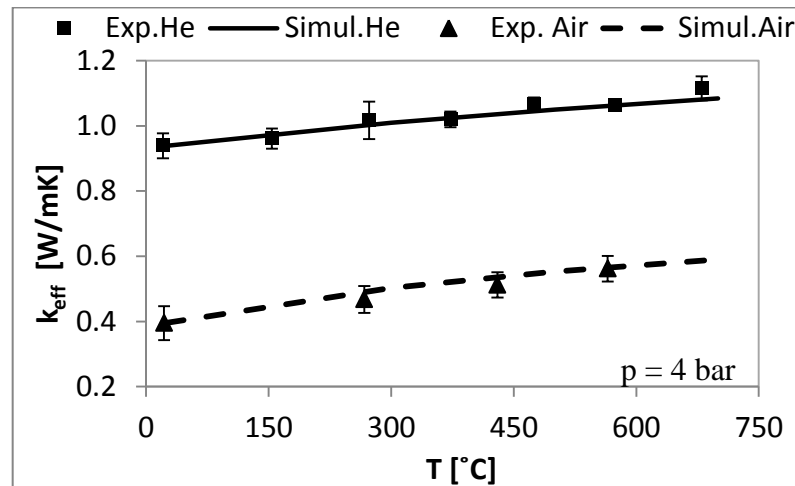
Figure 4–6: Comparison between numerical and experimental results [108] v for polydispersed assembly of EU Ref. pebbles in air and He. [77] (Moscardini et al., 2018).

4.2.3 Influence of the gas pressure

In this section, the influence of the gas pressure on the effective thermal conductivity of pebble beds is analyzed. Simulations were carried out with the above mentioned polydispersed assembly of EU Ref. In Figure 4–7, the comparison between numerical simulations and experimental results reported in [108] (Pupeschi et al., 2017) is shown.
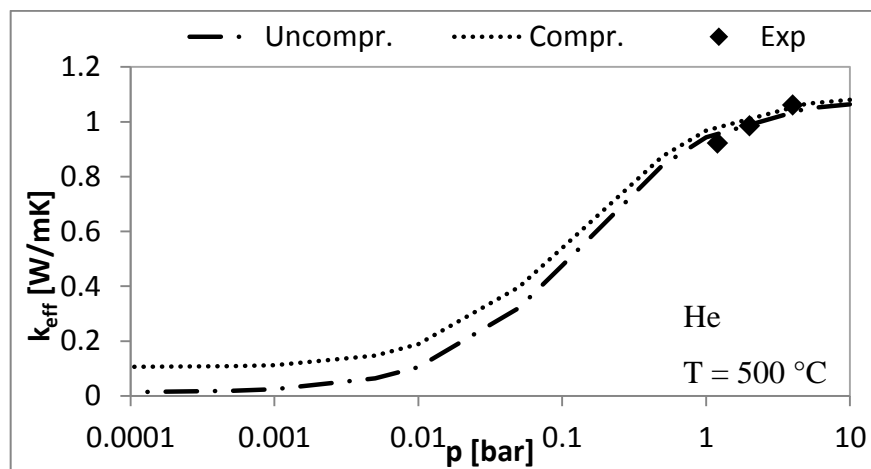
Figure 4–7: Influence of the pressure for different compression states. Comparison between numerical [77] (Moscardini et al., 2018) and experimental results [108] (Pupeschi et al., 2017).

The experimental results refer to the average value between compressed and uncompressed bed of EU Ref. in helium at 1.2, 2 and 4 bar as expressed by the correlations reported in [108] (Pupeschi et al., 2017). In the simulation the gas pressure was varied in the range 0.0001 to 10 bar to cover all the gas regimes. Moreover, the simulation results are shown for compressed (6 MPa) and uncompressed beds to show the influence of the compressive state at different gas pressure. The S-shape curve characteristic of the Smoluchowski effect is reproduced, meaning that the continuum, transition and free molecule gas regimes are numerically obtained. In the pressure range between 1 and 4 bar, a good agreement with experimental outcomes was found. In this pressure range, both theoretical (according to Eqs. 4.12 and 4.13) and experimental results show an increase of the effective thermal conductivity of the bed with the gas pressure. The effective thermal conductivity increases up to ~5 bar, then an asymptotic pressure dependence is observed. This indicates that, in the range 1-5 bar, the filling gas is in the upper part of the transition region. The influence of the compressive load was found to be more pronounced at very low pressures (free molecule regime) decreasing with the increase of the pressure in the transition regime to almost vanishing difference in the continuum regime where the breeder beds are supposed to operate. The influence of the compressive load is more evident at very low pressures where the heat transfer mainly occurs through touching particles, while the contribution of the gas is negligible. At high pressure, due to the small value of the ratio k_s/k_g (~20 for unconfined helium at room temperature) of the analyzed breeder bed, the heat is mainly transferred by the gas, thus even if contact areas increase under the compression load, negligible variations are detected. The DEM results are compared with literature data in Figure 4–8. The results reported in [103] (Enoeda et al., 2001) cover the low gas pressure range down to 0.0001 MPa, while in [102] (Dalle Donne, 2000) experiments were conducted in the pressure range 0.1-0.3 MPa. The figure is reproduced from [103] (Enoeda et al., 2001) where the experimental results were also compared with the correlations derived by Bauer and Schlünder (SBZ) [104] (1978) and Hall and Martin (HM) [105] (1981). The numerical values obtained in this study are overlaid as a solid red line. Both numerical and experimental results show a strong influence of the filling gas pressure in the pressure range 0.0001-0.1 MPa. The dependence on the helium pressure is drastically reduced, although still present, for pressures above 0.1 MPa. In contrast to the outcomes of [103] (Enoeda et al., 2001) and of the present study, no influence of the helium pressure on the thermal conductivity of the pebble bed is found in [102] (Dalle Donne, 2000). For a pressure above 0.05 MPa, the numerical results are in good agreement with the experimental values obtained in [103] (Enoeda et al., 2001). The observed difference between

the experimental and simulation values is less than 10%. Lower thermal conductivity values, especially between numerical simulations and experiments, were numerically obtained at lower gas pressures. Thermal radiation is not implemented in the present numerical model. Accounting for thermal radiation, the effective thermal conductivity values are expected to slightly increase in the low pressures region where radiation is the predominant heat transfer mechanism. A good agreement between numerical and HM analytical results is obtained in the studied pressure range while, the SZB model gives higher values. In Figure 4–9 and Figure 4–10 the influence of gas type and temperature on the bed effective thermal conductivity as a function of the gas pressure is shown, respectively. The simulations were carried out for an uncompressed bed. The effective thermal conductivities presented in these figures are normalized with respect to the effective thermal conductivity of the unconfined gas. For a given gas type and temperature, the thermal conductivity decreases with decreasing pressure showing the characteristic S-shaped curve. Compared to helium atmosphere, the onset of the transition regime is shifted to lower pressures in air.
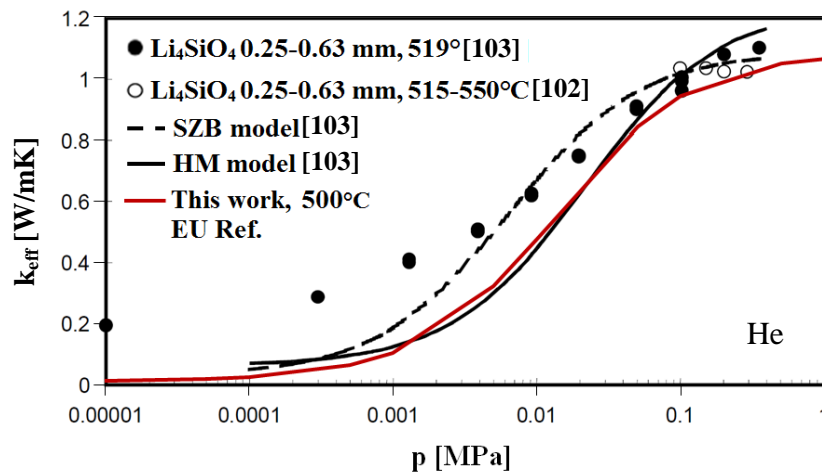
Figure 4–8: S-shape curves. Comparison between literature values and DEM results obtained in this work. After [103] (Enoeda et al., 2001) and [77] (Moscardini et al., 2018).
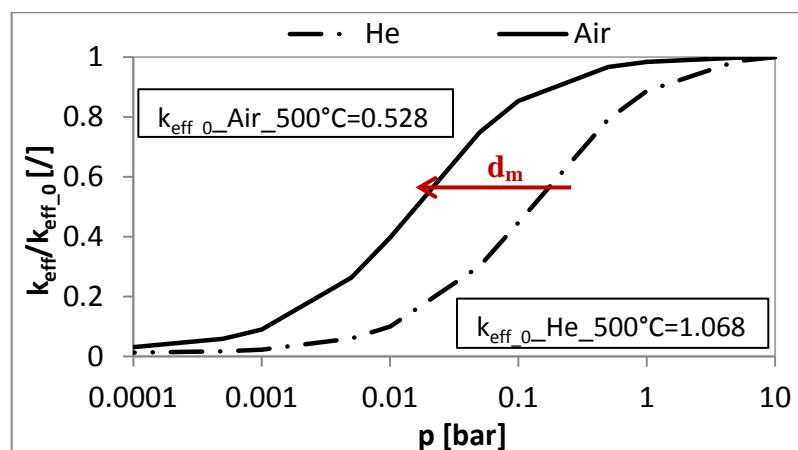
Figure 4–9: Numerical results for polydispersed assembly in He and air normalized on unconfined values of thermal conductivity k_{eff_0}, [77] (Moscardini et al., 2018).

93
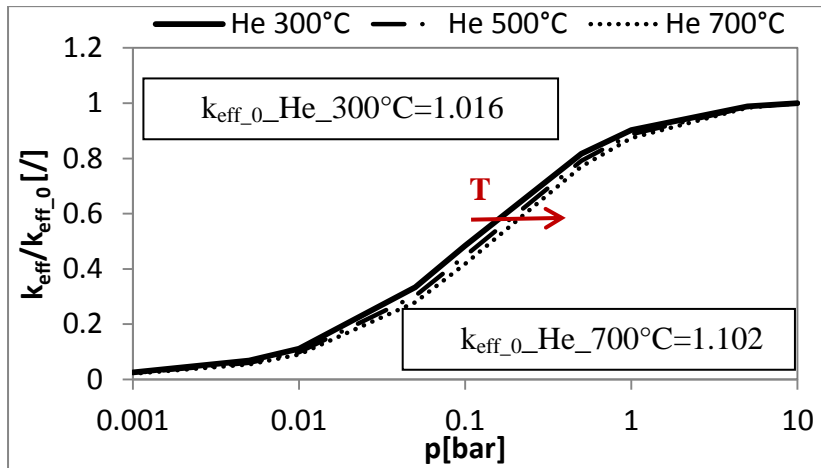
Figure 4–10: Numerical results for polydispersed assembly in He at 300, 500 and 700˚C normalized on unconfined values of thermal conductivity k_{eff_0}, [77] (Moscardini et al., 2018).

According to Eq. 4.13, in the transition regime, both a lower kinetic diameter and a higher temperature result in a larger mean free path leading to a reduction of the gas contribution to the effective conductivity of the bed. The onset of the transition region is then shifted to lower pressures when the filling gas is characterized by a higher kinetic diameter d_m and when the bed temperature decreases, respectively.

4.2.4 Influence of the compressive load

The solid to gas thermal conductivity ratio k_s/k_g affects the heat transfer in the bed. In pebble beds with comparably low k_s/k_g (e.g. in the order of 10 for ceramic breeder pebble beds) the heat flux is uniformly distributed among the solid and the gas phases, while in beds with a high ratio the heat flows mainly through pebbles and contact areas between particles, since these are the paths of higher thermal conductivity. Therefore, the effective thermal conductivity of beds with high k_s/k_g ratios (e.g. in the order of 1000 for the neutron multiplier pebble beds) is influenced by the bed deformation. In particular, a compressive load acting on a breeder bed results in an increase of both the number of the contacts between pebbles and the contact area dimension of existing contacts. In Figure 4–11, the numerical results on the effect of bed compression are compared with experimental results in [108] (Pupeschi et al., 2017). The numerical results refer to the above mentioned polydispersed assembly of EU Ref. in helium and air at 4 bar in the temperature range of 25 to 700ºC for a compressed and an uncompressed state. In helium, a good agreement with experimental values was obtained. The numerical results in air slightly underestimate or overestimate the experiments for the uncompressed and compressed states, respectively. However, considering the experimental uncertainty, a fairly good agreement with the experimental values was found also in air. An increase of the effective thermal conductivity with the applied compressive

load was observed in both atmospheres. The influence of the compressive load was found to be more pronounced in air consistent with the higher k_s/k_g ratio than in helium, since the thermal conductivity of air is 5 times lower than that of helium. The increase of the thermal conductivity due to the compressive load was found to be more expressed at low temperatures with the tendency to vanish at high temperatures according to the decrease of the k_s/k_g ratio with the temperature.
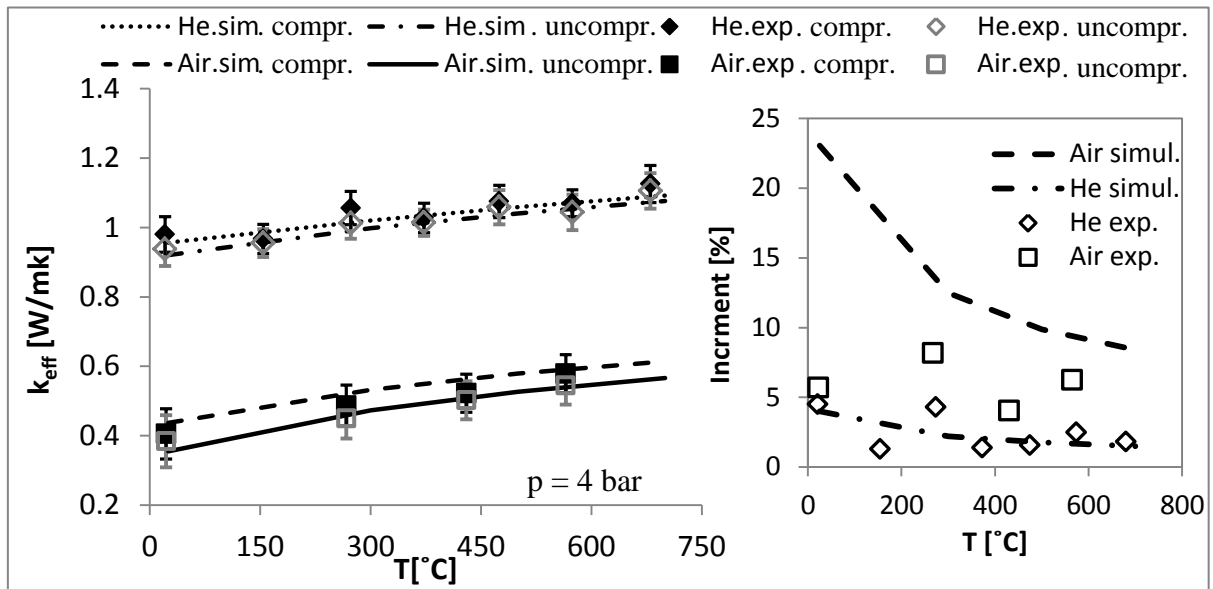

Figure 4–11: Influence of the compressive load on the effective thermal conductivity for polydispersed assembly of EU Ref. pebbles in air and He, [77] (Moscardini et al., 2018).

4.2.5 Influence of the solid material

In order to further validate the KIT thermal-DEM code, experimental works reported in literature and referring to other breeding materials were numerically investigated. In particular, the effective thermal conductivity of Li_2TiO_3 and Li_2ZrO_3 pebble beds were studied. In Figure 4–12 the numerical and experimental results reported in [112] (Lorenzetto et al., 1995) for Li_2ZrO_3 beds are compared to simulations. In [112] (Lorenzetto et al., 1995) Li_2ZrO_3 pebbles with a diameter of 1.2 mm at 63% packing fraction were investigated in helium atmosphere at 1 bar. The simulations were run with the same pebble size, packing state, gas type and pressure as used in the experiment [112] (Lorenzetto et al., 1995). The physical properties of Li_2ZrO_3 used in the simulation are reported in Table 4–3. As shown in the figure, the experimental results were reproduced. In particular, the nonlinear trend obtained in [112] (Lorenzetto et al., 1995) was numerically obtained. In Figure 4–13 the comparison between experimental [114] and numerical results for Li_2TiO_3 pebbles is shown. In this figure, the experimental results are presented by diamonds while the simulations are plotted by solid and dashed lines. As indicated in Table 4–3, the simulations were carried out

with the thermal properties k_g and c_p reported in [141] (Gierszewski, 1998) and additionally with the k_g and c_p values found in [142] (Saito, 1998), respectively. In [114] (Hatano et al., 2003) the thermal conductivity of Li_2TiO_3 pebble beds in helium gas at 1 bar was presented over the temperature range 400-800°C. The experiments were carried out with 1.91 mm pebbles at 60% packing fraction. The same conditions were used to run the simulations. Due to the scattering of the experimental results, both correlations used to estimate the thermal properties of the solid material give reasonable agreement when simulating the thermal conductivity of Li_2TiO_3 beds. It is obvious from this graph that the correlations implemented to define the thermal properties of the solid material play a major role in the evaluation of the effective thermal conductivity of the bed. Nevertheless, a good agreement between numerical and experimental results was obtained.
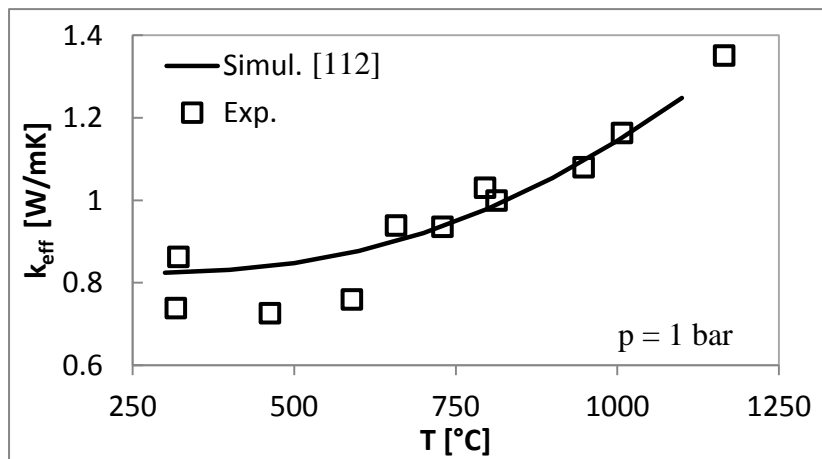
Figure 4–12: Comparison between numerical simulation and experimental results (Lorenzetto et al., 1995) [112] for Li_2ZrO_3 pebbles in helium atmosphere, [77] (Moscardini et al., 2018).
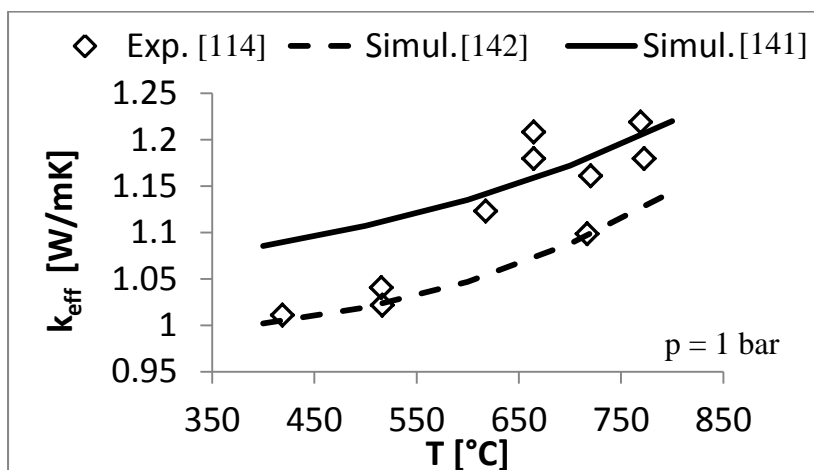
Figure 4–13: Comparison between numerical simulations with thermal properties reported in [141] (Gierszewski, 1998) and [142] (Saito et al., 1998) and experimental results according to [114] (Hatano et al., 2003) for Li_2TiO_3 pebbles in helium atmosphere, [77] (Moscardini et al., 2018).

Chapter 5
Thermal-DEM code application to the breeder zone

In the previous chapter, an innovative in-house thermal-DEM code, developed to estimate the heat transfer in packed beds, was presented. Through a comparison with experimental results reported in literature, the code was validated and the effective thermal conductivity of the ceramic breeder pebble beds as a function of several parameters was successfully predicted. For the work reported in this chapter, the code was slightly modified to evaluate the temperature profile generated in the ceramic breeder pebble beds from neutronic heating applied as internal heat source. The breeder zone of the HCPB blanket for DEMO was considered as the reference model implementing the same materials, applying the operating loads and simulating relevant bed's thicknesses. The variation of the thermal conductivity of the gas and solid material with the temperature at the contact pair level was taken into account. In the first section, the modified method is presented and the boundary and loading conditions are described. In the second section, the temperature profile generated inside the breeder bed from the neutronic heating is shown and sensitivity studies are reported and discussed.

5.1 Modified thermal-DEM code accounting for the neutronic heating as internal heat source.

To evaluate the temperature field generated in the ceramic breeder pebble beds from neutronic heating, the thermal-DEM code presented in the previous chapter was slightly modified. Assemblies of monosized and polydispersed pebbles have been generated according to the method described in the Section 4.1.1. Particles are highly packed inside a box with a given height defined by an upper and a bottom wall, while the condition of periodicity was applied at the lateral sides which dimensions are determined as a function of the target packing factor. The assemblies are then heated up applying the neutronic heating as internal heat source. The heat q_{ij} transferred between two particles i and j is evaluated according to the Eq. 4.1 at each time step for each contact in the whole assembly. Eq. 4.2 was modified to evaluate the rate of temperature change $\dot{T}_i$ of the i-th pebble accounting for the heat generation due to neutronic heating:

$$\dot{T}_i = \frac{1}{m_i \, c_p} \left(\sum_j q_{ij} + \Psi V_i \right).$$ 5.1

Compared to Eq 4.2 the term $\Psi_i V_i$ was added. Here, Ψ [W/m^3] and V_i [m^3] are the power density due to the neutronic heating and the volume of the particle "i" ($V_i = \frac{4}{3} \pi r_i^3$), respectively. The values of Ψ will be reported in the next section. The upper and bottom wall are set to a constant temperature (blanket relevant) resembling the cooling structures of the breeder beds (details are reported in the next section), while adiabatic conditions were applied to the lateral sides as described in Chapter 4. The thermal diffusion time δt (see Eq. 4.4) as well as the condition to end the simulation (see Eq. 4.3) were not modified.

The thermal resistor applied to evaluate the heat transfer in the individual thermal contact is the same as described in Section 4.1.2. Due to the large temperature gradient expected to be generated in the bed's thickness from the neutronic heating, the temperature dependent thermal conductivity of both solid material and gas were here implemented. In Eq. 4.9, k_s [W/m K] is replaced by $k_{s,i}$ [W/m K]. Here, $k_{s,i}$ is the thermal conductivity of the solid material evaluated for each individual particle at its related temperature. Likewise, the thermal conductivity of the gas k_g [W/m K] was replaced with $k_{g,ij}$ [W/m K], which is updated according to the temperature acting in the individual contact pair (Section 4.1.2). In particular, $k_{g,ij}$ [W/m K] is calculated at the average temperature of the two particles involved in the thermal contact. $\alpha = k_s / k_g^c$ [/] was replaced by $\alpha_{ij} = k_{s,ij} / k_{g,ij}^c$ [/], where $k_{s,ij}$ [W/m K] is the thermal conductivity of the solid material evaluated as the average of the thermal conductivities of the two particles in contact, while $k_{g,ij}^c$ is obtained by Eq 4.12 substituting k_g with $k_{g,ij}$. Finally, to adapt the implementation of the Smoluchowski effect for the evaluation of the heat transfer in a granular material with an internal heat source, the Knudsen number becomes

$$K_n = \frac{\Lambda}{L} = \frac{\mathcal{K} \, T_{ave}}{\sqrt{2} \, \pi \, d_m^2 \, P \, L},$$

5.2

where, compared to Eq.4.13, T_{ave} [K] replaces T [K] with T_{ave} as the average temperature of the two particles in contact.

5.1.1 Boundary conditions and thermal properties

As starting condition, the temperature of the particles composing the bed as well as the temperature of the upper and bottom wall is set to 500 °C. This temperature was selected according to the thermal analysis reported in [147], [148] (Hernández et al., 2011; Hernández et al., 2017). During the simulations, the temperature of the walls is kept constant to simulate

the cooling of the bed provided by helium flowing into the cooling plates of the HCPB breeding blanket [147], [148] (Hernández et al., 2011; Hernández et al., 2017). The temperature of the particles will increase according to the applied power density of the neutronic heating. Figure 5–1 shows the power density generated from the neutronic heating acting on the solid material Li_4SiO_4 as a function of the radial distance from the first wall. This data refers to the neutronic calculations presented in [149] (Hernández et al., 2016) and in [150] (Pereslavtsev et al., 2017) for an outboard blanket (OB) with Li_4SiO_4.
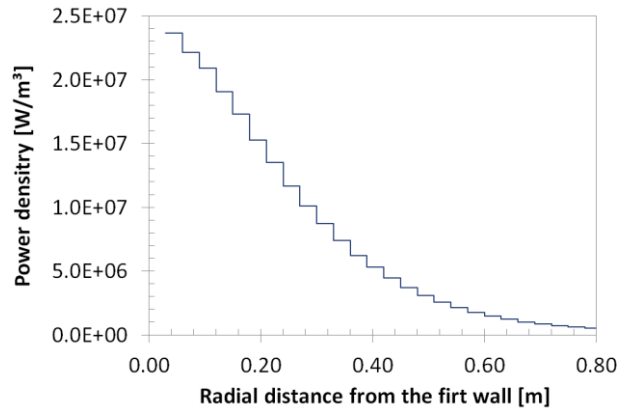
Figure 5–1: Neutronic power density for Li_4SiO_4 in OB blanket as a function of the radial distance from the first wall, after [149]-[150] (Hernández et al., 2016; Pereslavtsev et al., 2017).

When different conditions are not specified, the standard conditions refer to assemblies of 5000 polydispersed spheres (see Figure 4–3(b)) of EU Ref. material at 95% theoretical density (typical value of the EU Ref. produced pebbles [7] (Shikama et al., 2008)) at a packing factor of ~64%. A gas pressure of 2 bar was chosen as standard condition according to [148] (Hernández et al., 2017) and [149] (Hernández et al., 2016), where the helium purge gas pressure was reduced from 4 to 2 bar in favor of a reduction of the tritium permeation into the cooling plates. Indeed, the driving force behind the tritium permeation in the cooling plates and thus in the coolant fluid is the tritium partial pressure [151] (Hanchar et al., 1982), which depends on the pressure of the purge gas. In particular, when the pressure of the purge gas decreases the tritium partial pressure reduces determining a lower diffusion of tritium into the cooling plates. In view of this, the purge gas pressure is a key parameter to decrease the amount of tritium in the coolant and in the structural materials guaranteeing a high level of safety. Since the design of the DEMO HCPB blanket is constantly updated and not yet finalized [148] (Hernández et al., 2017) and [149] (Hernández et al., 2016), a bed thickness of 15mm is here taken as representative.

As the assemblies are generated under a periodic configuration for the lateral sides, the radial and toroidal heat transfer is neglected. The simulated assembly represents a column

cutout of the breeder bed bounded by the cooling plates at top and bottom. This simple geometry allows evaluating the temperature profile in the thickness of the breeder bed, where the temperature variation is more significant than in the other directions due to the small ratio between the bed thickness and the radial/toroidal extension. However, neglecting the heat exchange in the radial and toroidal direction, the predicted temperature is overestimated. For the simplified geometry, a constant power density (Ψ in the Eq.5.1) referring to the investigated radial distance from the first wall is applied to the individual pebbles of the assembly (multiplying Ψ by the volume V_i as reported in the Eq.5.1). For the reasons explained in the previous chapter (Section 4.2), a slight compression until 20 KPa is necessary to bring the starting configuration of the analyzed assembly closer to real conditions.

Li_2TiO_3, Li_2ZrO_3, LiO_2 and Li_4SiO_4 were considered as solid breeder materials to investigate their influence on the temperature profile of the bed. Figure 5–2 shows the thermal conductivity of Li_2ZrO_3, EU Ref., Li_2TiO_3 and LiO_2 evaluated as a function of the temperature according to the correlation reported in [112], [139], [142] and [152], respectively.
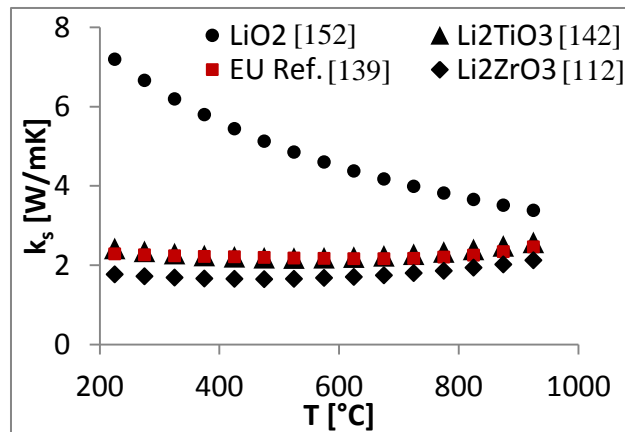
Figure 5–2: Thermal conductivity of the solid materials vs. temperature. Values obtained with correlations of [112] (Lorenzetto et al., 1995), [139] (Löbbecke et al., 2009), [142] (Saito et al., 1998) and [152] (Krikorian, 1985).

The values refer to a porosity of 11%, which is the minimum percentage reached in the sintered pellets of EU Ref. (Li_4SiO_4 + 10 mol. % of Li_2SiO_3) [139] (Löbbecke et al., 2009). Since results observed in this chapter are related to steady state conditions, which are not influenced by the heat capacity, c_p is kept constant at the value assumed at the starting temperature of 500 °C. The effective density and molecular mass are reported in Table 4–3 and Table 5–1. While for the Li_2ZrO_3, LiO_2 and Li_2TiO_3 the correlations reported in literature and obtained from different experimental campaigns give similar thermal conductivities, large deviations occur for Li_4SiO_4 between different studies. Therefore, three curves representing the thermal conductivities of Li_4SiO_4 (11% of porosity) are compared in Figure 5–3. The

related correlations are reported in Table 4–3 and Table 5–1. For the filling gas the implemented thermal properties are reported in Table 4–4.
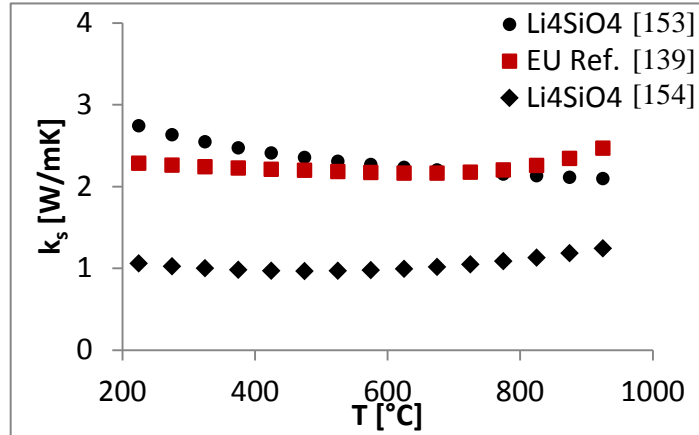
Figure 5–3: Thermal conductivity of Li_4SiO_4 vs. temperature. Values obtained with correlations of [139] (Löbbecke et al., 2009), [153] (Billone et al. , 1993) and [154] (http://www-ferp.ucsd.edu/LIB/PROPS/PANOS/li4sio4.html).

Table 5–1: Physical characteristics of the solid materials

Material	Parameter	Value
LiO_2	k_s [W/m K]	$[(1-p_r)^{1.94}](0.022 + 1.784*10^{-4}\,T)^{-1}$; T[K] [152] (Krikorian, 1985)
	c_p [J/kg K]	$(2.5179 + (3.328*10^{-4}\,T) - (8.382*10^4/T^2))*1000$; T[K] [152] (Krikorian, 1985)
	ρ [kg/m³]	2013(1- p_r)
	m_s [g/mol]	29.8814
Li_4SiO_4	k_s [W/m K]	$2.49\,(1-p_r)^{5/3}[(1 + 2.064*10^{-3}\,T)^{-1} + (1.85*10^{-10}\,T^3)]$; T[K] [153] (Billone et al. , 1993)
	c_p [J/kg K]	$(0.890 + (1.46*10^{-3}\,T) + (4.01*10^3*T^{-2}))*1000$; T[K] [153] (Billone et al. , 1993)
	ρ [kg/m³]	2400(1- p_r)
	m_s [g/mol]	119.85
Li_4SiO_4	k_s [W/m K]	$1.98 + \left(\frac{850}{T}\right)*\{(1-p_r)/[1 + \left(p_r\left(2.14 - (7*10^4*T)\right)\right)]\}$; T[K] [154] (http://www-ferp.ucsd.edu/LIB/PROPS/PANOS/li4sio4.html.)
	c_p [J/kg K]	$939.9 + (1.4577*T) - (4.011*10^7/T^2)$; T[K] [154] (http://www-ferp.ucsd.edu/LIB/PROPS/PANOS/li4sio4.html.)
	ρ [kg/m³]	2400(1- p_r)
	m_s [g/mol]	119.85

5.2 Temperature profile in the breeder zone

In this section the temperature profile generated by neutronic heating along the thickness of the breeder bed of the DEMO HCPB blanket is evaluated. Starting from the simplified geometry described in the previous section and relevant conditions for a breeder pebble bed, different neutronic power densities were applied to resemble different radial positions of the bed. Afterwards, parametric sensitivity studies were carried out varying the bed thickness, the

filling gas type, the gas pressure, the solid breeder material and the packing factor. Then, the effect of the mechanical cycling load until the 30th cycle is studied in order to evaluate the influence of the bed compaction on the temperature field of the bed. Finally the influence of the particles' size is investigated.

5.2.1 Influence of the neutronic power density

Figure 5–4 shows the temperature profiles generated across the bed's thickness for an OB HCPB breeding blanket with the conditions described in Section 5.1.1. The curves are generated dividing the assembly in 70 layers along the thickness and plotting the average temperature of the particles falling into the same layer at the center plane height of the layer. The different curves refer to different radial distances from the first wall. The radial distances correspond to a range from 50 to 450 mm resembling the radial extension of the breeder zone in the HCPB [147], [148] (Hernández et al., 2011; Hernández et al., 2017). A certain radial distance corresponds to a respective neutronic power density inside the solid breeder material. When the radial distance from the first wall increases, the neutronic power density decreases according to the plot shown in Figure 5–1. This generates the highest temperatures in the zone nearest to the first wall. Figure 5–5 exemplarily shows the obtained temperature field for different radial distances from the first wall. According to results shown in Figure 5–4 and Figure 5–5, the temperature field strongly changes with the radial position. The peak temperature of about 907°C is reached at the minimum distance of 50 mm considered in this study. This temperature is lower than the design limit of 920 °C, which is based on avoiding sintering of pebbles [155] (Hernández et al., 2012). Increasing the radial distance, the bed temperature strongly decreases reaching a maximum temperature lower than 580°C at 450 mm from the FW. This affects the Tritium Residence Time (TRT), which is one of the important targets of the breeder blanket. Indeed, the TRT strongly depends on the operating temperature of the breeder beds. Higher temperatures lead to a lower TRT, which is essential to minimize the tritium inventory inside the breeder zone avoiding a large tritium release in case of an accident. Therefore, even if the minimum temperature to avoid very low tritium diffusion is around 400°C, higher temperatures (but lower than the design limits) are aimed at to guarantee the minimum allowable TRT.

The temperature profile generated in the breeder thickness of the HCPB blanket has been also reproduced by means of an analytical approach considering the bed as a continuum with effective thermal properties. The adopted method as well as the comparison between analytical and numerical DEM results are reported in the Appendix A.
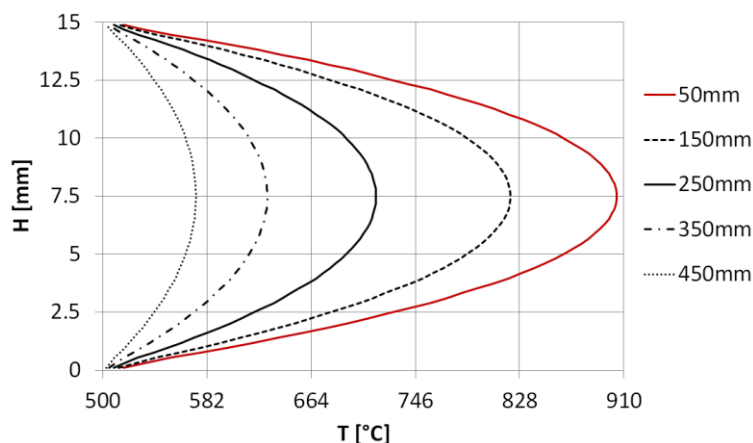
Figure 5–4: Temperature profiles generated in the thickness of the breeder material at different radial distances from the first wall according to the nuclear heating reported in Figure 5–1.
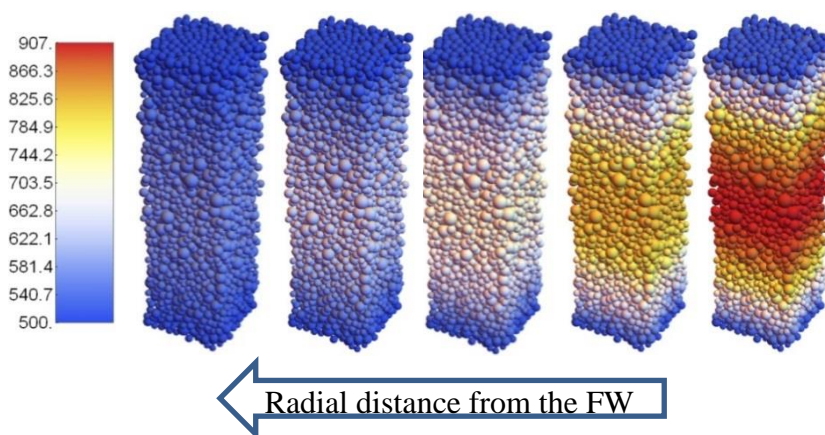

Figure 5–5: Temperature field predicted at several distances from the first wall (~50, 150, 250, 350 and 450 mm) according to the nuclear heating reported in Figure 5–1.

5.2.2 Influence of bed thickness

In the past ten years, variations of the breeder bed thickness were proposed to optimize the temperature field in the breeder beds assuring an acceptable Tritium Breeding Ratio (TBR), tritium extraction and to guarantee the fulfillment of the temperature design limits [149] (Hernández et al., 2016). Starting from the standard conditions reported in Section 5.1.1, thicknesses of 10, 15 and 20mm were simulated to investigate the influence of the bed height on the temperature profile. In Figure 5–6, the obtained temperature profiles are compared. Results are plotted as a function of the normalized thickness and refer to a radial distance from the first wall of ~50 mm. As it has to be expected, due to the longer transport path, a larger bed thickness exhibits a higher peak temperature under the same imposed neutronic power density. For a thickness of 20mm, the maximum temperature overcomes the allowable limit by about 245 ℃, while in a 10 mm bed, the predicted maximum temperature is about 240 ℃ below the allowable limit for the ceramic breeder material. This suggests that larger

bed thicknesses are more suitable for zones with a lower neutronic power density and vice versa. Adjusting the thickness of the bed as a function of the neutronic power density, and thus of the radial distance from the plasma, a higher average temperature could be reached in the whole bed in favor of a lower TRT.
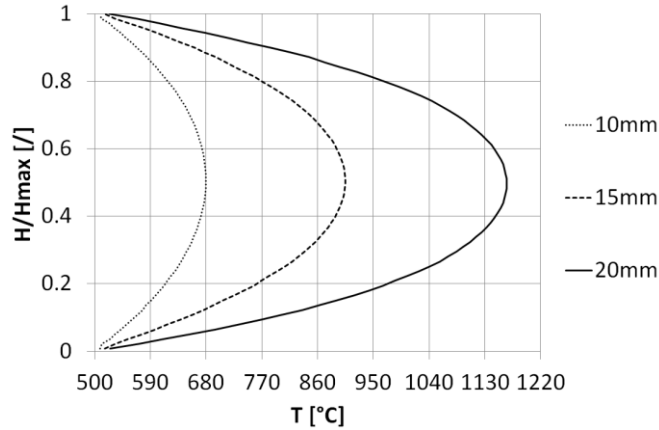
Figure 5–6: Temperature profiles generated inside an OB blanket at ~50mm from the FW for three different bed thicknesses: 10, 15 and 20mm.

5.2.3 Influence of the packing factor

Figure 5–7 shows the temperature profiles generated along the thickness of the breeder bed under standard conditions (see Section 5.1.1) at ~50mm from the first wall and for different packing factors. Packing factors of about 62.5, 63, 64 and 65% were investigated. Increasing the packing factor means a proportional increase of the heat deposit per unit pebble bed volume. However, the results show a decrease of the maximum temperature with the increase of the packing factor. A maximum temperature of 913°C is predicted for a PF of ~62.5%, while the peak temperature decreases to 892 °C for a PF of 65%. The reduction of the peak temperature is due to the increase of the total number of thermal contacts (overlaps + gaps). Figure 5–8 shows the number of thermal contacts evaluated for the simulated assemblies as the sum of the contacts acting among particles (counted once for each contact pair) and between particles and the top/bottom wall. When the PF increases, the number of the thermal contacts for each particle inside the assembly increases, thus the number of possible heat flux paths from one particle to its neighbors also increases. This leads to an increase of the effective thermal conductivity of the bed determining a lower temperature.To demonstrate this effect, the code presented in [77] was used to evaluate the effective thermal conductivity of the investigated assemblies at an average temperature of about 770 °C (the average temperature was estimated among the four investigated assemblies). Values of the effective thermal conductivities for the investigated assemblies characterized by different PFs are reported in Table 5–2.
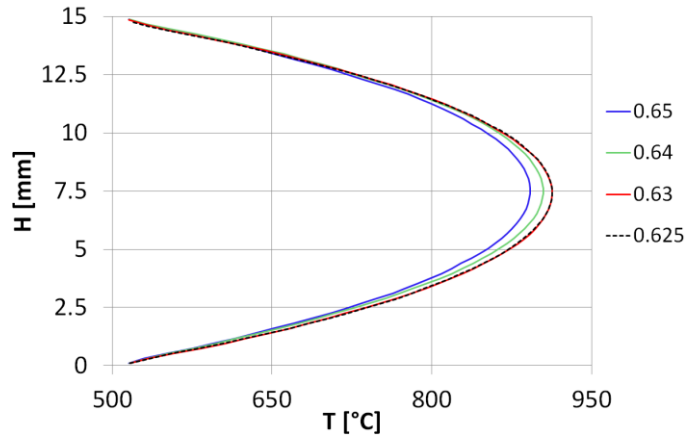
Figure 5–7: Temperature profiles obtained inside an OB blanket at 50mm from the first wall for different PFs.
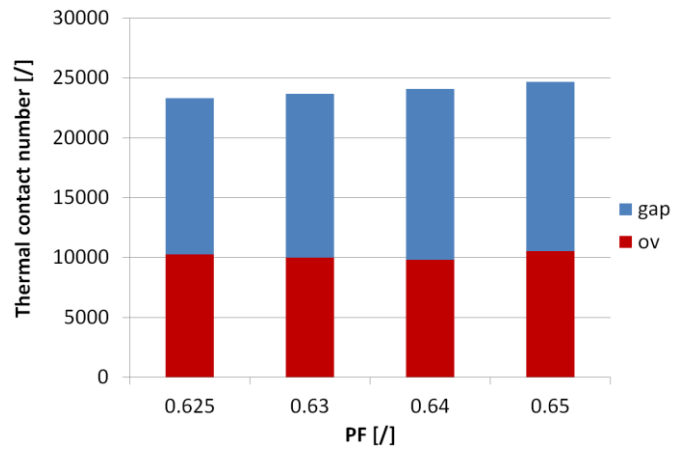
Figure 5–8: Number of thermal contacts detected for different PFs.

It can be seen that the relative increase of the effective thermal conductivity with the PF is larger than the relative increase of the heat deposit per unit pebble bed volume. Furthermore, Figure 5–8 suggests that the increase of the total number of thermal contacts with the packing factor is mainly due to the increase of the gap type thermal contacts involved in the heat transfer since the number of the overlaps is almost constant. This is due to the low initial stress level adopted (~20KPa) for the investigated assemblies. Therefore, for a given amount of particles with the same size distribution packed (according to the procedure described in Section 5.1) in a defined bed thickness with a fixed initial stress under a given neutronic power, assemblies exhibit a better heat exchange at higher PFs. This is due to the higher thermal conductivity determined by the larger amount of gap type thermal contacts involved in the heat transfer.

Table 5–2: Effective thermal conductivities of the investigated assemblies with different PFs evaluated at a given average temperature of 770°C

PF	0.625	0.63	0.64	0.65
k_{eff} [W/mK]	1.0005	1.0278	1.0708	1.1239

5.2.4 Influence of the gas pressure and gas type

In this section the influence of the gas pressure as well as of the filling gas type are analyzed. As explained in the Section 5.1.1, the tritium partial pressure is the driving force behind the tritium permeation into the cooling fluid [151] (Hanchar et al., 1982). Decreasing the purge gas pressure, the tritium permeation is consequently reduced in favor of a higher safety. However, even if the reduction of the purge gas pressure is beneficial for the reduction of the tritium permeation into the coolant, it also reduces the effective thermal conductivity of the breeder beds. It was reported that for pressures lower than 1.5 bar the Smoluchowski effect becomes important [156] (Yagi and Kunii, 1960) and [108] (Pupeschi et al., 2017). For this reasons, in the past years, the pressure of the purge gas was decreased from 4 to 2 bar [148] (Hernández et al., 2017) and [149] (Hernández et al., 2016), which is a trade-off between the minimization of the tritium and the maximization of the pressure to avoid the Smoluchowski effect.

Figure 5–9 shows the influence of the helium pressure at 4, 2, 1 and 0.1bar on the temperature profiles generated for the same assembly under standard conditions (see Section 5.1.1). As expected, an increase of the temperature is obtained when the gas pressure decreases. While slight increases of about 1.7 and 5% occur in terms of the peak temperatures when the gas pressure is reduced from 4 to 2 and 1 bar, respectively; the peak temperature increases by about 52% when the gas pressure decreases down to 0.1bar. At 1 and 0.1 bar, the temperature limit of 920°C is overcome reaching a maximum temperature of 933 and 1350°C, respectively. This behavior is due to the Smoluchowski effect, which determines a reduction of the thermal conductivity of the confined gas with the pressure. This leads to a reduction of the conductance in the thermal contacts, thus a lower heat flux is exchanged between particles.
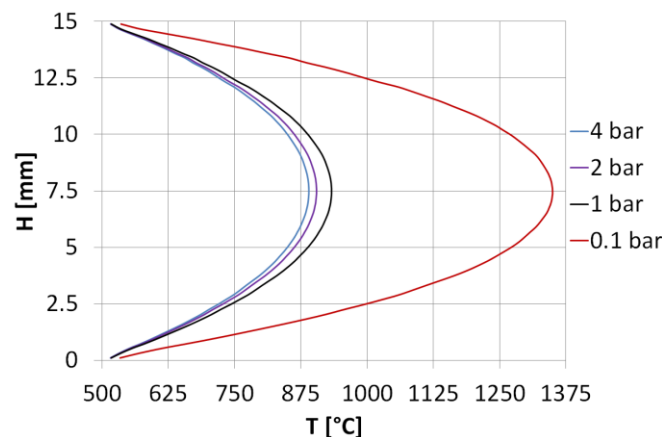
Figure 5–9: Temperature profiles inside an OB blanket at 50 mm for the first wall for different helium pressures.

Figure 5–10 shows the probability distributions of the effective thermal conductances C_{ij}^{eff} evaluated at 4, 2, 1 and 0.1 bar for the analyzed assembly. To evaluate the probability distribution reported in Figure 5–10, the thermal contacts among particles and between particles and the top/bottom wall were considered. As anticipated, the mean value of C_{ij}^{eff} is shifted to lower values when the gas pressure decreases.
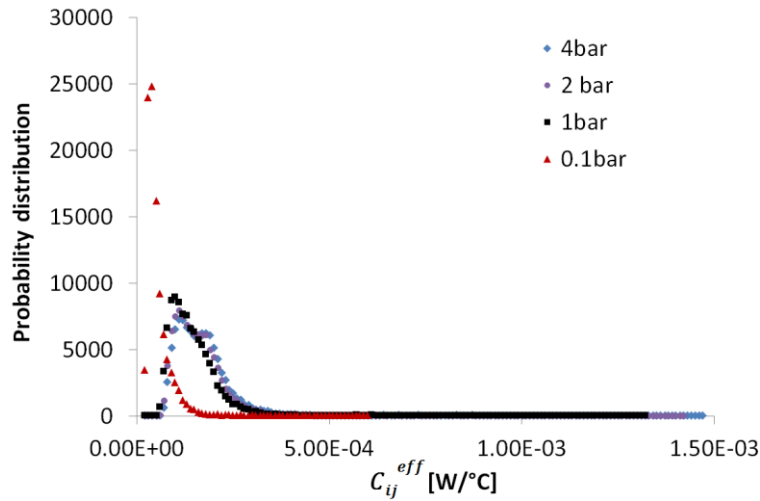

Figure 5–10: Probability distributions of the effective thermal conductances C_{ij}^{eff} evaluated at 4, 2, 1 and 0.1 bar for the same polydispersed assembly.

Considering an accident scenario such as an ex-vessel LOCA determined by the failure of the main helium pipes forming the first confinement barrier [157] (Boccaccini et al., 2006), the subsequent evolution of the accident could lead to the entrance of air into the breeder zone. In Figure 5–11, the temperature profiles generated inside the breeder beds under standard conditions (see Section 5.1.1) at 50 mm from the first wall are reproduced changing the filling gas from helium to air. Furthermore the influence of the gas pressure at 2 and 1 bar is analyzed for both gases. Comparing the results obtained at a given gas pressure, an increasing of ~30-40% is observed in terms of peak temperature when the filling gas is changed from helium to air. This is due to the different thermal conductivities of the two gases, indeed the thermal conductivity of the air is of about 40% lower than the helium thermal conductivity.

Figure 5–12 shows the probability distributions of the effective thermal conductances evaluated for thermal contacts considering only gap type thermal contacts. Since air has a lower thermal conductivity, for a fixed particle configuration and at a given pressure, the peak of the distribution is shifted to lower values compared to helium. Furthermore it has to be noticed that decreasing pressure from 2 to 1 bar, the peak temperature in air is reduced to about 1.6% vs. 3% in helium. This reflects the different reduction of the gas thermal

conductivity with the pressure. In Figure 5–13, the S-shape curves representing the reduction of the gas thermal conductivity with the gas pressure are reported for helium and air at 500 °C. The curves are obtained by means of Eqs. 4.12-4.15, for a fixed gap size of 30 μm and the gas properties reported in Table 4–4. Both gas thermal conductivities shown in Figure 5–13 are normalized to the respective gas thermal conductivity at unconfined condition. In air, the onset of the transition region is shifted to lower pressures resulting in a larger continuum region. This determines a lower slope of the curve between 1 and 2 bar in air than in helium. In particular, in the pressure range 1-2 bar, the helium thermal conductivity decreases by about 40%, while a reduction of ~3% is observed in air. Further details about the Smoluchowski effect inside packed beds are reported in Appendix B, where the variation of the S-shape curves as a function of temperature and gap size is evaluated according to Eqs. 4.12-4.15.
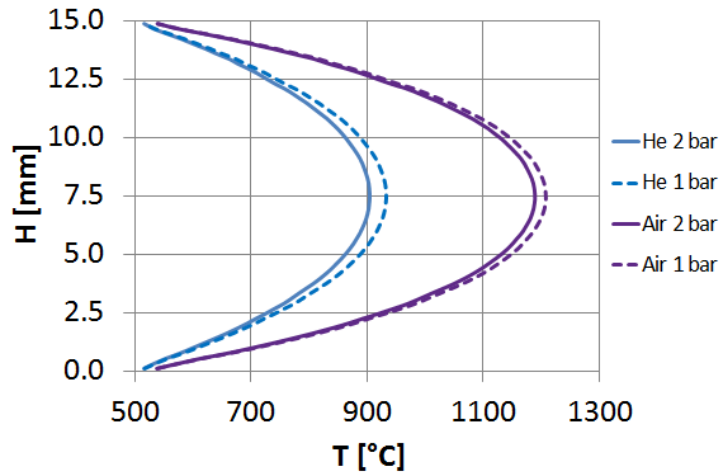
Figure 5–11: Temperature profiles generated at 50 mm from the FW with helium and air used as filling gas both at 2 and 1 bar.
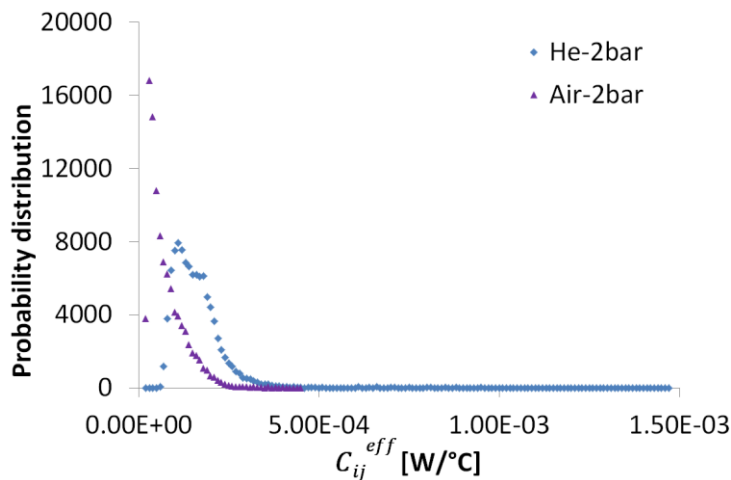
Figure 5–12: Probability distributions of the effective thermal conductances C_{ij}^{eff} evaluated using helium and air at 2 bar as filling gas.
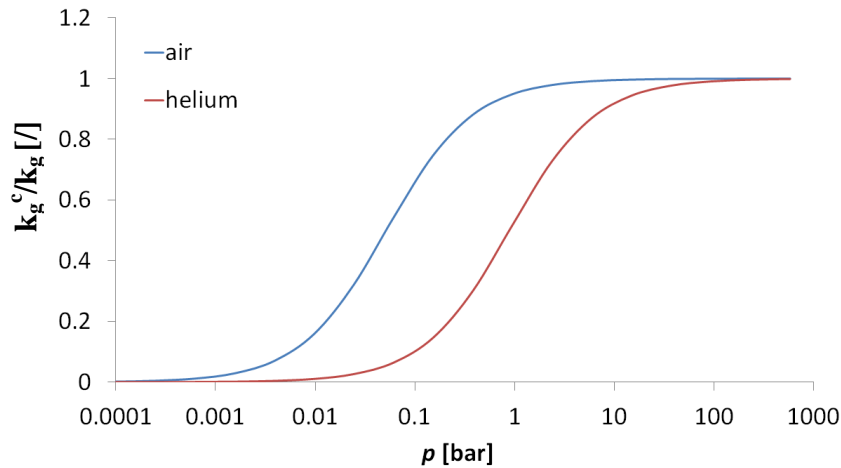
Figure 5–13: S-shape curves obtained for helium and air at 500 °C for a fixed gap size of 30 μm by means of Eq. 68-71 applying values reported in Table 4–4

5.2.5 Influence of the solid material

In order to study the influence of the solid material, three different investigations have been carried out. First, sensitivity studies were performed varying the thermal conductivity of the solid material. Then, the temperature profiles generated using different tritium breeder materials have been compared and the influence of the porosity was investigated. Finally, the influence of different correlations reported in literature characterizing the thermal conductivity of the same solid material was analyzed. Simulations were carried out under the standard conditions defined in the Section 5.1.1 at 50mm from the first wall.

For the first investigation, the thermal conductivity of the EU Ref. material was first varied by ±5% according to the uncertainty reported in [132] (Löbbecke and Knitter, 2007) to evaluate the influence of the experimental error on the simulated thermal behavior of the bed. Then the thermal conductivity was varied by ±10% to investigate the maximum acceptable deviation for the fulfillment of the temperature design limits.

The results are summarized in Figure 5–14 (dashed and dotted lines) and compared to the temperature profile obtained with the reference thermal conductivity (solid black line). The results confirm that a decrease of the solid thermal conductivity leads to an increase of the temperature in the bed and vice versa. In particular, a variation of ±1.3% and ±3% in terms of peak temperature was predicted when the thermal conductivity is changed by ±5% and ±10%, respectively. While a reduction of 5% determines a peak temperature of about 917 °C, fulfilling the temperature limit of 920 °C, a reduction of 10% generates an unacceptable maximum temperature of 931°C in the simulated conditions. Increasing the thermal conductivity by about 5% and 10%, the peak temperature decreases without compromising the TRT.
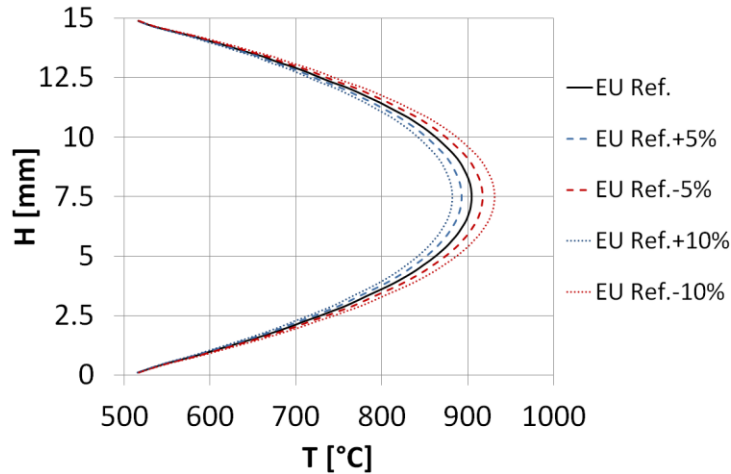
Figure 5–14: Temperature profiles generated at 50 mm from the first wall varying the thermal conductivity of the EU Ref. material.

As second step, the temperature profiles obtained using EU Ref., Li_2ZrO_3, LiO_2 and Li_2TiO_3 as solid materials with the same porosity (11%) have been evaluated. Since the solid materials exhibit different thermal conductivities under different porosities (Löbbecke and Knitter, 2007 [132]; Saito, 1998 [142]; Gierszewski, 1993 [143]), the influence of the porosity was investigated, additionally, since the porosity of the currently produced pebbles ranges from ~ 5% [7] (Shikama et al., 2008) to ~13% [13] (Hoshino, 2013). This sensitivity study was carried out for Li_2TiO_3 reducing the porosity from 11 to 5%. The results are shown in Figure 5–15. The solid lines refer to different solid materials with the same porosity of 11%, while the dashed line indicates the temperature profile of Li_2TiO_3 pebbles at 5% of porosity. The results demonstrate that materials with a higher thermal conductivity as LiO_2, more easily transfer the heat generated by the neutronic heating reaching a lower temperature for the given thickness. According to thermal conductivities reported in Figure 5–2, a slight deviation occurs between results obtained using Li_2TiO_3 and EU Ref. materials. Comparing the solid and dashed red curve, the influence of the porosity can be estimated for Li_2TiO_3. The porosity dependent thermal conductivity was calculated with the correlation reported in [142] (Saito et al., 1998). Due to the reduction of the voids, when the porosity decreases the thermal conductivity of the solid material increases determining a lower temperature in the assembly. In this specific case a reduction of 6% in porosity leads to a reduction of about 2.6% in terms of peak temperature.

Finally the influence of the implemented correlation used to evaluate the thermal conductivity of a solid material has been investigated. In Figure 5–16, three temperature profiles are shown. The three curves are generated using three different correlations to evaluate the thermal conductivity of Li_4SiO_4 at 11% of porosity presented in Figure 5–3. While a negligible difference occurs using the correlations reported in [139] and [154], the

temperature profile using the correlation given in [153] greatly differ. Due to the much lower thermal conductivity evaluated in [153], the peak temperature is well above the temperature limit for Li_4SiO_4 and the major part of the bed thickness experiences temperatures above 920°C.
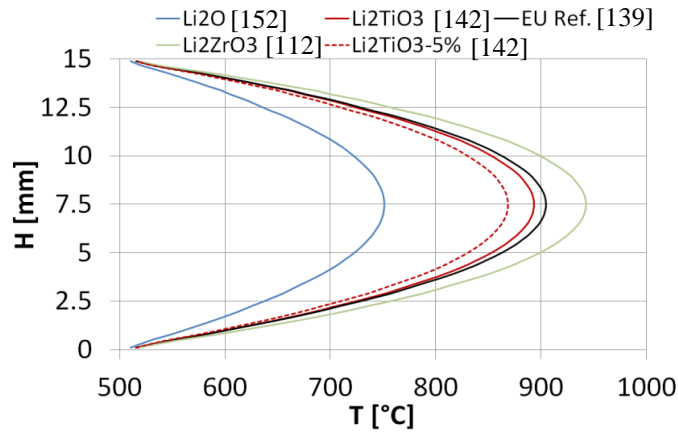

Figure 5−15: Temperature profiles generated at 50 mm from the first wall using the EU Ref., Li_2ZrO_3, LiO_2 and Li_2TiO_3 as solid materials.
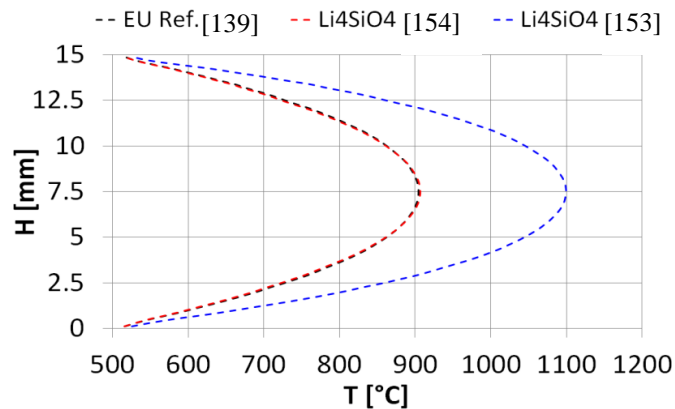

Figure 5−16: Temperature profiles generated at 50 mm three different correlations reported in literature for the thermal conductivity of the Li_4SiO_4 at 11% of porosity.

5.2.6 Influence of the cycling load

In order to investigate the influence of the compression level and particle rearrangement on the heat transfer in the breeder pebble beds, a cyclic load was applied on the standard assembly (see Section 5.1.1). Figure 5−17 shows the stress-strain curves resulting from the 1st, 2nd, 5th, 10th and 30th cycle, which were considered for the analysis reported in this section. The assembly is cyclically loaded until 6MPa and unloaded up to ~20 KPa. In Figure 5−18 the temperature profiles at 50 mm from the first wall at ~20 KPa and ~6MPa for the listed cycle number are shown. For a given stress level, the results exhibit a negligible variation of the temperature profile with cycling. In terms of peak temperature, a reduction of about 0.5% is

detected after thirty cycles. For the given cycle, the peak temperature decreases by about 1% when the assembly is compressed from about 20KPa to 6MPa.
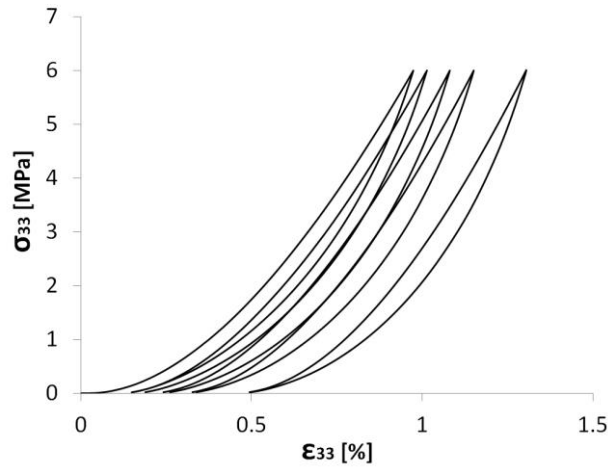
Figure 5–17: Stress-strain curves resulting from the 1st, 2nd, 5th, 10th and 30th load cycle.
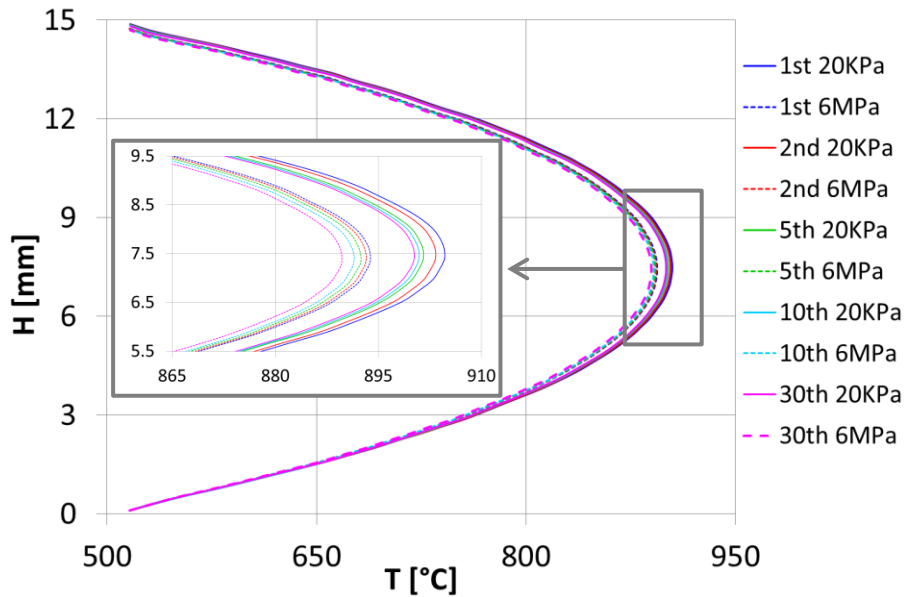

Figure 5–18: Temperature profiles generated at 50 mm from the first wall at the compression state of the corresponding cyclic point reported in the legend.

In Figure 5–19 and in Figure 5–20, the variation of the total effective thermal conductances and of the total contact number, given by overlap type contacts (red zone) and gap type thermal contacts (blue zone), are shown as a function of the compression state for the corresponding cyclic load, respectively. Here, total effective thermal conductance is defined as the sum of all thermal conductances of the thermal contacts detected, first, among particles in the assembly and, second, with the top and bottom walls. Peaks and valleys alternate when the assembly is loaded and unloaded, respectively. By loading the assembly, new contacts are generated, small gaps turn in overlaps and the existing contacts areas increase. This leads to an increase of the total thermal conductance given by overlaps associated to a reduction of the

gap total thermal conductance. The opposite occurs when the assembly is unloaded. Furthermore, after each unloading, the number of the particles rearranged into a permanent state of equilibrium slightly increases determining a higher number of contacts and thus a higher $C^{eff}_{sum\_ov}$. This leads to an increase of the total heat flux exchanged among particles generating the slight reduction of the temperature field shown in Figure 5–18.
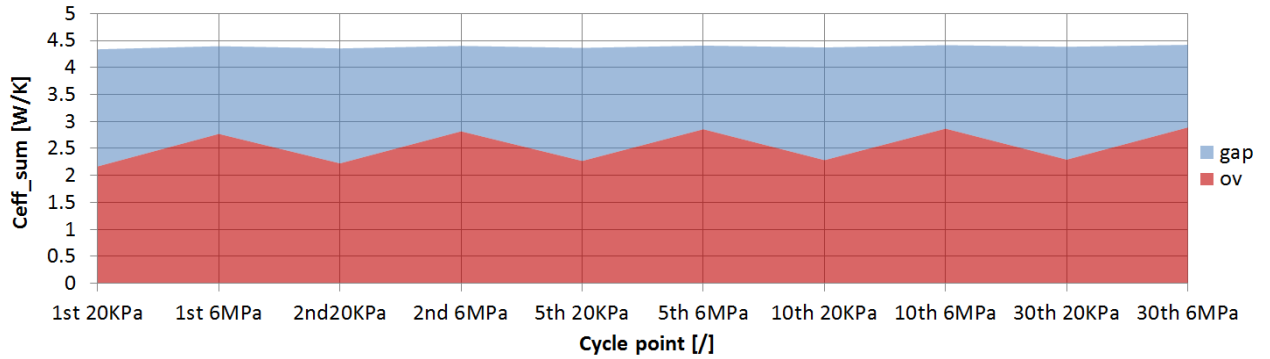

Figure 5–19: Total effective thermal conductances C^{eff}_{sum} of gaps and overlaps evaluated at the compression state of the corresponding cyclic load reported in the legend.
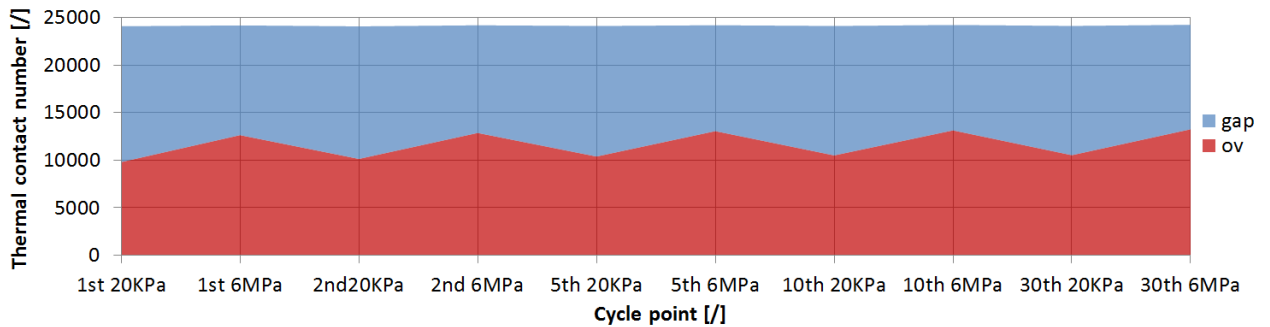
Figure 5–20: Thermal contact number of gaps and overlaps evaluated at the compression state of the corresponding cyclic load reported in the legend.

5.2.7 Influence of the particle size

In this section, the influence of the particle size on the heat transfer in the breeder pebble bed was investigated. Temperature profiles generated in the bed thickness with assemblies of monosized and polydispersed particles were compared. In Figure 5–21, four temperature profiles obtained under standard condition (see Section 5.1.1) referring to a polydispersed (Figure 4–3) packed bed and three assemblies of monosized particles with different radius of 0.13, 0.22 and 0.32 mm are shown. The three chosen radii refer to the maximum, minimum and the average value of the size distribution given in Figure 4–3. When the radius of the particles increases, the peak temperature reached inside the bed decreases. This occurs because larger contact areas are involved in assemblies composed of bigger spheres. As shown in Figure 5–22, when the radius of the particles increases, the mean contact area radius is shifted to higher values. Larger contact areas determine a higher effective thermal

conductivity of the bed leading to a lower temperature field in the bed. For the same reason, since the main value of the radius of the applied polydispersed size distribution is about 0.15-0.16mm, the temperature profile of the polydispersed assembly falls between curves of monosized packed particle with a radius of 0.13 and 0.22mm. Therefore, under the simulated conditions if the peak of the size distribution of the currently produced pebbles is shifted to a lower size, it has to be expected that there is a slight increase of the maximum temperature generated in the bed that is beyond the design limits.
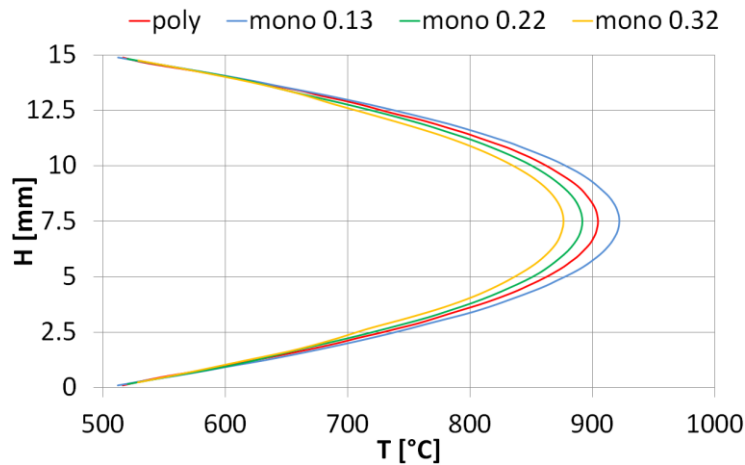
Figure 5–21: Temperature profiles at 50 mm from the first wall with assemblies of polydispersed (see Figure 4–3) and monosized particles with different radius.
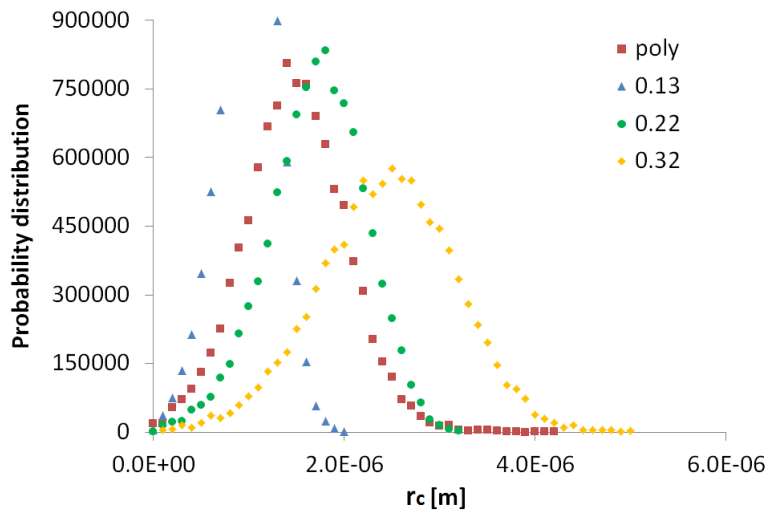
Figure 5–22: Probability distribution of contact radii. Different curves refer to assemblies of polydispersed (see Figure 4–3) and monosized particles with different radius.

Chapter 6

Conclusions

In the framework of the research studies dedicated to the design of the solid breeder blanket concept, the knowledge of the thermo-mechanical behavior of the ceramic breeder pebble beds at fusion relevant conditions is of primary importance. Designers are constantly supported by experiments and numerical simulations to establish an adequate design of the blanket. In this sense, the DEM is an essential tool to predict the behavior of fusion pebble beds as result of the interactions occurring in the bed such as particle-particle, particle-wall and particle-purge gas. Furthermore, modelling particles individually and studying the bed at the granular level phenomena otherwise inaccessible with other tools can be investigated. In this work, the DEM approach was used to investigate first the influence of the particles' shape on the mechanical behavior of the breeder pebble beds and then the heat transfer inside these multiphase material systems.

Starting from the existing in-house mechanical DEM code, developed to study the mechanical behavior of ceramic breeder pebble beds composed by perfectly spherical spheres, a new method was developed to study the influence of the particles' shape. The slight deviation from a perfect spherical shape of the currently produced pebbles was simulated by means of ellipsoidal particles. Assemblies of monosized ellipsoidal particles highly packed in a virtual cubic box under a periodic configuration were generated and then compressed in the axial direction to study the mechanical response. The results show that the initial packing factor as well as the aspect ratio of the particles play an important role in the mechanical response to an external excitation. A softer behavior is observed for low packing factors and high aspect ratios. An irreversible macroscopic deformation of pebble beds is seen for the investigated assemblies, where only elastic particles are simulated. This suggests that the rearrangement of the particles composing the bed is an important mechanism for macroscopic irreversibility. It was found that particles with high aspect ratios rearrange more easily due to the higher mobility determining a larger residual strain after unloading. This behavior also suggests that these structures are further away from their maximum PF, compared to assemblies of spheres. Therefore, to avoid the generation of large gaps between pebbles and walls during the blanket operation, PFs higher than 64% should be considered as targets for particles with sphericities larger than 1. In this sense, further analyses are needed to extend the simulation to polydispersed assemblies of ellipsoidal particles with a relevant distribution of the sphericity. Analyzing the microscopic interactions, correlations linking the average and

maximum normal forces as well as the coordination number to the macroscopic hydrostatic pressure were found. These correlations together with the statistical analysis of the force distribution in the assemblies give important information as basis for the estimation of the crash probability of the particles, which is essential to evaluate the dust formation inside the bed.

For the second aim of this work, an innovative in-house thermal DEM was developed to investigate the heat transfer in ceramic breeder pebble beds accounting for the Smoluchowski effect for the first time in a DEM code. This represents a step forward for thermal DEM simulations allowing the investigation of the gas pressure in granular beds. According to the Smoluchowski effect, when a gas is confined in small gaps, its thermal conductivity decreases with the gas pressure, affecting the effective thermal conductivity of the bed and, thus, its thermal behavior. In order to simulate the heat transfer among particles, a 3D resistor network model was implemented, where contacting particles and particles separated by relevant gaps up to half of their equivalent radius were considered as thermal contacts.

First, the code was used to estimate the effective thermal conductivity of the bed under an imposed thermal gradient at a certain temperature. The code was calibrated and validated through a comparison to experimental results reported in literature. The numerical results perfectly resembled the experimental data with a good agreement for different gas types, ceramic materials, temperatures, gas pressures and compression states of the bed, confirming the predictive capability of the code. While a negligible influence of the compression state on the effective thermal conductivity of the bed was observed, a strong influence of the gas pressure was evaluated. The typical S-shape curve characteristic of the Smoluchowski effect was successfully reproduced indicating a strong reduction of the effective thermal conductivity of the bed for helium pressures lower than 1 bar. The solid materials as well as the gas type were found to play a major role in the heat transfer mechanism.

Afterwards, the code was applied to estimate the temperature field generated by neutronic heating in the breeder zone of the DEMO HCPB blanket. The effect of relevant blanket parameters such as packing factor, pebble material/size, characteristics of the purge gas, compressive load and bed height were investigated. Generated under a periodic configuration for the lateral sides, the used assemblies represent a column cutout of the breeder beds bounded by an upper and bottom wall simulating the cooling plates. A strong influence of the neutronic heating acting along the radial length of the breeder zone was established. Increasing the radial distance from the plasma face, the neutronic heating decreases, determining a lower bed temperature for a given thickness. In particular, for a bed thickness

of 15 mm, a peak temperature of about 907 and 573°C was detected at 50 and 450 mm from the first wall, respectively. Under the simulated conditions, the predicted values satisfy the temperature limit of 920°C avoiding the sintering of the pebble. Sensitivity studies of the bed thicknesses showed that higher beds generate higher temperatures under the same imposed power density. While at 50mm higher bed should be avoided to be in agreement with the temperature limit, thicker beds for zones with a lower power density are suggested to further decrease the TRT. In order to reduce the tritium permeation in the cooling plates, a reduction of the purge gas pressure was recently adopted indicating 2 bar as suitable for the breeder zone of the HCPB blanket. This value is the best compromise between reducing the tritium permeation and avoiding a strong reduction of the effective thermal conductivity of the bed due to the Smoluchowski effect. Parametric sensitivity studies showed that reducing the gas pressure from 2 to 1 bar, an increase of the peak temperature by 5% is detected and the limit of 920°C is overcome. Simulating an accident scenario of an ex-vessel LOCA, air was used as filling gas. Due to the lower thermal conductivity of air compared to helium, the estimated peak temperature of the bed strongly increases exceeding 1100°C. Sensitivity studies demonstrate the importance of the size distribution of the produced pebbles. In particular, when the peak of the size distribution is shifted to higher diameters, a lower temperature is reached in the bed. A variation of 40% of the pebbles' diameter determines a variation of about 3.4% of the peak temperature in the bed. Finally, the influence of the solid material was evaluated and the effect of the porosity was estimated. According to the obtained results, when the porosity increases, the thermal conductivity of the solid material decreases generating a lower temperature field in the bed. At the same time, studies revealed the necessity to create a reliable database characterizing the thermal properties of the solid materials with unique and valid correlations.

The developed thermal DEM code presented in this chapter is a first approach to investigate the heat transfer inside the breeder material system for a fusion reactor. Due to the BB relevant conditions, the proposed model is a good approximation of the physical reality. However, in order to extend the applicability of the code to other fields and materials, phenomena such as the thermal radiation and thermal expansion need to be taken into account.

Bibliography

[1]   S. Azteni and J. Meyer-ter-Vehn, "The Physics of Inertial Fusion", chap01-Nuclear fusion reactions, Published online January 2008, e-ISBN: 9780191714030, DOI: http://dx.doi.org/10.1093/acprof:oso/9780198562641.001.0001 (November 27, 2018).

[2]   F. Cismondi, Lecture: Basics of breeding blanket technology, 5th Karlsruhe International School on Fusion Technologies 2011, http://staff.polito.it/roberto.zanino/sub1/teach_files/current_topics/lect_cismondi.pdf (November 27, 2018).

[3]   Y. Xu, "A general comparison between tokamak and stellarator plasmas", Matter and Radiation at Extremes, Volume 1- Issue 4, 2016, Pages 192-200.

[4]   J. G. van der Laan, B. Cuquel, D. Demange, B. -E. Ghidersa, L. M. Giancarli, M. Iseli, T. Jourdan, J. -C. Nevière, R. Pascal, W.Ring, "Preparation of acceptance tests and criteria for the Test Blanket Systems to be operated in ITER", Fusion Engineering and Design, Volumes 98–99, 2015, Pages 1889-1892.

[5]   https://www.iter.org/mach/TritiumBreeding, (November 27, 2018).

[6]   F. Hernandez, F. Cismondi , S. Kecskes, B. Kiss,"Thermo-mechanical analyses and assessment with respect to the design codes and standards of the HCPB-TBM Breeder Unit", Fusion Engineering and Design, Volume 87-Issues 7-8, 2012, Pages 1111–1117.

[7]   T. Shikama, R. Knitter, J. Konys, T. Muroga, K. Tsuchiya, A. Möslang, H. Kawamura, S. Nagata, "Status of development of functional materials with perspective on beyond-ITER", Fusion Engineering and Design, Volume 83-Issues 7-9, 2008, Pages 976–982.

[8]   A. Ying, M. Akiba, L. V. Boccaccini, S. Casadio, G. Dell'Orco, M. Enoeda, K. Hayashi, J. B. Hegeman, R. Knitter, J. van der Laan, J. D. Lulewicz, Z. Y. Wen, "Status and perspective of the R&D on ceramic breeder materials for testing in ITER", Journal of Nuclear Materials, Volumes 367–370-Part B, 2007, Pages 1281–1286.

[9]   A. Ying, J. Reimann, L. Boccaccini, M. Enoeda, M. Kamlah, R. Knitter, Y. Gan, J. G. van der Laan, L. Magielsen, P. A. Di Maio, G. Dell'Orco, R. K. Annabattula, Jon T.Van Lew, H. Tanigawa, S. Til, "Status of Ceramic Breeder Pebble Bed Thermo-mechanics R&D and Impact on Breeder Material Mechanical Strength", Fusion Engineering and Design, Volume 87, Issues 7–8, 2012, Pages 1130-1137.

[10] I. R. Cristescu, L. Doerr, M. Glugla, D. Murdoch, "Tritium inventories and tritium safety design principles for the fuel cycle of ITER", Nuclear Fusion, Volume 47, 2007, Page S458.

[11] R. Knitter, M. H. H. Kolb, U. Kaufmann, A. A. Goraieb, "Fabrication of modified lithium orthosilicate pebbles by addition of titania", Journal of Nuclear Material, Volume 442 – Issues 1-3, 2013, Pages S420–S424.

[12] X. Wu , Z. Wen, X. Xu, Y. Liu, "Fabrication of Li4SiO4 pebbles by a sol–gel technique", Fusion Engineering and Design, Volume 85 - Issue 2, 2010, Pages 222–226.

[13] T. Hoshino, "Development of fabrication technologies for advanced tritium breeder pebbles by the sol–gel method", Fusion Engineering and Design, Volume 88 – Issues 9-10, 2013, Pages 2264–2267.

[14] D. Mandal, M. R. K. Shenoi, S. K. Ghosh , "Synthesis & fabrication of lithium-titanate pebbles for ITER breeding blanket by solid state reaction & spherodization", Fusion Engeneering and Design, Volume 85 – Issue 5, 2010, Pages 819–823.

[15] P. A. Cundall and O. D. L. Strack., "A discrete numerical model for granular assemblies". Geotechnique, Volume 29 – Issue 1, 1979, Pages 47-65.

[16] H. J. Herrmann and S. Luding., "Modeling granular media on the computer", Continuum Mechanics and Thermodynamics, Volume 10 – Issue 4, 1998, Pages 189-231.

[17] C. Thornton and S. J. Antony, "Quasi-static deformation of particulate media", Philosophical Transactions of the Royal Society of London Series a-Mathematical Physical and Engineering Sciences, Volume 356 – Issue 1747, 1998, Pages 2763-2782.

[18] C. L. Martin, D. Bouvard, and S. Shima, "Study of particle rearrangement during powder compaction by the Discrete Element Method", Journal of the Mechanics and Physics of Solids, Volume 51- Issue 4, 2003, Pages 667-693.

[19] Z. Lu, A. Ying, M. Abdou, "Numerical and experimental prediction of the thermomechanical performance of pebble beds for solid breeder blanket", Fusion Engineering and Design, Volume 49-50, 2000, Pages 605-611.

[20] P. W. Cleary, "DEM simulation of industrial particle flows: case studies of drag line excavators, mixing in tumblers and centrifugal mills", Powder Technology, Volume 109, 2000, Pages 83–104.

[21] P. Redanz and N. A. Fleck., "The compaction of a random distribution of metal cylinders by the discrete element method", Acta Materialia, Volume 49 - Issue 20, 2001, Pages 4325-4335.

[22] C. L. Martin, D. Bouvard, S. Shima, "Study of particle rearrangement during powder compaction by the Discrete Element Method", Journal of the Mechanics and Physics of Solids, Volume 51 - Issue 4, 2003, Pages 667-693.

[23] G. Marketos and M. D. Bolton, "Quantifying the extent of crushing in granular materials: A probability-based predictive method", Journal of the Mechanics and Physics of Solids, Volume 55 - Issue 10, 2007, Pages 2142-2156.

[24] Z. An, A. Ying, M. Abdou, "Application of discrete element method to study mechanical behaviors of ceramic breeder pebble beds", Fusion Engineering and Design, Volume 82, 2007a, Pages 2233–2238.

[25] Z. An, A. Ying, M. Abdou, "Numerical characterization of thermo-mechanical performance of breeder pebble beds", Journal of Nuclear Materials,Volumes 367–370, 2007, Pages 1393–1397.

[26] F. A. Gilabert, J. N. Roux, A. Castellanos, "Computer simulation of model cohesive powders: Influence of assembling procedure and contact laws on low consolidation states", Physical Review E, Volume 75 –Issue-1, 2007, Pages 011303_1-011303_26.

[27] Y. Gan "Thermo-mechanics of pebble beds in fusion blankets", PhD Thesis, Universität Karlsruhe (TH), 2008 https://publikationen.bibliothek.kit.edu/1000010009 (November 27, 2018).

[28] Y. Gan and M. Kamlah "Discrete element modelling of pebble beds: with application to uniaxial compression tests of ceramic breeder pebble beds", Journal of the Mechanics and Physics of Solids, Volume 58 – Issue 2, 2010, Pages129–144.

[29] Y. Gan, M. Kamlah, J. Reimann, "Computer simulation of packing structure in pebble beds", Fusion Engineering and Design, Volume 85, 2010, Pages 1782–1787.

[30] S. Zhao "Multiscale Modeling of Thermomechanical Properties of Ceramic Pebbles", PhD Thesis, Universität Karlsruhe (TH), 2011 https://www.ksp.kit.edu/9783866446281 (November 27, 2018).

[31] R. K. Annabattula, Y. Gan, M. Kamlah, "Mechanics of binary and polydisperse spherical pebble assembly", Fusion Engineering and Design, Volume 87, 2012a, Pages 853–858.

[32] R. K. Annabattula, Y. Gan, S. Zhao, M. Kamlah, "Mechanics of a crushable pebble assembly using discrete element method", Journal of Nuclear Materials, Volume 430, 2012b, Pages 90–95.

[33] S. Zhao et al., "Failure initiation and propagation of Li4SiO4 pebbles in fusion blankets", Fusion Engineering and Design 88 (2013), pp. 8-16.

[34] S. Pupeschi, R. Knitter, M. Kamlah, Y. Gan, "Numerical and experimental characterization of ceramic pebble beds under cycling mechanical loading", Fusion Engineering and Design, Volume 112, 2016, Pages 162-168.

[35] H. Goldstein, C. P. Poole and J. L. Safko, Classical Mechanics (3rd Edition), Boston: Addison Wesley 2001, ISBN: 0201657023.

[36] D. J. Evans, S. Murad, "Singularity free algorithm for molecular dynamics simulation of rigid polyatomics", Molecular Physics, Volume 34, 1997, Pages 327–331.

[37] X. Lin, T. T. Ng, "Contact detection algorithms for three-dimensional ellipsoids in discrete element modelling", International Journal for Numerical Analalysis Methods in Geomechanics, Volume 19, 1995, Pages 653–659.

[38] X. Lin, T. T. Ng, "A three-dimensional discrete element model using arrays of ellipsoids", Géotechnique, Volume 47, 1997, Pages 319–329.

[39] H. Ouadfel, L. Rothenburg, "Analgorithm for detecting inter-ellipsoid contacts", Computers and Geotechnics, Volume 24, 1999, Pages 245–263.

[40] G.G.W. Mustoe, M. Miyata, "Material flow analyses of non circular-shaped granular media using discrete element methods", Journal of Engineering Mechanics, Volume 127, 2001, Pages 1017–1026.

[41] A. Donev, S. Torquato, F. H. Stillinger, "Neighbor list collision-driven molecular dynamics simulation for non spherical hard particles: II. Applications to ellipses and ellipsoids", Journal of Computational Physics, Volume 202, 2005, Pages 765–793.

[42] E.J.W. Wynn, "Simulations of rebound of an elastic ellipsoid colliding with a plane", Powder Technology, Volume 196, 2009, Pages 62–73.

[43] B. Yan, R. A. Regueiro, S. Sture, "Three-dimensional ellipsoidal discrete element modeling of granular materials and its coupling with finite element facets", Engineering Computation, Volume 27 − Issue 4, 2010, Pages 519–550.

[44] R.M. Baram, P.G. Lind, "Deposition of general ellipsoidal particles", Physical Review, Volume E 85, 2012, Pages 041301_1- 041301_9.

[45] Q.J. Zheng, Z. Y. Zhou, A. B. Yu, "Contact forces between viscoelastic ellipsoidal particles", Powder Technology, Volume 248, 2013, Pages 25–33.

[46] A.H. Barr, "Super quadrics and angle preserving transformations", IEEE Computer Graphics and Applications, Volume 1, 1981, Pages 11–23.

[47] J.R. Williams, R. O'Connor, "A linear complexity intersection algorithm for discrete element simulation of arbitrary geometries", Engineering Computations, Volume 12, 1995, Pages 185–201.

[48] C. Hogue, "Shape representation and contact detection for discrete element simulations of arbitrary geometries", Engineering Computations, Volume 15, 1998, Pages 374–390.

[49] G. Lu, J. R. Third, C. R. Müller, "Discrete element models for non-spherical particle systems: From theoretical developments to applications", Chemical Engineering Science, Volume 127, 2015, Pages 425–465.

[50] Z. Ning, R. Boerefijn, M. Ghadiri, C. Thornton, "Distinct element simulation of impact breakage of lactose agglomerates", Advanced Powder Technology, Volume 8 – Issue 1, 1997, Pages 15–37.

[51] J.F. Favier, M. H. Abbaspour-Fard; M. Kremmer, "Modeling non-spherical particles using multi-sphere discrete elements", Journal of Engineering Mechanics, Volume 127 – Issue 10, 2001, Pages 971–977.

[52] J.F. Favier, M. H. Abbaspour-Fard; M. Kremmer, A. O. Raji, "Shape representation of axi-symmetrical, non-spherical particles in discrete element simulation using multi-element model particles" Engineering Computations, Volume 16, 1999, Pages 467–480.

[53] C. Thornton, M. T. Ciomocosa, M. J. Adamsb, "Numerical simulations of agglomerate impact breakage" Powder Technology, Volume 105, 1999, Pages 74–82.

[54] K. D. Kafui, C. Thornton, "Numerical simulations of impact breakage of a spherical crystalline agglomerate" Powder Technology, Volume 109, 2000, Pages 113–132.

[55] D. Markauskas , R. Kačianauskas, A. Džiugys, R. Navakas, "Investigation of adequacy of multi-sphere approximation of ellipsoid particles for DEM simulations", Granular Matter, Volume 12, 2010, Pages 107–123.

[56] J. F. Ferellec, G. R. McDowell "A simple method to create complex particle shapes for DEM" Geomechanics and Geoengineering, An International Journal, 3:3, 2008, Pages 211–216.

[57] J. F. Ferellec, G. R. McDowell, "Modelling realistic shape and particle inertia in DEM", Géotechnique, Volume 60, 2010a, Pages 227–232.

[58] J. F. Ferellec, G. R. McDowell, "A method to model realistic particle shape and inertia in DEM", Granular Matter, Volume 12, 2010b, Pages 459–467.

[59] E. J. R. Parteli, "Using LIGGGHTS for performing DEM simulations of particles of complex shapes with the multi sphere method", Proceedings of the 6th International Conference on Discrete Element Method" Colorado, USA, 2013a.

[60] E. J. R. Parteli, "DEM simulation of particles of complex shapes using the multi sphere method: application for additive manufacturing", AIP Conference Proceedings, 1542-185, 2013b, Pages 185–188.

[61] H. Kruggel Emden, S. Rickelt, S.Wirtz, V. Scherer , "A study on the validity of the multi-sphere discrete element method", Powder Technology, Volume 188 – Issue 2, 2008, Pages 153–165.

[62] M. Kodam, R. Bharadwaj, J. Curtis, B. Hancock, C. Wassgren, "Force model considerations for glued sphere discrete element method simulations", Chemical Engineering Science, Volume 64 – Issue 15, 2009, Pages 3466–3475.

[63] D. Höhner, S.Wirtz, H. Kruggel-Emden, V. Scherer, "Comparison of the multi-sphere and polyhedral approach to simulate non-spherical particles within the discrete element method: Influence on temporal force evolution for multiple contacts", Powder Technology, Volume 208 – Issue 3, 2011, Pages 643–656.

[64] F. Alonso Marroquín, S. A. Galindo-Torres, A. Tordesillas, Y. Wang, "New perspectives for discrete element modeling: merging computational geometry and molecular dynamics", Proceedings of the 6th International Conference on Micromechanics of Granular Media, Golden, USA, 2009, Pages 825–828.

[65] R. Hart, P. A. Cundall, J. Lemos, "Formulation of a three-dimensional distinct element model – Part II. Mechanical calculations for motion and interaction of a system composed of many polyhedral blocks", International Journal of Rock Mechanics and Mining Sciences & Geomechanics Abstracts, Volume 25 – Issue 3, 1998, Pages 117–125.

[66] M. A. Hopkins, "Polyhedra faster than spheres ?", Engineering Computations, Volume 31-Issue 3, 2014, Pages 567–583.

[67] P. A. Cundall, "Formation of a three-dimensional distinct element model – part I: a scheme to detect and represent contacts in a system composed of many polyhedral blocks", International Journal of Rock Mechanics and Mining Sciences & Geomechanics Abstracts, Volume 25 - Issue 3, 1998, Pages 107–116.

[68] E.G. Nezami, Y. M. A. Hashash, D. Zhao, J. Ghaboussi, "A fast contact detection algorithm for 3-D discrete element method", Computers and Geotechnics, Volume 31 – Issue 7, 2004, Pages 575–587.

[69] E. G. Nezami, Y. M. A. Hashash, D. Zhao, J. Ghaboussi, "Shortest link method for contact detection in discrete element method", Internal Journal for Numerical and Analitical Methods in Geomechanics, Volume 30, 2006, Pages 783–801.

[70] D. Zhao, E. G. Nezami, Y. M. A. Hashash, J. Ghaboussi, "Three-dimensional discrete element simulation for granular materials", Engineering Computations, Volume 23 – Issue 7, 2006a, Pages 749–770.

[71] D. Zhao, E. G. Nezami, Y. M. A. Hashash, J. Ghaboussi, "Discrete element modeling of polyhedral representation of granular materials", Proceedings of the 10th Biennial International Conference on Engineering, Construction and Operations in Challenging Environments and the 2nd NASA/ARO/ASCE Workshop on Granular Materials in Lunarand Martian Exploration. League City/ Houston, USA, 2006b, Pages 1–9.

[72] A. Abou-Sena, A. Ying, M. Abdou, "Effective thermal conductivity of lithium ceramic pebble beds for fusion blankets: a review", Fusion Technology, Volume 47 - Issue 4, 2005, Pages 1094–1100.

[73] F. Franza, L. V. Boccaccini, A. Ciampichetti, M. Zucchetti, "Tritium transport analysis in HCPB DEMO blanket with the FUS-TPC code", Fusion Engineering and Design, Volume 88 - Issues 9–10, 2013, Pages 2444-2447.

[74] Y. Asakuma Y. Kanazawa, T. Yamamoto, "Thermal radiation analysis of packed bed by a homogenization method", International Journal of Heat and Mass Transfer, Volume 73, 2014, Pages 97–102.

[75] X. Lu, R. Caps, J. Fricke, C. T. Alviso, R. W. Pekala, "Correlation between structure and thermal conductivity of organic aerogels", Journal of Non-Crystalline Solids, Volume 188 - Issue 3, 1995, Pages 226-234.

[76] H. Wu, N. Gui, X. Yang, J. Tu, S. Jiang, "Effect of scale on the modeling of radiation heat transfer in packed pebble beds", International Journal of Heat and Mass Transfer, Volume 101, 2016, Pages 562–569.

[77] M. Moscardini, Y. Gan, S.Pupeschi, M. Kamlah, "Discrete element method for effective thermal conductivity of packed pebbles accounting for the Smoluchowski effect", Fusion Engineering and Design, Volume 127, 2018, Pages 192-201.

[78] G. K. Batchelor and R. W. O'Brien, ''Thermal or Electrical Conduction Through a Granular Material'' Proceedings of the Royal Society A, London, Volume 355 – Issue 1682, 1977, Pages 313-333.

[79] T. S. Yun, T. M. Evans, "Three-dimensional random network model for thermal conductivity in particulate materials", Computers and Geotechnics, Volume 37, 2010, Pages 991–998.

[80] S. Kanuparthi, G. Subbarayan, T. Siegmund, "An Efficient Network Model for Determining the Effective Thermal Conductivity of Particulate Thermal Interface Materials" Ieee Transactions on Components and Packaging Technologies, Volume 31 – Issue 3, 2008, Pages 611-621.

[81] Y. Gan, F. Hernandez, D. Hanaor, R. K. Annabattula, M. Kamlah, P. Pereslavtsev, "Thermal discrete element analysis of EU solid breeder blanket subjected to neutron irradiation", Fusion Science and Technology, Volume 66, 2014, Pages 83-90.

[82] M. Smoluchowski, "Über den Temperatursprung bei Wärmeleitung in Gasen" Pisma Mariana Smoluchowskiego 1.1, 1924, Pages 113-138.

[83] K. Raed, "Investigation of Knudsen and gas-atmosphere effects on effective thermal conductivity of porous media", Ph.D. thesis, Faculty of Mechanical, Process and Energy Engineering, Technische Universität Bergakademie Freiberg, 2013.

[84] A. Ying, Z. Lu, M. Abdou, "Mechanical behavior and design database of packed beds for blanket designs", Fusion Engineering and Design, Volumes 39–40, 1998, Pages 759–764.

[85] Z. Lu, A. Ying, M. Abdou, "Numerical and experimental prediction of the thermomechanical performance of pebble beds for solid breeder blanket", Fusion Engineering and Design, Volumes 49–50, 2000, Pages 605–611.

[86] J. Reimann and G. Wörner, "Thermal creep of Li4SiO4 pebble beds", Fusion Engineering and Design, Volume 58 –Issue 59, 2001, Pages 647–651.

[87] G. Piazza J. Reimann, E. Günther, R. Knitter, N. Roux, J. D. Lulewicz, "Characterisation of ceramic breeder materials for the helium cooled pebble bed blanket", Journal of Nuclear Materials, Volumes 307–311 (Part 1(0)) (2002), Pages 811–816.

[88] J. Reimann, L. Boccaccini, M. Enoeda, A. Ying, "Thermomechanics of solid breeder and be pebble bed materials", Fusion Engineering and Design, Volumes 61–62, 2002, Pages 319–331.

[89] L. Bühler and J. Reimann, "Thermal creep of granular breeder materials in fusion blankets", Journal of Nuclear Materials, Volumes 307–311, 2002, Pages 807–810.

[90] G. Dell'Orco, P. A. Di Maio, R. Giammusso, A. Malavasi, L. Sansone, A. Tincani, G. Vella, "Progress in the benchmark exercise for analyzing the lithiate breeder pebble bed thermo-mechanical behaviour", Fusion Engineering and Design, Volume 81, 2006, Pages 169–174.

[91] C. S. Zhang A. Ying, M. Abdou, Y.-H. Park, "Ceramic breeder pebble bed packing stability under cyclic loads", Fusion Engineering and Design, Volume 109-111 A, 2016, Pages 267-271.

[92] A. Ying J. Reimann, L. Boccaccini, M. Enoeda, M. Kamlah, R. Knitter, Y. Gan, J. G. van der Laan, L. Magielsen, P. A. Di Maio, G. Dell'Orco, R. K. Annabattula, J. T. Van

Lew, H. Tanigawa, S. Til, "Status of ceramic breeder pebble bed thermomechanics R&D and impact on breeder material mechanical strength", Fusion Engineering and Design, Volume 87, 2012, Pages 1130–1137.

[93] J. T. Van Lew, A. Ying, M. Abdou, "A discrete element method study on the evolution of thermomechanics of a pebble bed experiencing pebble failure", Fusion Engineering and Design, Volume 89, 2014, Pages 1151–1157.

[94] J. T. Van Lew Y.-H. Park, A. Ying, M. Abdou, "Modifying Young's modulus in DEM simulations based on distributions of experimental measurements", Fusion Engineering and Design, Volumes 98–99, 2015, Pages 1893–1897.

[95] W. S. Jodrey and E. M. Tory, "Computer simulation of close random packing of equal spheres", Physical review A, Volume 32-Issue 4, 1985, Pages 2347–2351.

[96] X. Wang, M. Ye, H. Chen, "Computational study on the behaviors of granular materials under mechanical cycling", Journal of Applied Physics, Volume 118 – Issue 17, 2015, Pages 174901_1- 174901_8.

[97] H. Zhang, H. Guo, T. Shi, M. Ye, H. Huang, Z. Li, "Cyclic loading tests on ceramic breeder pebble bed by discrete element modelling", Fusion Engineering and Design, Volume 118, 2017a, Pages 40-44.

[98] H. Zhang, H. Guo, M. Ye, Z. Li, H. Huang, "Investigation on the packing behaviors and mechanics of Li_4SiO_4 pebble beds by discrete element method", Fusion Engineering and Design, Volume 125, 2017b, Pages 551-555.

[99] A. Abou-Sena, A. Ying and M. Abdou, "Effective thermal conductivity of lithium ceramic pebble beds for fusion blankets: a review", Fusion Science and Technology, Volume 47, 2005, Pages 1094–1100.

[100] M. Dalle Donne and G. Sordon, "Heat Transfer in Pebble Beds For Fusion Blankets", Fusion Technology, Volume 17 – Issue 4, 1990, Pages 597-635.

[101] M. Dalle Donne A. Goraieb, R. Huber, B. Schmitt, G. Schumacher, G. Sordon, A. Weisenburger, "Heat Transfer and Technological Investigations on Mixed Beds of Beryllium and Li_4SiO_4 pebbles", Journal of Nuclear Materials, Volume 212, 1994, Pages 872-876.

[102] M. Dalle Donne, H. Yang, Q. Zhan, S. Liu, B. Zhu, Y. Zhang, "Measurements of the effective thermal conductivity of Li_4SiO_4 pebble bed", Fusion Engineering and Design, Volume 49, 2000, Pages 545-550.

[103] M. Enoeda, Y. Ohara, N. Roux, A. Ying, G. Piazza, S. Malang, "Effective Thermal Conductivity Measurement of the Candidate Ceramic Breeder Pebble Beds by the Hot Wire Method", Fusion Technology, Volume 39, 2001, Pages 621-616.

[104] R. Bauer and E. U. Schlunder, "Effective Radial Thermal Conductivity of Packings in Gas Flow. Part II. Thermal Conductivity of the Packing Fraction without Gas Flow", International Journal of Chemical Engineering, Volume 18, 1978, Page 189.

[105] R. O. A. Hall and D. G. Martin, "The thermal conductivity of powder beds. a model, some measurements on UO2, vibro-compacted microspheres, and their correlation", Journal of Nuclear Materials, Volume 101, 1981, Pages 172-183.

[106] J. Reimann and S. Hermsmeyer, "Thermal conductivity of compressed ceramic breeder pebble beds", Fusion Engineering and Design, Volumes 61-62, 2002, Pages 345-351.

[107] Y. Feng, K. Feng, Y. Liu, B. Gong, Y. Cheng, "Experimental Investigation of Thermal Properties of the Li4SiO4 Pebble Beds", Journal of Plasma Fusion Research SERIES, Volume 11, 2015, Pages 49-52.

[108] S. Pupeschi, R. Knitter, M. Kamlah, "Effective thermal conductivity of advanced ceramic breeder pebble beds", Fusion Engineering and Design, Volume 116, 2017, Pages 73–80.

[109] W. Pannhorst, V. Geiler, G. Rake, B. Speit, D. Sprenger, "Production Process of Lithium Orthosilicate Pebbles", Fusion Tech. 1998, Proceedings of 20th Symposium on Fusion Technology, Sept. 7-11, 1998, Marseille, France, B. Beaumont, P. Libeyre, B. de Gentile, G. Tonon (Eds.), Volume 2, Pages 1441-1444.

[110] M. Kolb, R. Knitter, U. Kaufmann, D. Mundt, "Enhanced fabrication process for lithium orthosilicate pebbles as breeding material", Fusion Engineering and Design, Volume 86, 2011, Pages 2148-2151.

[111] J. Sullivan, C. L. Brayman, R. A. Verrall, J. M. Miller, P. J. Gierszewski, F. Londry, A. Slavin,"Canadian ceramic breeder sphere technology-capability and recent results", Fusion Engineering and Design, Volume 17, 1991, Pages 79-85.

[112] P. Lorenzetto P. Gierszewski, G. Simbolotti, "A European proposal for an ITER water-cooled solid breeder blanket", Fusion Engineering and Design, Volume 27, 1995, Pages 423-429.

[113] J. Earnshaw, F. A. Loundry, P. J. Gierszewski, "The Effective Thermal Conductivity of Bed of 1.2mm Lithium Zirconate Spheres in Helium", Fusion Technology, Volume 33, 1998, Pages 31-37.

[114] T. Hatano, M. Enoeda, S. Suzuki, Y. Kosaku, M. Akiba, "Effective Thermal Conductivity of a Li_2TiO_3 Pebble Bed for a Demo Blanket", Fusion Science and Technology, Volume 44, 2003, Pages 94-98.

[115] A. Abou Sena et al., "Experimental measurements of the effective thermal conductivity of a lithium titanate (Li2TiO3) pebbles-packed bed", Journal of Materials Processing Technology 181 (2007) 206–212.

[116] M. Panchal, P. Chaudhuri, J. T. Van Lew, A. Ying, "Numerical modelling for the effective thermal conductivity of lithium meta titanate pebble bed with different packing structures", Fusion Engineering and Design, Volume 112, 2016, Pages 303-310.

[117] COMSOL Multi physics https://www.comsol.com/ (November 27, 2018).

[118] M. Enoeda, S. Satoh; T. Kurasawa; H. Takatsu,"Measurement of Effective Conductivity of Lithium Oxide & Beryllium Packed Bed", 15th IEEE /NPSS Symposium Fusion Engineering, Volume 282, 1994.

[119] M. Moscardini, Y. Gan, R. K. Annabattula and M. Kamlah, "A Discrete Element Method to simulate the mechanical behavior ofellipsoidal particles for a fusion breeding blanket", Fusion Engineering and Design, Volume 121, 2017, Pages 22-31.

[120] Wolfram Mathematica 13.0, 2015 http://www.wolfram.com/ (November 27, 2018).

[121] K.L. Johnson, "Contact Mechanics", Cambridge University Press, 1985, Cambridge. doi:10.1017/CBO9781139171731.

[122] N. Bicanic, "Discrete element methods", In E. Stein, R. de Borst, and T. J. R. Hughes, editors, Encyclopedia of Computational Mechanics 1, 2004, Pages 311-337, Chichester: John Wiley and Sons.

[123] C. A. Truesdell, "A First Course in Rational Continuum Mechanics. Vol. 1: General Concepts", 2nd ed., III, 1991, Boston: Academic Press. Sects. I.8-10.

[124] W. C. Swope and H. C. Andersen, "A computer simulation method for the calculation of equilibrium constants for the formation of physical clusters of molecules: Application to small water clusters", Journal of Chemical Physics, Volume 76, 1982, Pages 76-637.

[125] L. Verlet, "Computer" Experiments" on Classical Fluids", I. Thermodynamical Properties of Lennard-Jones Molecules. Physical Review, Volume 159 – Issue 1, 1967, Pages 98-103.

[126] W. R Hamilton, "On Quaternions, or on a new system of imaginaries in Algebra", in The London, Edinburgh, and Dublin Philosophical Magazine and Journal of Science, Volume 25, 3rd Series, no. 163, 166 & 169, 1844.

[127] I.Kosenko, "Integration of the equations of a rotational motion of a rigid body in quaternion algebra. The Euler case.", Journal of Applied Mathemathics and Mechanics, Volume 62 – Issue 2, 1998, Pages 193–200

[128] E.Celledoni and N.Säfström, "Efficient time-symmetric simulation of torqued rigid bodies using Jacobi elliptic functions", Journal of Physics A: Mathematical and General, Volume 39 – Issue 19, 2006, Pages 5463–5478.

[129] E.Hairer and G.Vilmart, "Preprocessed discrete Moser Veselov algorithm for the full dynamics of a rigid body", Journal of Physics A: Mathematical and General, Volume 39 – Issue 42, 2006, Pages 13,225–13,235

[130] F. Zhao and B. G. M. vanWachem, "A novel Quaternion integration approach for describing the behavior of non-spherical particles", Acta Mechanica, Volume 224, 2013, Pages 3091–3109.

[131] S. A. Whitmore and L. Hughes, "Closed-form Integrator for the Quaternion (Euler Angle) Kinematics Equations", US patent (2000), Patent Number 6,061,611.

[132] B. Löbbecke and R. Knitter, "Procurement and quality control of Li4SiO4 pebbles for testing of breeder unit mock-ups.", Fusion Nr. 311, final report on TW6-TTBB-006-D2, Forschungszentrum Karlsruhe. Technical report, 2007.

[133] N. Zaccari and D. Aquaro, "Mechanical characterization of Li_2TiO_3 and Li_4SiO_4 pebble beds: experimental determination of the material properties and of the pebble bed effective value", Fusion Engineering and Design, Volume 82 – Issues 15-24, 2007, Pages 2375–2382.

[134] A. Donev, F. H. Stillinger, P. M. Chaikin, S. Torquato, "Unusually dense crystal packings of ellipsoids", Physical Review Letters, Volume 92, 2004, Pages 2555061-2555064.

[135] M. G. Kaganer, "Thermal insulation in cryogenic engineering", Israel Program for Scientific Translations, Jerusalem, 1969.

[136] N. Wakao and S. Kagnei, "Heat and mass transfer in packed beds", Gordon and Breach, New York, 1982.

[137] B. Baule, "Theoretische Behandlung der Erscheinungen in verduennten Gasen", Annalen der Physik, Volume 44, 1914,Pages 145-176.

[138] F. O. Goodman, "Thermal accommodation coefficients", The Journal of Physical Chemistry, Volume 84, 1980, Pages 1431-1445.

[139] B. Löbbecke, R. Knitter, M. Rohde, J. Reimann, "Thermal conductivity of sintered lithium orthosilicate compacts", Journal of Nuclear Material, Volumes 386–388, 2009, Pages 1068–1070.

[140] Dr. R. Knitter, Karlsruhe Institute of Technology, personal communication based on the results reported in [139], 2017.

[141] P. Gierszewski, "Review of Properties of Lithium Metatitanate", Fusion Engineering and Design, Volumes 39-40, 1998, Pages 739-743.

[142] S. Saito, K. Tsuchiyaa, H. Kawamuraa, T. Teraib, S. Tanakab, "Density dependence on thermal properties of Li_2TiO_3 pellets", Journal of Nuclear Material, Volume 253, 1998, Pages 213–218.

[143] P. Gierszewski, "Thermal conductivity of lithium metazirconate", Fusion Technology, Volume 23, 1993, Pages 333.

[144] D. A. Moore, "A compilation of data and a review of the properties of lithium monoxide and lithium zirconates relevant to their use as tritium breeder material in fusion reactors", UKAEA, Northern Research Laboratories, Springfields, NRL-R-2014 (S), 1989.

[145] D. R. Lide, CRC Handbook of Chemistry and Physics, 95th Edition, Boca Raton: CRC Press, 2004.

[146] The Engineering ToolBox, http://www.engineeringtoolbox.com (November 27, 2018).

[147] F. Hernández, F. Cismondi, B. Kiss, "Fluid dynamics and thermal analysis of a HCPB TBM Breeder Unit mock-up", Fusion Engineering and Design, Volumes 86 – Issue 9-11, 2011, Pages 2278-2281.

[148] F. Hernandez, P. Pereslavtsev, Q. Kang, P. Norajitra, B. Kiss, G. Nádasi, O. Bitz, "A new HCPB breeding blanket for the EU DEMO: Evolution, rationale and preliminary performances", Fusion Engineering and Design, Volume 124, 2017, Pages 882-886.

[149] F. Hernández, Q. Kang, B. Kiss, P. Norajitra, G. Nádasi, P. Pereslavtsev, C. Zeile, "HCPB Design Report 2015", Deliverable ID BB-1.2.1-T002-D001, EUROfusion Final Report 2016.

[150] P. Pereslavtsev U. Fischer, F. Hernandez, L. Lu, "Neutronic analyses for the optimization of the advanced HCPB breeder blanket design for DEMO", Fusion Engineering and Design, Volume 124, 2017, Pages 910-914.

[151] D. R. Hanchar and M. S. Kazim, "A Tritium Permeation Model for Conceptual Fusion Reactor Designs", Journal of Fusion Energy, Volume 3, 1983, Pages 47-61.

[152] O. Krikorian, "Estimation of the Thermophysical and Mechanical Properties and the Equation of State of Li2O", High Temperature-High Pressures, Volume 17, 1985.

[153] M. Billone, W. Dienst, T. Flament, P. Lorenzetto, K. Noda, N. Roux, "ITER Solid Breeder Blanket Materials Database", Energy Technology Division/Fusion Power Program/Engineering Physics Division, 1993.

[154] ARIES Program - Public Information Site, "Thermal and Structural Properties of Fusion related Materials - LITHIUM SILICATE (Li4SiO4)", http://www-ferp.ucsd.edu/LIB/PROPS/PANOS/li4sio4.html (November 27, 2018).

[155] F. Hernández, F. Cismondi, B. Kiss, "Thermo-mechanical analyses and assessment with respect to the design codes and standards of the HCPB-TBM Breeder Unit", Fusion Engineering and Design, Volumes 87 – Issue 7-8, 2012, Pages 1111-1117.

[156] S. Yagi, and D. Kunii, "Studies on heat transfer near wall surface in packed beds" Americal Institute of Chemical Engineers, 1960, Pages 97-104.

[157] L.V. Boccaccini, S. Ciattaglia, R. Meyder, "Review of Safety Issues for the European HCPB Test Blanket System", Nuclear Fusion, Volume 47,2007, Pages S436-S441.

Appendix A

Analytical estimation of the temperature profile in the breeder zone

Here, the temperature profile generated from the neutronic heating along the pebble bed thickness is analytically calculated. To this end, starting from the heat conduction equation

$$\rho c_p \frac{\partial T}{\partial t} - \nabla \cdot (k \, \nabla T) = \dot{q}_v ,$$

where mass density ρ [kg/m^3], heat capacity c_p [J/kg K], and thermal conductivity k [W/mK] are the properties of the medium while $\dot{q}_v$ [W/ m^3] is the volumetric heat source. Under stationary condition, constant properties of the medium and one dimensional cross plane conduction through an infinite plate, the heat conduction equation reduces to

$$k \, \frac{\partial^2 T}{\partial x^2} + \dot{q}_v = 0 .$$

According to the conditions used in the DEM simulations, the equation was solved for an infinite plate with a thickness H of 15 mm and applying a constant temperature T_c of 500 ºC at x=0 and x=15 mm as boundary conditions. The analytical solution to evaluate the temperature of the bed in the thickness reads as

$$T = -\frac{\dot{q}_v \, x^2}{2 \, k} + \frac{\dot{q}_v \, H \, x}{2 \, k} + T_c$$

The EU Ref. breeder bed packed at 64% is considered as a continuum, thus the power density acting on the solid material (reported in Figure 5–1) is multiplied by 0.64 and applied as volumetric heat source for the whole bed (pebbles+voids). Like in the DEM simulations, a constant temperature of 500 ºC was applied as boundary condition at x=0 and x=15 mm. In particular, an effective power density of 14.9 MW/m^3 was applied to represent the thermal behavior of the bed at 50mm from the first wall. The effective thermal conductivity of the bed in helium and air at 2 bar is set according to the equations reported in [108] (S. Pupeschi et al., 2017), which are

$$k_{eff} = 0.902 + (0.000166 * T[°C]),$$

and

$$k_{eff} = 0.378 + (0.000293 * T[°C]),$$

respectively.

In Figure A–1 and in Figure A–2, the analytical results obtained using helium and air at 2 bar as filling gas are compared to the temperature profile predicted by means of the DEM code for an assembly located at 50 mm, respectively. Different curves (dashed lines) refer to temperature profiles obtained by means of the analytical method applying the effective thermal conductivity at different average bed temperatures.
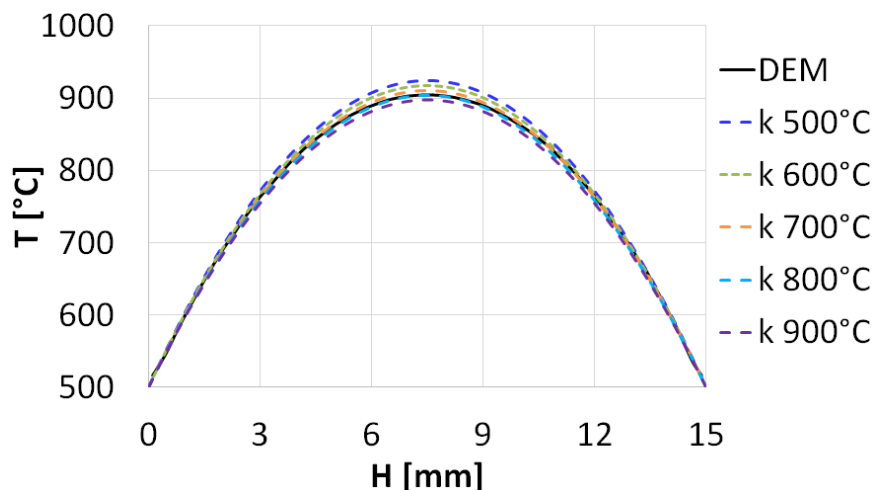
Figure A–1: Comparison between the temperature profiles obtained with the DEM code and the analytical method at different average bed temperatures in helium at 50mm from the first wall.
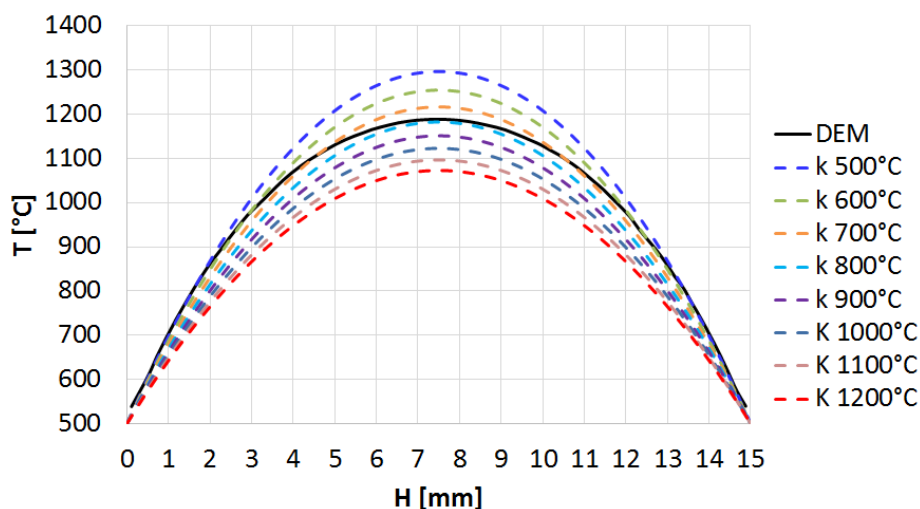
Figure A–2: Comparison between the temperature profiles obtained with the DEM code and the analytical method at different average bed temperatures in air at 50mm from the first wall.

In Figure A–1, a good agreement between DEM results (solid black line) and analytical values obtained at 800°C in helium is shown, while a negligible difference with the temperature profile obtained at 900 °C is observed. In Figure A–2 analytical results in air at 800 °C perfectly match the temperature profile obtained with the DEM code. In terms of peak temperature, which has to be controlled to avoid the sintering of the pebbles, a difference of about 8% occurs between DEM results and analytical values at 1100 °C. The difference is due

to the approximation introduced by the correlations to evaluate the effective thermal conductivity. Indeed an uncertainty of about 10% is declared in [108] (S. Pupeschi et al., 2017) for the used equations and the error is lower than the uncertainty. The good agreement between the two approaches confirms the suitability simulating pebble beds as a continuum, and, thus, it confirms the possibility to determine accurate results about the thermal behavior of ceramic breeder pebble beds by means of FEM approaches.

Appendix B

Smoluchowski effect on the thermal conductivity of confined gases

In this appendix the influence of the gas temperature and the size of the gas confining space on the Smoluchowski effect is presented. Applying the Eqs. 4.12-4.15 with the values reported in Table 4–4, the S-shape curves describing the variation of the thermal conductivity with the gas pressure were reproduced for helium. The influence of the gas pressure on the thermal conductivity of helium for different temperatures and gap sizes is shown in Figure B–1 and Figure B–2, respectively. In Figure B–1 results refer to a constant gap of 30 μm, while a temperature of 500°C was used for values reported in Figure B–2. For a given gap size a temperature increase shifts the onset of the transition region to higher pressures, while for a given temperature the increase of the gap size shifts the onset of the transition region to lower pressures.
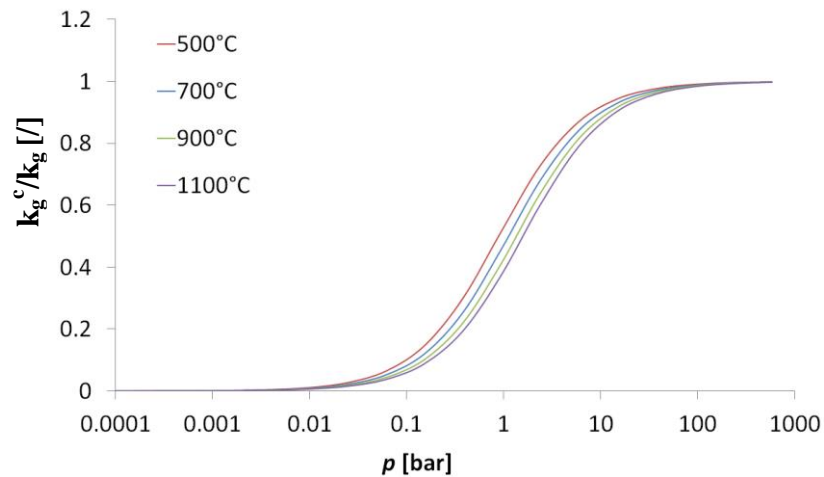
Figure B–1: Variation of the helium thermal conductivity as a function of the gas pressure at different average temperatures for a given confining gap size of 30 μm.
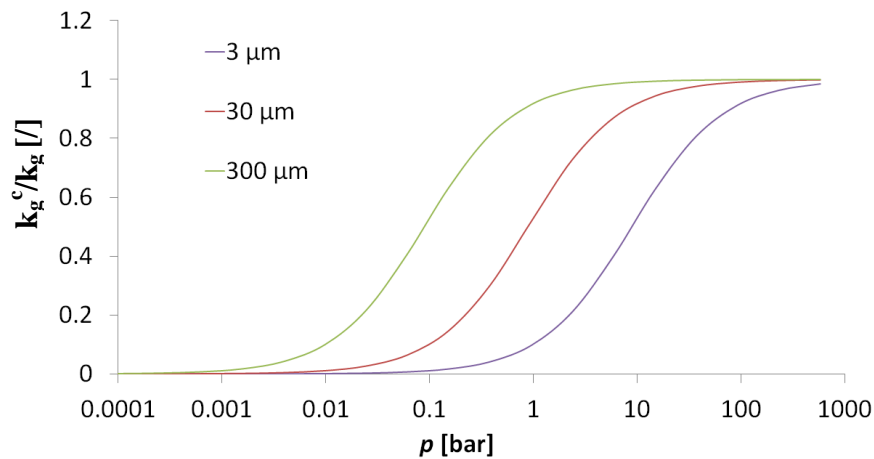
Figure B–2: Variation of the helium thermal conductivity as a function of the gas pressure for different values of confining gap size at 500°C.

Acknowledgements